Molecular Cell

Article

α-Synuclein aggregates inhibit ESCRT-III through sequestration and collateral degradation

Graphical abstract

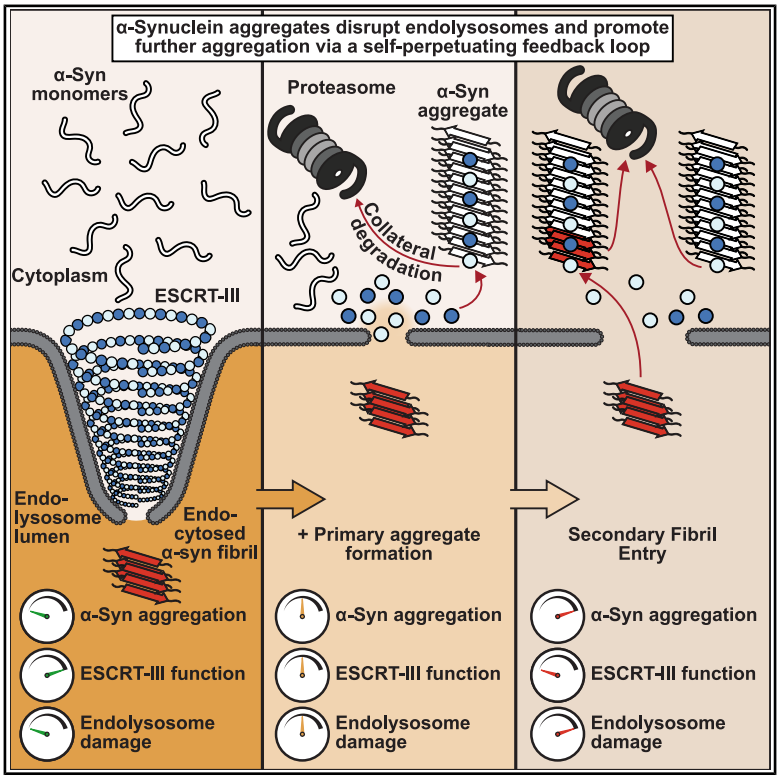

Highlights

- α-Synuclein fibrils bind and sequester ESCRT-III endolysosome repair proteins
- An α-helical segment common to ESCRT-III mediates fibril-selective interaction
- Fibril-bound ESCRT-III subunits undergo "collateral degradation" via the proteasome
- ESCRT-III depletion damages endolysosomes and worsens α-synuclein aggregation

Authors

Cole S. Sitron, Victoria A. Trinkaus, Ana Galesic, ..., Irina Dudanova, J. Wade Harper, F. Ulrich Hartl

Correspondence

uhartl@biochem.mpg.de

In brief

Neurodegeneration-associated aggregates, such as α-synuclein inclusions in Parkinson's disease, often contain ESCRT-III proteins. Sitron et al. reveal how α-synuclein aggregates bind ESCRT-III proteins, immobilizing them and triggering their "collateral degradation." This cascade functionally depletes ESCRT-III to initiate a toxic feedback loop.

Sitron et al., 2025, Molecular Cell *85*, 3505–3523
September 18, 2025
https://doi.org/10.1016/j.molcel.2025.08.022

CellPress

Molecular Cell

CellPress
OPEN ACCESS

Article

α-Synuclein aggregates inhibit ESCRT-III through sequestration and collateral degradation

Cole S. Sitron,[1,2,3] Victoria A. Trinkaus,[1,2,3,9] Ana Galesic,[2,4,8] Maximilian Garhammer,[1,2,3,8] Patricia Yuste-Checa,[1,2,3,8] Ulrich Dransfeld,[1,2,3,8] Dennis Feigenbutz,[5,6,7] Jiuchun Zhang,[4] Larysa Ivashko,[1,2,3] Irina Dudanova,[5,6,7] J. Wade Harper,[2,4] and F. Ulrich Hartl[1,2,3,10,*]

[1]Department of Cellular Biochemistry, Max Planck Institute of Biochemistry, 82152 Martinsried, Germany
[2]Aligning Science Across Parkinson's (ASAP) Collaborative Research Network, Chevy Chase, MD 20815, USA
[3]Munich Cluster for Systems Neurology (SyNergy), 81377 Munich, Germany
[4]Department of Cell Biology, Harvard Medical School, Boston, MA 02115, USA
[5]Molecular Neurodegeneration Group, Max Planck Institute for Biological Intelligence, 82152 Martinsried, Germany
[6]Department of Molecules–Signaling–Development, Max Planck Institute for Biological Intelligence, 82152 Martinsried, Germany
[7]Center for Anatomy, Faculty of Medicine and University Hospital Cologne, University of Cologne, 50931 Cologne, Germany
[8]These authors contributed equally
[9]Present address: Department of Structural Biochemistry, Max Planck Institute of Molecular Physiology, 44227 Dortmund, Germany
[10]Lead contact
*Correspondence: uhartl@biochem.mpg.de
https://doi.org/10.1016/j.molcel.2025.08.022

SUMMARY

α-Synuclein aggregation is a hallmark of Parkinson's disease and related synucleinopathies. Extracellular α-synuclein fibrils enter naive cells via endocytosis, followed by transit into the cytoplasm to seed endogenous α-synuclein aggregation. Intracellular aggregates sequester numerous proteins, including subunits of the endosomal sorting complexes required for transport (ESCRT)-III system for endolysosome membrane repair, but the toxic effects of these events remain poorly understood. Using cellular models and *in vitro* reconstitution, we found that α-synuclein fibrils interact with a conserved α-helix in ESCRT-III proteins. This interaction sequesters ESCRT-III subunits and triggers their proteasomal destruction in a process of "collateral degradation." These twin mechanisms deplete the available ESCRT-III pool, initiating a toxic feedback loop. The ensuing loss of ESCRT function compromises endolysosome membranes, thereby facilitating escape of aggregate seeds into the cytoplasm, facilitating a "second wave" of templated aggregation and ESCRT-III sequestration. We suggest that collateral degradation and the triggering of self-perpetuating systems are general mechanisms of sequestration-induced proteotoxicity.

INTRODUCTION

In neurodegenerative diseases, including Alzheimer's disease (AD) and Parkinson's disease (PD), aggregate pathology spreads through the brain in disease-specific patterns.[1–5] For instance, α-synuclein (α-syn) aggregates in PD arise in the brainstem or peripheral nerves before spreading to higher brain regions, correlating with clinical decline.[6–10]

The molecular mechanism underlying spreading is thought to be prion-like aggregate "seeding," where fibrillar protein seeds transfer between cells, then template the misfolding and aggregation of their monomeric counterparts.[11–14] Seeds leave donor cells via several mechanisms, including release into the extracellular milieu.[15–19] Highlighting the importance of this exocytic route, α-syn aggregate seed detection in cerebrospinal fluid shows promise in early PD diagnosis.[20–23] Aggregate seeds released as naked proteins can enter acceptor cells by endocytosis, arriving in membrane-bound endolysosomal organelles.[12,24–30] Confinement inside endolysosomes restricts seeds from accessing the cytoplasmic pool of monomeric protein. However, endolysosomal membrane ruptures permit seeds to escape and trigger aggregation.[26,31–35]

The endosomal sorting complexes required for transport (ESCRT) machinery, a series of cytosolic protein complexes (ESCRT-0, -I, -II, and -III), mediates membrane fission[36–46] and repairs endolysosomal membrane damage, preventing aggregate seed leakage into the cytoplasm. ESCRT-III comprises 12 proteins in humans, including three paralog groups with partially overlapping function. ESCRT-III proteins form spiral, spring-shaped hetero-oligomers that invaginate the membrane they bind.[31,47–55] The AAA ATPase VPS4 disassembles these oligomers, severing invaginated membranes to form intralumenal vesicles.[56–64] ESCRT-III oligomerization constricts membranes at damage sites, bringing membrane edges together to reseal lesions.[40,42,65,66] Underscoring ESCRT's role in maintaining nervous system health, mutations in the ESCRT-III protein CHMP2B

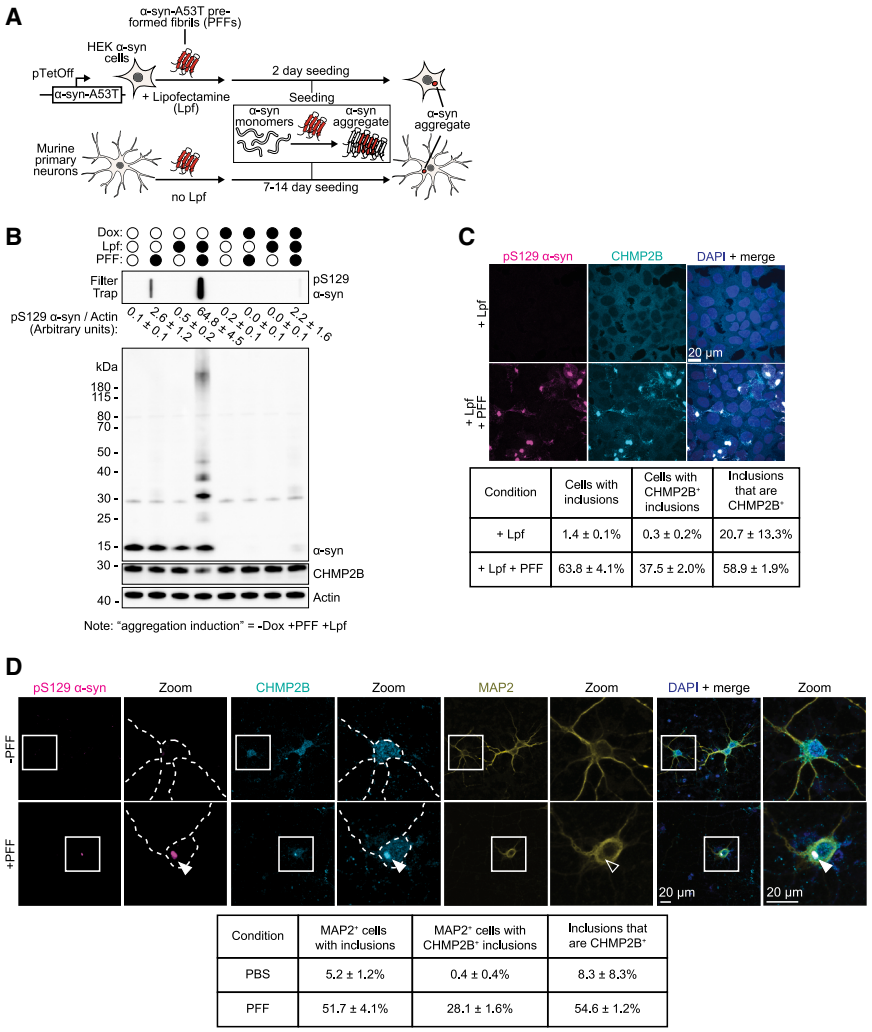

Condition	Cells with inclusions	Cells with CHMP2B⁺ inclusions	Inclusions that are CHMP2B⁺
+ Lpf	1.4 ± 0.1%	0.3 ± 0.2%	20.7 ± 13.3%
+ Lpf + PFF	63.8 ± 4.1%	37.5 ± 2.0%	58.9 ± 1.9%

Condition	MAP2⁺ cells with inclusions	MAP2⁺ cells with CHMP2B⁺ inclusions	Inclusions that are CHMP2B⁺
PBS	5.2 ± 1.2%	0.4 ± 0.4%	8.3 ± 8.3%
PFF	51.7 ± 4.1%	28.1 ± 1.6%	54.6 ± 1.2%

Figure 1. α-Syn aggregates sequester ESCRT-III proteins

(A) Workflow to induce α-syn aggregation. α-syn, α-synuclein A53T; PFFs, α-syn-A53T pre-formed fibrils; Lpf, lipofectamine.

(B) Representative immunoblot and filter trap of HEK α-syn cells with tetracycline-repressible α-syn expression. Cells underwent 10-day doxycycline (Dox) treatment to turn off α-syn expression, then 2-day PFF/Lpf treatment. Filters were probed for Ser129-phosphorylated (pS129) α-syn; immunoblots probed for α-syn, CHMP2B, and β-actin (loading control). Densitometric pS129 α-syn intensities normalized to β-actin shown below filter trap (mean ± SEM, $n = 3$).

(C) Representative immunofluorescence microscopy of HEK α-syn cells ± aggregation induction, stained for pS129 α-syn and CHMP2B.

(D) Representative primary neuron immunofluorescence after 14-day PFF treatment, stained for pS129 α-syn, CHMP2B, and MAP2 (neuronal cytoskeletal marker). Dashed lines: contours of the neurons. Arrowheads: pS129 α-syn inclusions.

Summary statistics appear below (C) and (D). Data presented as mean ± SEM, $n = 3$.

See also Figure S1.

cause diseases of the amyotrophic lateral sclerosis-frontotemporal dementia spectrum (ALS-FTD)[67–69] and have been found in patients with dementia with Lewy bodies (DLB), a PD-related synucleinopathy.[70] Although CHMP2B has a paralog, CHMP2A, only CHMP2B mutations have been implicated as neurodegenerative risk factors.

Neurodegeneration-associated aggregates contain numerous macromolecules besides the primary disease protein. Lewy bodies in PD contain α-syn fibrils, organelles, membranes, and over 100 other proteins.[8,71,72] Researchers have long posited that sequestration of bystander proteins by aggregates depletes the available pool of these proteins, causing widespread loss of function and subsequent proteostasis collapse.[73–75] Although this "*trans*-acting loss of function" is a commonly invoked mechanism of aggregate toxicity, pathomechanistic evidence is rare[76–78] and mostly concerns chaperones or ubiquitin-binding proteins.[79–84]

The ESCRT-III protein CHMP2B co-localizes with aggregates of β-amyloid (Aβ), Tau, and α-syn in patient brains and cellular models.[85–91] It remains unclear whether this co-localization reflects *trans*-acting loss of function by sequestration. Here, we analyzed the α-syn-CHMP2B interaction by reconstitution and in mammalian cell culture models. We find that seeded α-syn aggregates sequester CHMP2B and other ESCRT-III proteins. A central, conserved α-helix of ESCRT-III proteins binds to fibrillar α-syn preferentially over monomers, trapping ESCRT-III proteins in α-syn aggregates and targeting some subunits for "collateral degradation" via the proteasome. These two effects deplete ESCRT-III subunits, inhibiting ESCRT function and thereby compromising endolysosomal membranes. Consequently, exogenous α-syn fibrils leak into the cytoplasm, forming a positive feedback loop between α-syn aggregation and ESCRT-III loss of function. Proteopathic aggregates thus exert *trans*-acting loss of function by both sequestering other cellular proteins and targeting these proteins for collateral degradation.

RESULTS

α-Syn aggregates sequester ESCRT-III proteins

To study the effect of α-syn aggregation on ESCRT-III, we developed a HEK cellular model with controllable α-syn aggregation. As HEK cells have low endogenous α-syn,[92] we expressed the highly aggregation-prone α-syn A53T mutant[30,93] with a doxycycline (Dox)-repressible promoter to provide soluble α-syn for templated aggregation (Figure 1A). The protein was not retained on a cellulose acetate filter, suggesting that it was soluble (Figure 1B). We then exposed these cells to exogenous α-syn A53T preformed fibrils (PFFs)[8,13,14,72,94,95] and lipofectamine ("Lpf"), a commonly used transfection reagent that delivers fibrils to the

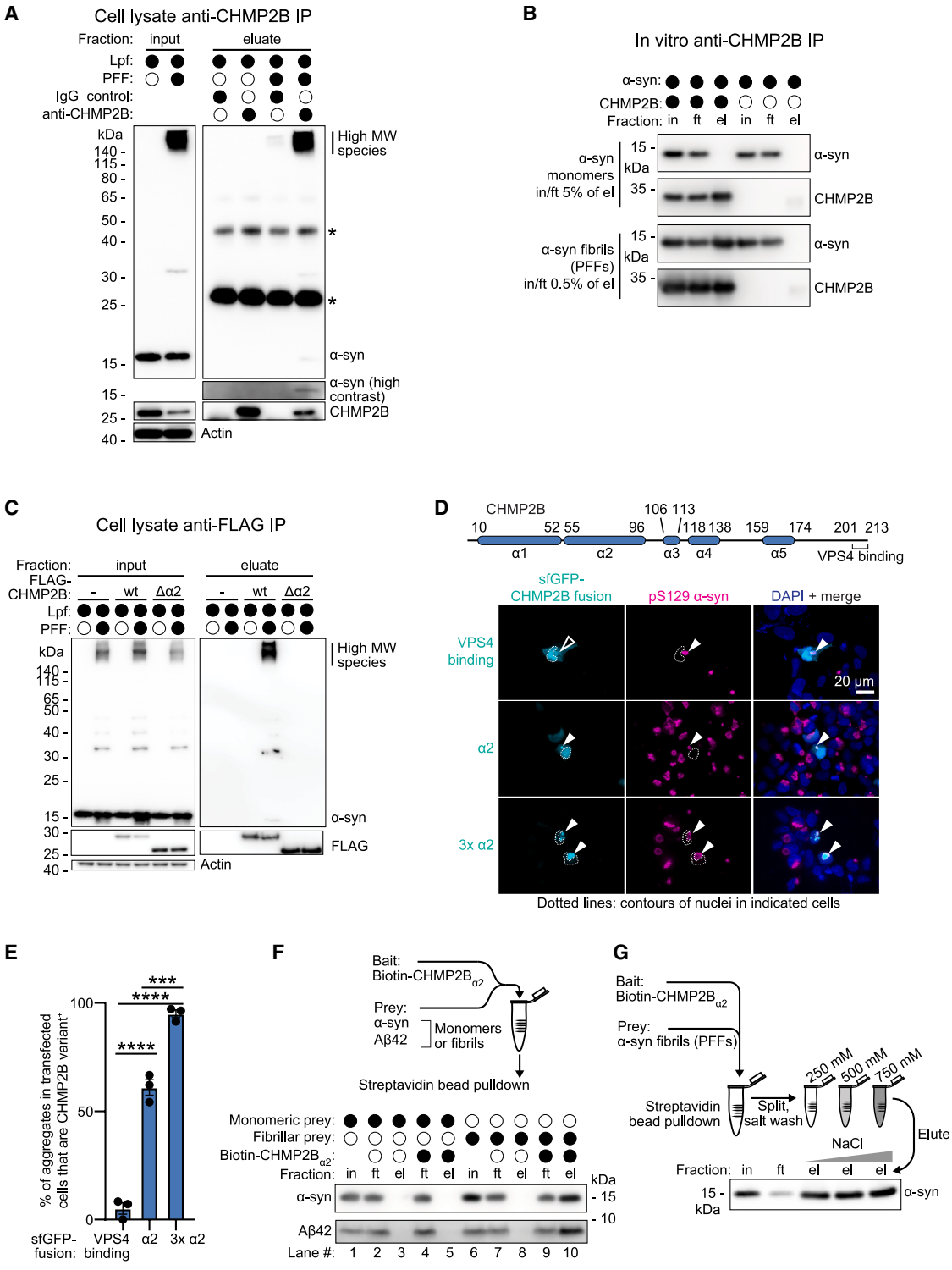

Figure 2. An α-helical segment of CHMP2B binds α-syn fibrils

(A) Representative immunoblot of anti-CHMP2B immunoprecipitation from HEK α-syn cells ± aggregation induction, stained for CHMP2B, α-syn, and β-actin (loading control; *n* = 2). Asterisks: nonspecific bands from the protein G-IgG complex. IP, immunoprecipitation.

(B) Representative immunoblots of anti-CHMP2B co-immunoprecipitations of recombinant CHMP2B and α-syn monomers/PFFs, stained for CHMP2B and α-syn (*n* = 3). In, input; Ft, flow-through; El, eluate.

(legend continued on next page)

cytoplasm.[72,96–101] The PFF/Lpf combination triggered the accumulation of high molecular weight (HMW) α-syn species on SDS-PAGE and retention of Ser129-phosphorylated α-syn (pS129 α-syn) on a cellulose acetate filter after 2 days (Figure 1B), indicative of insoluble α-syn aggregates.[102] PFFs alone produced a much smaller amount of filter-retained material (Figure 1B). Blocking intracellular α-syn expression with Dox abolished production of both HMW and filter-retained α-syn (Figure 1B), indicating that aggregates contained endogenous α-syn. For simplicity, the combination of conditions resulting in insoluble α-syn production (PFF/Lpf co-treatment without Dox) will be referred to as "aggregation induction." When visualized by microscopy, aggregation induction produced inclusions that were positive for pathologic α-syn markers: pS129 α-syn, Lys48-linked ubiquitin, and p62/SQSTM1 (Figure S1A).[72,102–105] Thus, the HEK system permits inducible formation of α-syn aggregates that bear pathologic hallmarks.

Induction of aggregation markedly altered CHMP2B localization. Although control HEK cells featured diffuse CHMP2B distribution, CHMP2B re-localized to pS129 α-syn inclusions upon aggregation (Figure 1C; 63.8% of cells with inclusions, 58.9% of which are CHMP2B positive). CHMP2B sequestration also occurred without Lpf when we applied PFFs for 6 days (Figure S1B). Similarly, primary mouse neurons exposed to PFFs for 14 days (without Lpf) formed CHMP2B-positive pS129 α-syn inclusions (Figures 1D and S1C; 51.7% of cells with inclusions, 54.6% CHMP2B positive). The clinical finding of CHMP2B co-localization with α-syn aggregates[86,87,89] can therefore be reproduced in cell culture upon aggregate seeding with or without Lpf.

In addition to co-localizing with α-syn inclusions, CHMP2B levels decreased after aggregate formation in HEK and primary neurons (Figures 1B and S1D–S1F). These results mirror observations in DLB patient brains[86] and will be addressed below.

We next tested whether α-syn associated with other ESCRT-III subunits beyond CHMP2B. CHMP2A (CHMP2B paralog), CHMP3, and CHMP4B co-localized with aggregates but CHMP6 did not (Figure S1G). This result implies that α-syn aggregates sequester much of the ESCRT-III system, with CHMP2B-α-syn co-localization serving as a proxy for this effect. Given the strong clinical links between CHMP2B and neurodegenerative disease,[67–70,85–88,106,107] we focus on CHMP2B and its paralog CHMP2A, though our findings likely extend to other ESCRT-III subunits.

An α-helical CHMP2B segment binds α-syn fibrils

To determine whether α-syn aggregates and CHMP2B interact physically, we immunoprecipitated CHMP2B from cells with and without α-syn aggregates. CHMP2B co-immunoprecipitated α-syn only after aggregation induction, with Lpf-only control immunoprecipitations failing to recover α-syn (Figure 2A). We obtained similar results with α-syn aggregates generated without Lpf (Figure S2A).

Because both α-syn and ESCRT-III proteins bind membranes,[108–118] their interaction could be indirect, bridged by membranes inside α-syn inclusions.[71,72,119–122] To address this possibility, we expressed a membrane-binding-deficient CHMP2B mutant (CHMP2B L4D/F5D[123]). Both exogenously expressed wild-type (WT) and mutant CHMP2B co-localized with pS129 α-syn inclusions (Figures S2B and S2C; 87.8% and 88.7% exogenous CHMP2B positive, respectively), suggesting a membrane-independent interaction. Compared with endogenous CHMP2B (Figure 1C), exogenous expression increased CHMP2B association with aggregates (87.8% vs. 58.9%), likely due to higher CHMP2B levels. We further evaluated the interaction by *in vitro* co-immunoprecipitation of recombinant components (Figure 2B). Anti-CHMP2B pull-down co-purified α-syn PFFs, but not monomers, alongside CHMP2B (Figure 2B), supporting a direct, fibril-specific interaction.

To map the ESCRT-III-α-syn interaction interface, we evaluated the ability of a series of CHMP2B mutants to associate with α-syn aggregates in cells. Using membrane-binding-deficient CHMP2B eliminated possible confounding effects of mutations on membrane binding. CHMP2B comprises five core helices and a C-terminal VPS4-binding helix[36–39,41,43] (Figure S2B). Deleting these helices sequentially, we found that most mutants co-localized with α-syn aggregates, but removal of the second helix (α2), spanning residues 55–96, abrogated co-localization (Figures S2B and S2C; 7.8% for "Δα2" and 88.7% for the parental CHMP2B variant). Furthermore, α2 deletion prevented FLAG-tagged CHMP2B from specifically co-immunoprecipitating aggregated α-syn from cell lysates (Figure 2C), indicating that α2 is necessary for the CHMP2B-α-syn interaction.

To test whether α2 was sufficient for binding, we fused it to superfolder GFP (sfGFP). The sfGFP-CHMP2B$_{\alpha2}$ fusion co-localized with α-syn inclusions similarly to endogenous CHMP2B (Figures 1C, 2D, and 2E; 61.0% vs. 58.9%). Expressing a triple-tandem CHMP2B$_{\alpha2}$ repeat to increase avidity enhanced this co-localization (Figures 2D and 2E; 95.0%). In contrast, a control fusion with the C-terminal VPS4-binding helix (residues 201–213) showed no co-localization (Figures 2D and 2E). Thus, CHMP2B$_{\alpha2}$ is sufficient for CHMP2B-α-syn aggregate association.

We then assessed whether CHMP2B$_{\alpha2}$ possesses the same fibril-discriminating properties as the full-length protein. We conjugated a biotinylated synthetic CHMP2B$_{\alpha2}$ peptide to streptavidin resin and evaluated its ability to pull down different fibrillar

(C) Representative anti-FLAG pull-down immunoblots from lysates containing FLAG-CHMP2B constructs, stained for α-syn, FLAG, and β-actin (loading control; $n = 2$).

(D) Representative immunofluorescence micrographs from HEK α-syn cells, showing co-localization of sfGFP fusions of CHMP2B regions (schematic above) with α-syn inclusions. Arrowheads: pS129 α-syn staining-positive inclusions.

(E) Quantification of (D): percent of inclusions positive for sfGFP fusions in transfected cells. Error bars: mean ± SEM ($n = 3$). ***$p < 0.001$; ****$p < 0.0001$ by one-way ANOVA.

(F) Pull-downs of monomeric/fibrillar α-syn and Aβ42 using biotinylated CHMP2B$_{\alpha2}$ (residues 55–96) peptide bound to streptavidin resin ($n = 3$). Representative immunoblots stained for α-syn and Aβ42.

(G) Representative immunoblots showing CHMP2B$_{\alpha2}$ pull-downs of PFFs with variable high-salt washes, as schematized above ($n = 3$).

See also Figure S2.

or monomeric proteins. α-syn monomers associated with neither peptide-conjugated resin nor an unconjugated control (Figure 2F; lanes 5 and 3). However, α-syn PFFs specifically bound CHMP2B$_{\alpha2}$ resin but not unconjugated control (Figure 2F; lanes 10 and 8). Immunoprecipitation of sfGFP-tagged CHMP2B$_{\alpha2}$ from lysates yielded similar results, with the CHMP2B$_{\alpha2}$ triple repeat enhancing α-syn aggregate co-immunoprecipitation, whereas the VPS4-binding region failed to recover α-syn (Figure S2D). CHMP2B$_{\alpha2}$ therefore binds fibrillar but not monomeric α-syn. Because CHMP2B appears in several different neurodegeneration-associated aggregates,[85–88,91] we tested whether its α-syn-interacting helix could bind another amyloid protein, Aβ42. As for α-syn, CHMP2B$_{\alpha2}$ specifically bound fibrillar but not monomeric Aβ42 (Figure 2F; lanes 10 and 5).

All ESCRT-III proteins share this α2 motif, including aggregate-associated CHMP2A, CHMP3, and CHMP4B (Figure S1G), as evidenced by alignment of their α2 regions (Figure S2E). Even CHMP6, which did not co-localize with α-syn aggregates (Figure S1G), has a similar α2 sequence. Indeed, both sfGFP-CHMP6$_{\alpha2}$ and a chimeric CHMP2B containing CHMP6$_{\alpha2}$ co-localized with α-syn inclusions (Figure S2F). CHMP6$_{\alpha2}$ can therefore bind aggregates, but another feature prevents full-length CHMP6 from doing so. Its unique N-terminal myristoylation[124] may draw CHMP6 to membranes, limiting access to cytoplasmic α-syn aggregates.

ESCRT-III α2 helices share physico-chemical properties, including enrichment of basic and aliphatic amino acids, notably methionine (Figure S2G). Basic amino acids cluster at the N terminus, imparting a positive charge (Figure S2E). However, α-syn PFF pull-down by CHMP2B$_{\alpha2}$ resisted high-salt washes (Figure 2G), suggesting a primarily non-electrostatic interaction. The C terminus contains clusters of hydrophobic amino acids with 7-residue spacing, with additional hydrophobic residues at the midpoints between these clusters (Figure S2H). CHMP2B$_{\alpha2}$ also possesses this pattern, albeit shifted 3 amino acids C-terminally (Figure S2E). The spacing of these residues suggests a hydrophobic face on the α-helix (Figure S2I). Reducing the hydrophobicity of this face with V82E, M85E, and M92E mutations—individually or combined—significantly decreased α-syn co-localization (Figures S2J and S2K), implicating this hydrophobic patch in amyloid fibril binding.

In summary, α-syn aggregates in cell culture sequester CHMP2B and other ESCRT-III components. CHMP2B directly binds fibrillar α-syn through its α2 helix, likely using a C-terminal hydrophobic patch. This region also binds Aβ42 fibrils, suggesting ESCRT-III α2 helices may broadly recognize amyloid structures.

α-Syn aggregation inhibits ESCRT

Does ESCRT-III binding to α-syn aggregates affect ESCRT function? To measure ESCRT, we developed an assay using RNF152, an E3 ligase in the lysosomal membrane that autoubiquitinates and is then sorted into the lumen and degraded in an ESCRT-III-dependent manner.[44] We introduced an EGFP-RNF152 reporter into HEK α-syn cells, with IRES-linked mScarlet as an internal translation control (Figure 3A). Flow cytometry (Figure S3A) of EGFP/mScarlet ratios reflects reporter stability, increasing with inhibited EGFP-RNF152 degradation. As expected, inhibitors of ubiquitination or lysosomal function stabilized the reporter (Figure S3B), and the reporter co-localized with the lysosomal marker TMEM192 (Figure S3C).

To establish the reporter's sensitivity to ESCRT-III disruption, we knocked down CHMP2A and CHMP2B, paralogous proteins[31,54] that both associate with α-syn aggregates (Figures S1G and 1C). CHMP2A small interfering RNA (siRNA) knockdown and CHMP2B Cas9-sgRNA knockdown reduced levels by 90% and 78%, respectively (Figures 3B and S3D). Single knockdowns were without effect, but CHMP2A/B double knockdown led to ∼4-fold stabilization (Figure 3C), effecting accumulation of full length and HMW reporter (Figure 3B). Because reporter stabilization required CHMP2A/B double knockdown, we hereafter use this to perturb ESCRT in HEK cells. To impose broader ESCRT stress, we expressed CHMP2B Q165X, an FTD mutant[69] that hyper-oligomerizes,[50,69,117,125–127] sequestering other ESCRT-III proteins.[128] CHMP2B Q165X overexpression stabilized the reporter whereas WT CHMP2B did not; Dox shutoff of α-syn had no effect (Figure S3E). The reporter thus detects reduced ESCRT-III availability.

We next analyzed whether α-syn aggregation affects ESCRT function. Inducing aggregation with 2-day PFF/Lpf treatment stabilized the ESCRT reporter 1.6-fold; Lpf or PFFs alone had no effect, and Dox shutoff of α-syn prevented stabilization (Figure 3D). Reporter mScarlet levels were unaffected (Figure S3F). Aggregation induced by 6-day PFF exposure without Lpf also stabilized the reporter (Figure S3G). Thus, only conditions producing substantial α-syn aggregates (e.g., Figures 1B and S1B) stabilize the reporter. In neurons, PFFs similarly stabilized an sfGFP-RNF152 reporter (Figures 3E and S3H), including cleaved sfGFP fragments—common lysosomal degradation byproducts.[129] These results indicate that ESCRT-III-sequestering α-syn aggregates impair ESCRT function.

If α-syn aggregation perturbs ESCRT by sequestering ESCRT-III, the reporter should be both ubiquitinated and lysosome associated. Anti-ubiquitin pull-down showed broadly increased ubiquitinated species (PFF/Lpf vs. Lpf control) and an accumulation of ubiquitinated reporter, migrating as an HMW smear (Figure S3I). To assess lysosomal association, we performed lysosome immunoprecipitation (Lyso-IP) with a hemagglutinin (HA)-tagged lysosomal membrane protein, TMEM192,[130] enriching the lysosomal marker LAMP1 but not other subcellular markers (Figure S3J). Lyso-IP recovered more reporter after aggregation induction, reflecting its increased abundance in the input (Figure S3J). These data support α-syn aggregation stabilizing the reporter in a ubiquitinated and lysosome-associated state, consistent with reduced ESCRT-III availability.

When two perturbations converge on a common target, they produce synergistic phenotypes.[131,132] We leveraged this principle to determine whether ESCRT-III knockdown and α-syn aggregation stabilize the ESCRT reporter in the same way. To avoid saturating the reporter, we used a mild CHMP2A/B double knockdown (59% for CHMP2A and 48% for CHMP2B; Figures S3K and S3L) that did not yield significant stabilization (Figure 3F; bars 1 and 3). Aggregation induction produced 1.5-fold stabilization (Figure 3F; bars 1 and 2). Combined, the two perturbations synergized to stabilize the reporter 3.1-fold (Figure 3F; bars 1 and 4). As a control, combining α-syn aggregation with E1 ubiquitin-activating (E1) enzyme inhibition, a

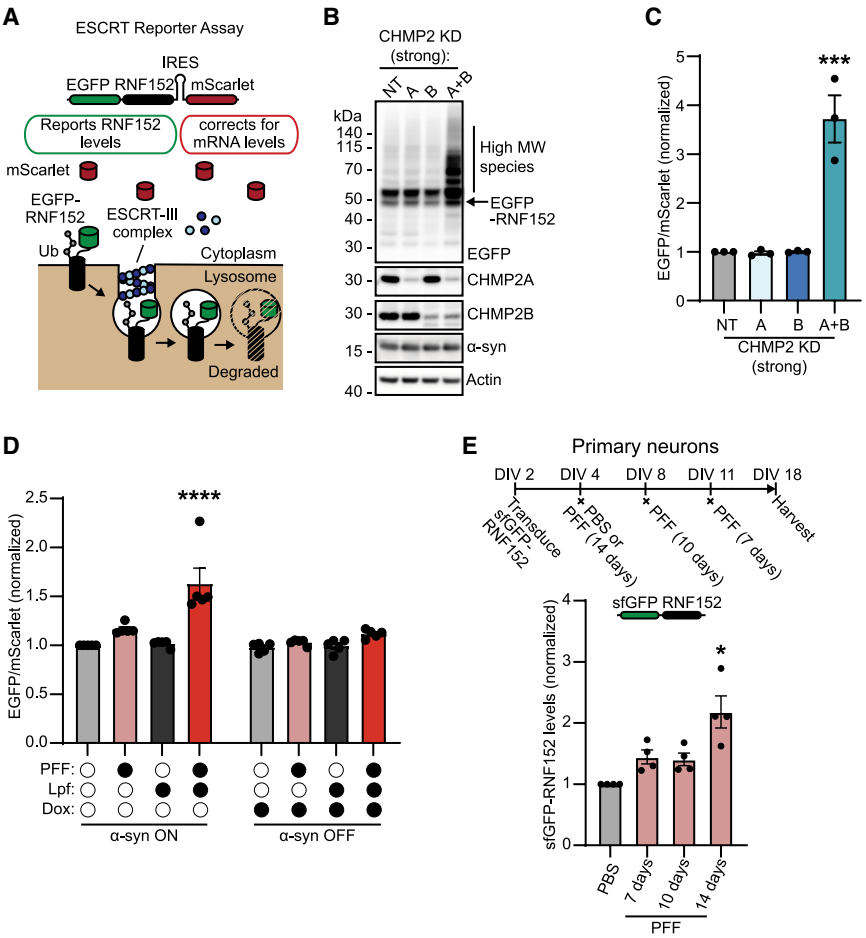

Figure 3. α-Syn aggregation inhibits ESCRT

(A) ESCRT reporter assay schematic. HEK α-syn cells express EGFP-RNF152 alongside IRES-driven mScarlet. mScarlet controls reporter expression; EGFP tracks RNF152 degradation. EGFP, enhanced green fluorescent protein; IRES, internal ribosome entry site.

(B) Representative ESCRT reporter immunoblot with strong CHMP2A and CHMP2B knockdown, stained for GFP, CHMP2A, CHMP2B, α-syn, and β-actin (loading control). Quantified in Figure S3D ($n = 3$). KD, knockdown; NT, non-targeting control.

(C and D) ESCRT reporter flow cytometry after strong CHMP2A and CHMP2B knockdown, normalized to NT (C) or after aggregation induction, normalized to untreated control (D). Error bars: mean ± SEM. ($n = 3$ in C and $n = 5$ in D).

(E) Densitometric quantification of full-length sfGFP-RNF152 in primary neurons, treated according to the timeline above, values normalized to GAPDH and PBS control. Mean ± SEM shown ($n = 4$). Supporting immunoblot in Figure S3H.

(F) ESCRT reporter flow cytometry measures the effect of combining either α-syn aggregation (PFF/Lpf vs. Lpf) with mild CHMP2A/B knockdown or E1 enzyme inhibitor. Data normalized to appropriate controls (Lpf/NT or Lpf/DMSO). Mean ± SEM shown ($n = 3$ or 5). Arrows: expected values from additive effects. Supporting immunoblots and quantification in Figures S3K and S3L.

$^*p < 0.05$; $^{**}p < 0.01$; $^{***}p < 0.001$; $^{****}p < 0.0001$ by one-way (C and E) or two-way (D and F) ANOVA. See also Figure S3.

perturbation mechanistically unrelated to impaired ESCRT function, showed no synergy (Figure 3F; bars 5 and 8). This synergy between CHMP2 knockdown and α-syn aggregation is consistent with both perturbations limiting ESCRT-III availability, thereby reducing ESCRT function.

Interaction with aggregated α-syn targets ESCRT-III for collateral degradation

We considered two ways in which α-syn aggregation could diminish ESCRT-III availability. First, aggregate sequestration may immobilize ESCRT-III subunits, restricting them from reaching sites of action. Second, aggregation may reduce ESCRT-III protein levels, as we observed CHMP2B levels to decline by half in HEK cells and primary neurons upon aggregation (Figures 1B and S1D–S1F). Induction of α-syn aggregation additionally lowered CHMP2A and CHMP3 in HEK cells but not CHMP4B or CHMP6 (Figures S4A and S4B). We next investigated how aggregation drives this reduction in ESCRT-III proteins.

To explore the interplay between α-syn aggregation and ESCRT-III depletion, we PFF-treated HEK α-syn cells and measured CHMP2B levels. We omitted Lpf to slow the pace of aggregation and better measure its onset. By immunoblot, CHMP2B levels declined only after α-syn aggregates appeared (HMW SDS-resistant smears), continuing to drop through day 6 (Figure 4A). Additionally, silencing α-syn expression with Dox after PFF exposure attenuated α-syn aggregation and CHMP2B loss (Figure 4B). These results establish that α-syn aggregate formation precedes reduction of ESCRT-III levels.

Considering α-syn inclusions contain strong ubiquitin and CHMP2B signal (Figures 1C and S1A), we hypothesized that CHMP2B is degraded ubiquitin-dependently, perhaps resulting

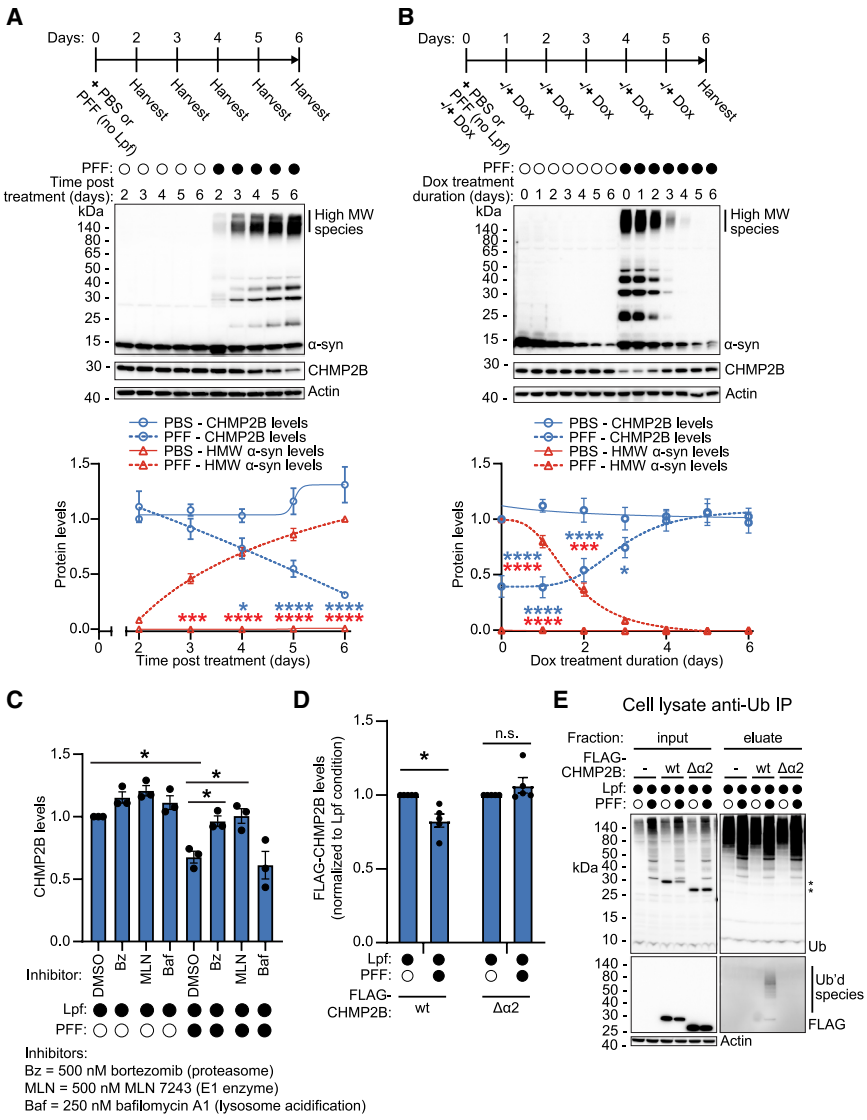

Figure 4. Interaction with aggregated α-syn targets ESCRT-III for collateral degradation

(A and B) Representative HEK α-syn cell immunoblots after PBS or PFF treatment for (A) increasing amounts of time or (B) 6 days with Dox addition at different times (see timeline above). In (B), "6 days" means Dox added on day 0, "5 days" = day 1, etc. Immunoblots were stained for α-syn, CHMP2B, and β-actin (loading control). Densitometry below: CHMP2B values normalized to first time point; α-syn values normalized to maximum—6 days in (A), 0 days in (B). Error bars: mean ± SEM (n = 3). Pairwise statistical comparisons shown for CHMP2B (blue) and HMW α-syn (red) at matched time points.

(C) Densitometric CHMP2B quantification after 8 h inhibitor treatment ± aggregation induction in HEK α-syn cells (see Figure S4C immunoblot). Data normalized to β-actin then to Lpf/DMSO control. Error bars: mean ± SEM (n = 3).

(D) Densitometric FLAG-CHMP2B variant quantification (immunoblots in Figure S4E) ± aggregation induction in HEK α-syn cells. Values normalized to β-actin then to Lpf control for each variant. Error bars: mean ± SEM (n = 5).

(E) Representative anti-ubiquitin (Ub) pull-down immunoblots from HEK α-syn lysates expressing FLAG-CHMP2B variants, stained for ubiquitin, FLAG, and β-actin (loading control). Asterisks: persistent FLAG-CHMP2B signal after re-probing (n = 2).

n.s. $p > 0.05$; *$p < 0.05$; ***$p < 0.001$; ****$p < 0.0001$ by two-way ANOVA.

See also Figure S4.

from an α-syn-targeting E3 ligase nonspecifically ubiquitinating α-syn-bound CHMP2B. Indeed, inhibiting E1 enzymes or the proteasome rescued CHMP2B levels, whereas inhibiting lysosome acidification did not (Figures 4C and S4C). Furthermore, anti-ubiquitin immunoprecipitation recovered more ubiquitinated CHMP2B after aggregation induction; unmodified CHMP2B additionally co-purified, suggesting that non-ubiquitinated CHMP2B may be complexed with ubiquitinated cellular material (Figure S4D). Thus, α-syn aggregation triggers ubiquitination and proteasomal degradation of CHMP2B.

To test whether ESCRT-III degradation relies on binding α-syn aggregates, we induced aggregation after overexpressing either FLAG-tagged WT CHMP2B or the α2 deletion mutant observed to have diminished aggregate binding (Figure 2C). Although induction of aggregation reduced WT FLAG-CHMP2B levels and increased its ubiquitination, the α2 mutant was unaffected (Figures 4D, 4E, and S4E), indicating that CHMP2B degradation requires aggregate binding. Interestingly, overexpression of WT FLAG-CHMP2B lessened endogenous CHMP2B degradation but the non-degraded α2 mutant did not, suggesting a saturable degradation pathway (Figures S4E and S4F). Saturation would explain why cells degrade overexpressed FLAG-CHMP2B less than endogenous CHMP2B (17% vs. 38%, Figures 4D, S4E, and S4F).

These data suggest that interaction with α-syn aggregates triggers degradation of CHMP2B and, by extension, other ESCRT-III subunits. We refer to this as collateral degradation, as degradation is a collateral consequence of aggregate binding. Alongside sequestration, this mechanism contributes to functional ESCRT-III depletion.

α-Syn aggregation impairs endolysosomal homeostasis

The findings above suggested that α-syn aggregation, by compromising ESCRT-III function, may impair endolysosome membrane integrity. Perforating these membranes exposes lumenal β-galactoside sugars to the cytoplasm, causing clustering of Galectin proteins on the membrane.[133–137] To assess endolysosome membrane integrity, we expressed an mRuby3-Gal3 and mClover3-Gal3 fluorescence resonance

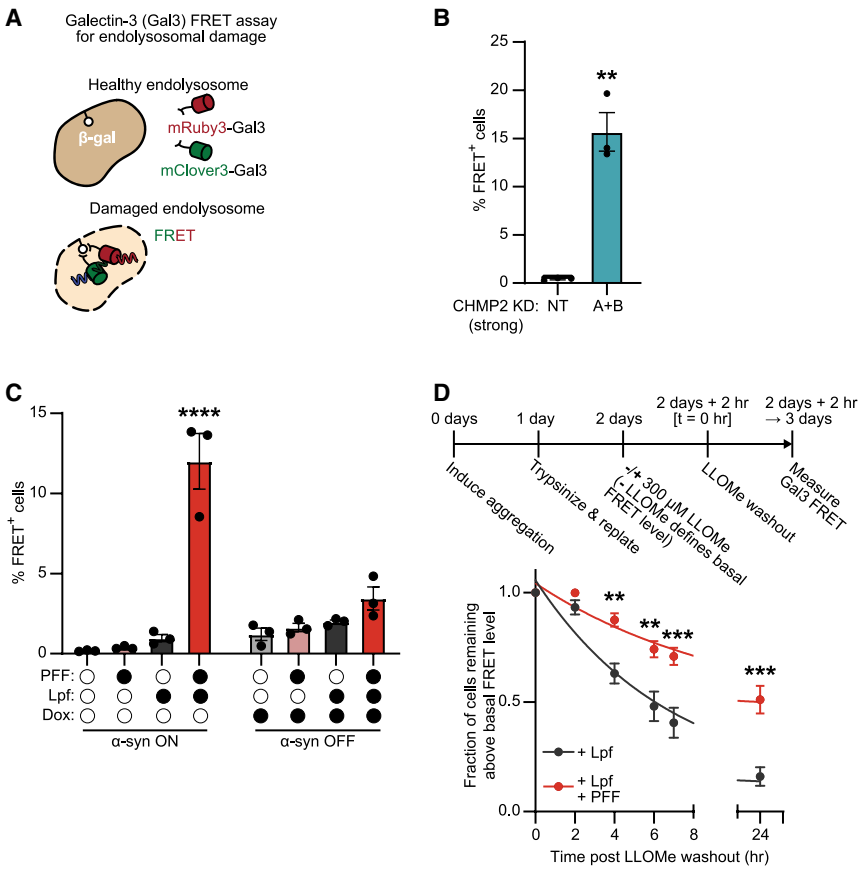

Figure 5. α-Syn aggregation impairs endolysosomal homeostasis

(A) A Gal3 FRET assay measures endolysosomal damage via clustering of mRuby3- and mClover3-Gal3 around β-galactoside sugars on perforated membranes in HEK α-syn cells.

(B and C) Gal3 FRET flow cytometry after strong CHMP2A/B knockdown (B) or α-syn aggregation induction (C). Error bars: mean ± SEM (n = 3).

(D) Gal3 FRET signal decay after brief 300 μM LLOMe treatment in cells with (PFF/Lpf) or without (Lpf) α-syn aggregates. Fraction of FRET-positive cells normalized to t = 0 within each condition. Error bars: mean ± SEM (n = 4, except t = 24 h where n = 3). Statistical comparisons shown within each time point.

$^{**}p < 0.01$; $^{***}p < 0.001$; $^{****}p < 0.0001$ by t test (B) or two-way ANOVA (C and D).

See also Figure S5.

energy transfer (FRET) pair in HEK α-syn cells (Figure 5A). As expected, L-leucyl-L-leucine methyl ester (LLOMe; a lysosome-damaging drug) increased Gal3 FRET positivity and triggered formation of Gal3 puncta that co-localized with endolysosomal markers (Figures S5A–S5C).

Consistent with ESCRT-III's role in preserving endolysosomal membrane integrity,[40,42] strong CHMP2A/B double knockdown and dominant-negative CHMP2B Q165X increased the Gal3 FRET signal, even without lysosome stress (Figures 5B and S5D). These data suggest that loss of ESCRT-III raises baseline endolysosomal damage, indicating a necessity for constant repair, consistent with a recent observation of perforated endolysosomes in unstressed neurons.[35]

To assess whether α-syn aggregation increases endolysosomal damage, we treated Gal3 reporter cells with Lpf and PFFs. Aggregate formation markedly increased Gal3 FRET positivity, whereas Lpf or PFFs alone had no effect. Dox shutoff of α-syn expression prevented the increase in FRET positivity (Figure 5C). Cells with aggregates contained prominent Gal3 puncta, appearing within and beyond aggregate regions and co-localizing with LAMP2, indicating endolysosomal damage (Figures S5E and S5F). Gal3 FRET also revealed membrane damage when α-syn aggregation was induced by 6-day PFF treatment without Lpf (Figure S5G). Thus, α-syn aggregate formation triggers endolysosomal damage, similar to direct ESCRT-III perturbation (Figure 5B).

α-Syn aggregation could increase steady-state endolysosomal damage by acting as the damaging agent, inhibiting repair or both. To measure repair, we briefly exposed cells carrying α-syn aggregates (PFF/Lpf) and control cells (Lpf) to LLOMe, then washed the drug out and followed Gal3 FRET signal decline. Although the Gal3 FRET signal decreased after LLOMe washout in both cases, the decline was slower in aggregate-bearing cells (Figure 5D), indicating diminished endolysosomal damage repair upon α-syn aggregation.

Together, these results support a model wherein endolysosomes exist in a balance between damage and repair, with ESCRT-III facilitating repair. α-Syn aggregates disturb the balance, sequestering ESCRT-III subunits and targeting them for degradation, compromising endolysosome repair. We cannot rule out aggregates themselves additionally causing endolysosomal damage. Nonetheless, impaired ESCRT-III-mediated repair would amplify this damage.

ESCRT functional disruption exacerbates seeded α-syn aggregation

α-Syn fibrils can enter cells by endocytosis, binding cell surface receptors before trafficking through early and late endosomes to reach lysosomes.[24,25,28–30] Accordingly, Alexa 647-labeled PFFs co-localized with early endosomes after 15 min of incubation and with late endosomes/lysosomes after 4 h in HEK cells (Figure S6A). We wondered whether endolysosomal damage triggered by ESCRT-III disruption could liberate such fibrils from endolysosomes, allowing them to seed intracellular α-syn aggregation.

To measure seeded α-syn aggregation, we constructed a HEK cell line expressing two A53T α-syn variants, tagged with FRET donor mClover3 or acceptor mRuby3 (Figure 6A). PFF/Lpf treatment produced 68% FRET-positive cells within 2 days

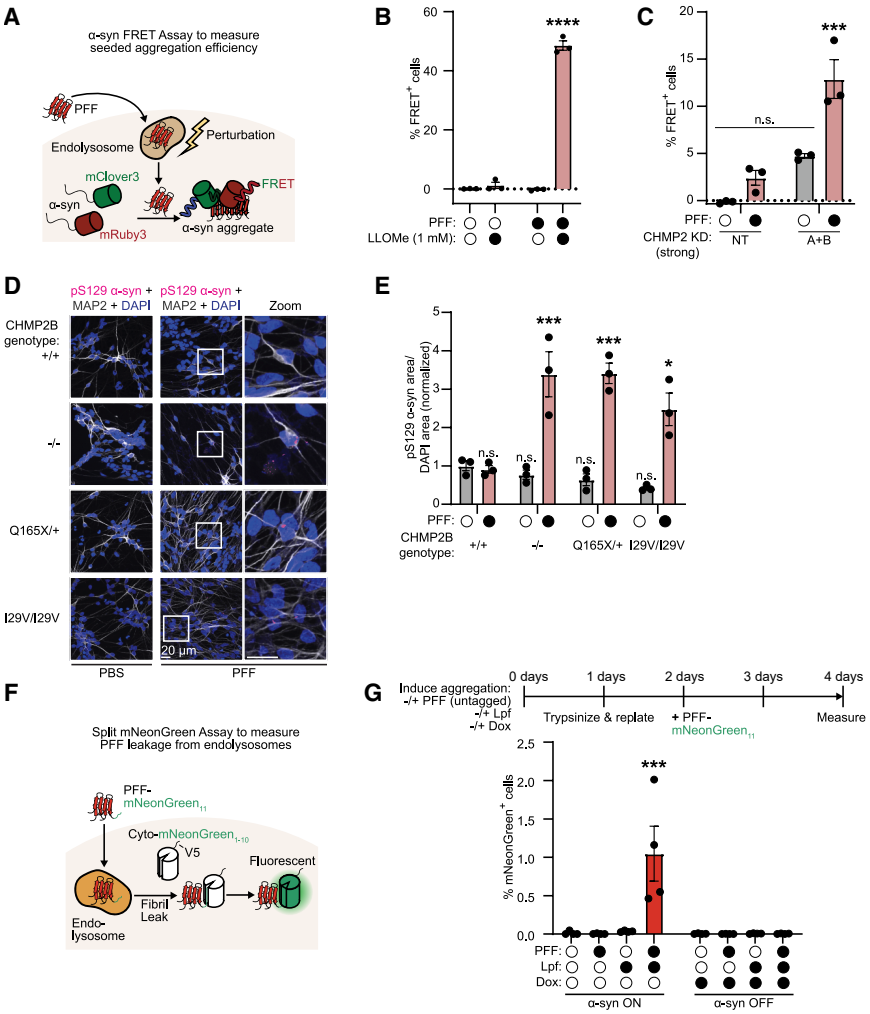

Figure 6. ESCRT-III disruption and α-syn aggregation cause fibril leakage from endolysosomes

(A) α-Syn FRET assay schematic: α-syn-mClover3 and α-syn-mRuby3 aggregation in PFF-treated HEK cells produces FRET, measured by flow cytometry.

(B and C) α-Syn FRET assay in cells treated with PFFs, then 1 h later with LLOMe (B), or treated with PFFs after strong CHMP2A/B knockdown (C). Error bars: mean ± SEM (n = 3).

(D and E) Representative immunofluorescence (D) of CHMP2B-mutant iNeurons, stained for pS129 α-syn and MAP2, after 7-day PFF treatment from DIV16-DIV23. Quantification appears in (E). Error bars: mean ± SEM (n = 3). Comparisons relative to untreated CHMP2B$^{+/+}$ control. DIV, days *in vitro*.

(F) Split mNeonGreen PFF leakage assay schematic: HEK α-syn cells expressing cyto-mNeonGreen$_{1–10}$ are treated with PFF-mNeonGreen$_{11}$. Cytoplasmic leakage produces fluorescence complementation. V5-tagging cyto-mNeonGreen$_{1–10}$ permits visualization independently of complementation.

(G) Split mNeonGreen PFF leakage assay after pre-treating cells to induce aggregation, followed by treatment with PFF-mNeonGreen$_{11}$. Error bars: mean ± SEM (n = 4).

(H) Representative immunofluorescence micrographs of complemented mNeonGreen localization in selected conditions from (G), stained for pS129 α-syn (arrowheads mark inclusions) and V5 (total cyto-mNeonGreen$_{1–10}$).

n.s. $p > 0.05$; *$p < 0.05$; ***$p < 0.001$; ****$p < 0.0001$ by two-way ANOVA.

See also Figures S6 and S7.

(Figure S6B), similar to untagged α-syn aggregation (Figure 1B). This FRET increase coincided with filter-retained aggregate material recognized by anti-GFP (detecting mClover3) and anti-pS129 α-syn antibodies (Figure S6C). mClover3- and mRuby3-positive inclusions also formed, staining for classical α-syn aggregation markers (Figure S6D). Thus, the α-syn FRET signal reflects *bona fide* α-syn aggregate formation.

We then employed the α-syn FRET cells to test whether endolysosomal damage facilitates seeded aggregation. To ensure that PFFs enter cells through the physiologic endocytic route, we omitted Lpf in these assays (Figure 6A). PFFs alone had little effect after 2 days, but combined PFF/LLOMe treatment massively increased FRET positivity, reflecting intracellular α-syn aggregation (Figure 6B). Endolysosomal perforations therefore permit PFFs to efficiently seed intracellular α-syn aggregation. In contrast, seeding without perforation is slow, potentially due to low seed transfer to the cytoplasm (Figure 4A).

Next, we investigated whether ESCRT-III perturbation facilitates α-syn seeding similarly to LLOMe. CHMP2A/B double knockdown significantly increased FRET positivity after PFF treatment without Lpf, also generating a minor non-significant FRET-positive population even without PFFs (Figure 6C). Furthermore, dominant-negative CHMP2B Q165X also enhanced PFF seeding, whereas WT CHMP2B did not (Figure S6E). Thus, perturbation of ESCRT-III, which causes endolysosomal damage (Figure 5B), also exacerbates templated α-syn aggregation.

Notably, CHMP2A/B double knockdown did not affect PFF-induced aggregation when Lpf was present (Figure S6F), suggesting cytosolic entry of seeds is not limiting for seeding in this condition. This observation validates Lpf as a tool to study how α-syn aggregation affects ESCRT without confounding effects on cytoplasmic entry.

To determine whether ESCRT-III loss enhances α-syn seeding in neurons, we disrupted ESCRT-III in induced pluripotent stem cells (iPSCs) before differentiation into iNeurons by NGN2-driven reprogramming.[138] Using endogenous α-syn levels to avoid a saturating seeding regime, preliminary findings showed that CHMP2B deletion alone produced a clear phenotype in iNeurons. We used CRISPR-Cas9 (or Cpf1) to generate CHMP2B$^{-/-}$ cells, in addition to lines containing dominant disease-associated mutations—CHMP2B$^{Q165X/+}$ and CHMP2B$^{I29V/I29V}$; all lines differentiated normally, marked by reduced OCT4 and increased Synapsin I expression over time (Figures S6G–S6I). Although PFFs did not efficiently seed the parental line (without Lpf), all CHMP2B mutations facilitated pS129 α-syn inclusion formation (Figures 6D and 6E). We obtained similar results in primary neurons, where 4-day PFF treatment only yielded pS129 α-syn inclusions upon CHMP2B short hairpin RNA (shRNA) knockdown (Figures S6J–S6M; 53% knockdown), indicating that CHMP2B loss alone facilitates α-syn seeding in neurons.

In summary, PFFs can escape from endolysosomes to seed the aggregation of soluble α-syn. ESCRT-III proteins maintain endolysosomal homeostasis to limit seeding. Loss of ESCRT-III function thus increases seeding efficiency.

α-Syn aggregation enhances leakage of exogenous fibrils into the cytoplasm

Our findings suggest that α-syn aggregates sequester ESCRT-III members and trigger their degradation, inhibiting their ability to maintain endolysosomal integrity. We hypothesized that endolysosome homeostasis collapse triggered by α-syn aggregation would increase leakage of endocytosed fibrils into the cytoplasm. These secondary fibril leaks could provide additional seeding templates, accelerating α-syn conversion into aggregates. This model predicts that cells with aggregates should leak more endocytosed fibrils into the cytoplasm than cells without aggregates do.

To test this hypothesis, we developed a flow-cytometry-based fluorescence complementation assay using split mNeonGreen.[139] We generated exogenous PFFs fused to the final β-strand of mNeonGreen (PFF-mNeonGreen$_{11}$) and expressed β-strands 1–10 in the cytoplasm (cyto-mNeonGreen$_{1–10}$) of HEK α-syn cells (see STAR Methods; Figure 6F). Cytoplasmic delivery of PFF-mNeonGreen$_{11}$ with Lpf resulted in mNeonGreen fluorescence and mNeonGreen-positive inclusions (Figures S7A and S7B). The fluorescence signal developed in fewer cells (18%) than what we observed by α-syn FRET (68%; Figure S6B), potentially due to steric effects of the fibrils limiting fluorescence complementation. Inclusions were mostly double-positive for mNeonGreen and pS129 α-syn but singly positive inclusions also appeared (Figure S7C). mNeonGreen-negative, pS129 α-syn-positive inclusions may reflect inefficient complementation or secondary aggregation via primary aggregate fragmentation or secondary nucleation.[140–143] mNeonGreen-positive, pS129 α-syn-negative puncta could represent PFF-mNeonGreen$_{11}$ fibrils that have complemented with cyto-mNeonGreen$_{1-10}$ but not seeded phosphorylated aggregates. We also detected fluorescence complementation without Lpf when we disrupted ESCRT-III with CHMP2B Q165X (Figure S7D), confirming that the assay detects PFF leakage from endolysosomes after loss of ESCRT-III function.

We next tested the prediction that α-syn aggregation facilitates fibril leakage. We first pre-treated cells with untagged PFFs and Lpf to generate α-syn aggregates that were not detectable by the split mNeonGreen assay (Figures 6G, S7A, and S7B), then added PFF-mNeonGreen$_{11}$ without Lpf. We only detected fluorescence complementation when adding PFF-mNeonGreen$_{11}$ to cells with pre-existent aggregates (PFF/Lpf pre-treatment), an effect abolished by α-syn-silencing Dox treatment (Figure 6G). The resultant mNeonGreen puncta co-localized with pS129 α-syn inclusions (Figure 6H). As expected, leakage was lower than that caused by direct ESCRT-III perturbation with CHMP2B Q165X (Figures 6G and S7D). mNeonGreen-positive cells with leaked PFF-mNeonGreen$_{11}$ excluded a membrane-impermeable dye, unlike saponin-treated cells (Figure S7E), indicating that α-syn aggregation promotes cytoplasmic entry of endocytosed fibrils through damaged endolysosomes, rather than ruptured plasma membranes.

To assess whether cytoplasmic fibril leakage promotes further aggregation, we expressed YFP-tagged Tau repeat domain containing FTD mutations P301L/V337M (“TauRD”) alongside α-syn. After inducing α-syn aggregation for 2 days, we added TauRD-PFFs and observed TauRD-YFP inclusions in 36% of cells—an effect not seen with either TauRD-PFFs or α-syn aggregation alone (Figures S7F and S7G). Although some TauRD-YFP inclusions co-localized with α-syn, others localized to distal areas like the nucleus. Notably, the 36% seeding rate exceeds the frequency of cells showing fibril leakage or Gal3-reported endolysosomal damage (1% and 12%, respectively; Figures 5C, 6G, and S7G). The discrepancy may reflect the self-amplifying nature of TauRD aggregation enhancing the sensitivity of the seeding assay and/or further damage to endolysosomal membranes. These results nonetheless indicate that α-syn aggregation exacerbates fibrillar seed leakage, facilitating a second wave of templated aggregation.

DISCUSSION

This study uncovers the cell biological implications of the clinically observed co-localization between CHMP2B and neurodegeneration-associated inclusions, specifically α-syn.[85–89,91] CHMP2B binds fibrillar, but not monomeric, α-syn via its α2 helix (Figures 2B–2F and S2B–S2D). Consequently, α-syn aggregates sequester CHMP2B and other ESCRT-III proteins, including CHMP2A, CHMP3, and CHMP4B, with similar helices (Figures 1C, 1D, 7A–7C, and S1G). Aberrant interaction with α-syn aggregates triggers collateral degradation of ESCRT-III subunits by the proteasome (Figures 4A–4E, 7C, and S4A–S4F). α-syn aggregation thereby depletes the ESCRT-III subunit pool, inhibiting ESCRT function and endolysosomal repair. Aggregates may also directly destabilize these membranes,[24,32,144,145] hastening endolysosomal homeostasis collapse (Figures 7C and 7D). Accordingly, cells carrying inclusions accumulate endolysosome membrane damage and leak endocytosed fibrils into the cytoplasm, promoting further

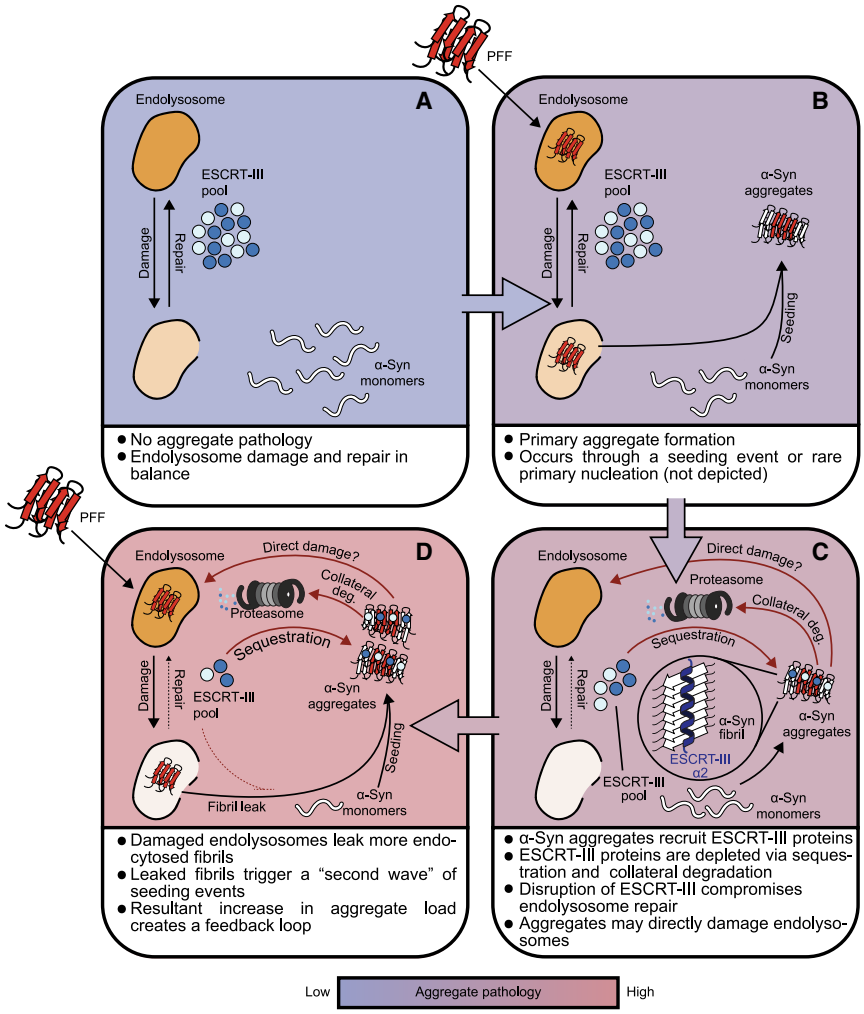

Figure 7. Working model of a feedback loop connecting α-syn aggregation and ESCRT-III inhibition

(A) Healthy cells: α-syn is soluble and ESCRT-III proteins repair endolysosomal damage.

(B) α-Syn aggregate pathology initiation: primary aggregate forms via seeding or primary nucleation.

(C) Sequestration: ESCRT-III proteins bind aggregates via helix α2. This interaction immobilizes ESCRT-III proteins and targets them for collateral degradation, functionally depleting ESCRT-III and compromising endolysosomes. Aggregates may additionally directly damage endolysosomal membranes.

(D) Feedback: compromised endolysosomes leak fibrils, triggering a "second wave" of seeding. Aggregation kinetics increase, further perturbing ESCRT-III and forming a feedback loop. Below, scale bar indicating the degree of aggregate pathology across panels.

seeding events that increase aggregate burden and complete a feedback loop of α-syn aggregation, ESCRT disruption, endolysosomal damage, and further aggregation (Figures 6G, 7D, S7F, and S7G).

Experimental systems for cell biological analysis of α-syn aggregation

Key to our investigation was a cellular system that controlled α-syn aggregation, using inducible α-syn expression, PFFs, and Lpf (Figure 1A). This control allowed precise analysis of how α-syn aggregation impacts specific phenotypes. Notably, ESCRT-III-sequestering inclusions of intracellular α-syn had the strongest effect, whereas α-syn expression or brief PFF treatment alone caused minimal disruption (Figures 1B, 3D, 5C, 6G, S1D, S3G, and S5G). Silencing α-syn expression reduced toxicity, highlighting its therapeutic potential.[146]

Because feedback loops amplify inputs, isolating each segment experimentally requires severing the loop. Lpf permitted α-syn aggregate seeding at saturation, unaffected by further ESCRT-III perturbation (Figure S6F), which was crucial for untangling the feedback mechanism. This approach enabled us to measure combined effects of aggregation and CHMP2 knockdown (Figure 3F), without impaired ESCRT function leading to increased aggregation and amplifying the effect. We nonetheless controlled for Lpf throughout and reproduced key results under Lpf-independent conditions.

Sequestration and collateral degradation functionally deplete ESCRT-III

ESCRT-III proteins associate with α-syn aggregates and become functionally depleted in two ways. First, spatial confinement may prevent ESCRT-III subunits from reaching their site of action. Second, sequestration causes collateral degradation of ESCRT-III proteins alongside α-syn.

In patient brains, ESCRT-III proteins co-localize with α-syn.[86,87,89] How this interaction originates remains unclear. Recent evidence indicates that endocytosed Tau fibrils tear endolysosomal membranes and protrude into the cytoplasm, templating the misfolding of monomeric Tau on the other side of the membrane. These membrane damage sites also recruit ESCRT-III repair machinery.[34] If α-syn aggregates originate similarly, early α-syn-ESCRT-III interactions may occur at these membrane lesions. However, CHMP2B can bind aggregated α-syn independently of membranes (Figures 2B, S2B, and S2C), suggesting that cytoplasmic ESCRT-III proteins may also bind aggregates formed distally, via fibril fragmentation or secondary nucleation.[140–143]

Our results indicate that ESCRT-III proteins specifically bind aggregated α-syn (Figures 1C, 1D, 2A–2C, 2F, S1C, S1G, and S2A). Contrary to a recent report,[90] we detected no interaction between CHMP2B and soluble α-syn (Figures 2A–2C and S2A). This aggregation-specific interaction mapped to

CHMP2B$_{\alpha2}$, spanning residues 55–96 (Figures 2C–2E and S2B–S2D), which forms an extended α2/3 hydrophobic interface between protomers in ESCRT-III oligomer structures.[47,51,53,147] We speculate that α2 recognizes α-syn fibrils, docking its hydrophobic face into a hydrophobic groove on the fibril surface (Figures S2I–S2K). α2 also binds other amyloid proteins (Figure 2F), suggesting that it and, by extension, CHMP2B[85–89,91] recognize a shared feature of amyloid folds. Its broad recognition and compact size could make α2 a promising scaffold for delivering therapeutics to amyloid fibrils across diseases.

All ESCRT-III complex structures feature this extended α2/3 helical binding motif,[47,51,53,147] potentially explaining why α-syn sequesters other ESCRT-III proteins beyond CHMP2B. Although this study focused on CHMP2B and its paralog CHMP2A, we also detected CHMP3 and CHMP4B recruitment to α-syn aggregates (Figure S1G). α-Syn aggregation may broadly impair ESCRT-III by targeting multiple subunits.

As in DLB patients,[86] we observed that α-syn aggregation reduced CHMP2B and several other ESCRT-III subunit levels (Figures 1B and S4A). Inhibiting ubiquitination or the proteasome suppressed the decrease, as did mutating the α-syn binding site on CHMP2B (Figures 4C–4E, S4C, S4E, and S4F). Furthermore, excess collateral degradation substrates saturated the pathway (Figures S4E and S4F) by competing with endogenous CHMP2B for α-syn binding or for recognition by E3 ligases. Thus, the loss of CHMP2B (and other ESCRT-III proteins) results from ubiquitination after co-aggregation with α-syn.

During aggregate clearance, E3 ligases may spuriously ubiquitinate nearby CHMP2B when targeting α-syn. As aggregates constantly form and become ubiquitinated, they therefore serve as a sink for ESCRT-III proteins, functionally depleting ESCRT-III. E3 ligases incidentally ubiquitinate collaborating E1 and E2 enzymes,[148] but, to our knowledge, such inadvertent ubiquitination has not been reported for aggregate-bound proteins.

For optimal activity, ESCRT-III subunits must assemble in a choreographed sequence.[36–39,41,43,46] Disturbing this coordination with imbalanced subunit ratios impairs ESCRT-III function.[116] Even partial reduction of several ESCRT-III species could thereby exert outsized impacts on ESCRT-III oligomerization. If ESCRT disruption is due to such imbalances, increasing one subunit alone is unlikely to restore function. Attempts at ameliorating the effect of α-syn aggregation on ESCRT function might be better invested in blocking the α-syn-ESCRT-III interaction, inhibiting collateral degradation or fortifying endolysosome homeostasis through ESCRT-independent means.

ESCRT disruption drives endolysosomal dysfunction in PD

Mutations in several PD-linked genes with diverse functions converge on the endolysosome,[149–152] highlighting its central role in PD and suggesting that wide-ranging endolysosomal stressors promote disease pathogenesis. Clinical evidence of ESCRT-III sequestration[86,87,89] and our findings position ESCRT disruption as a driver of α-syn-related endolysosomal dysfunction. Feedback between endolysosomes, ESCRT, and α-syn aggregation (Figure 7) may amplify other endolysosomal stressors, augmenting their contribution to PD.

An emergent property of the feedback loop described here is that cells carrying α-syn inclusions tend to leak endocytosed fibrils into the cytoplasm (Figure 7D). It is intuitive how ESCRT dysfunction resulting from α-syn aggregation might be toxic. Yet, the consequences of increased endolysosome leakiness are less apparent. Leakiness may usher a "second wave" of α-syn seeding events, accelerating aggregation and endolysosomal proteostasis decline (Figures 7D, S7F, and S7G). Damaged endolysosomes could spill other proteins into the cytoplasm, such as Tau fibrils. PD and other synucleinopathies commonly feature Tau comorbidity.[153–156] Leakage of Tau fibrils into the cytoplasm of α-syn inclusion-bearing cells (Figures S7F and S7G) could facilitate the propagation of Tau co-pathology. Understanding the pathological importance of this leakiness will require animal studies.

Limitations of the study

We identified the α-syn binding region of CHMP2B and its physico-chemical properties (Figures 2C–2F, S2B–S2D, and S2G–S2K), but the precise fibril-specific binding mechanism could not be resolved within this study. Structural information on CHMP2B in complex with fibrils is therefore absent from our current dataset, limiting our insight into the structural basis for sequestration-induced ESCRT-III inhibition.

Sequestration via α2 couples α-syn aggregation to ESCRT-III functional depletion (Figure 7). HEK cell experiments revealed the mechanism of the ensuing feedback loop. Limited primary neuron culture longevity and inefficient iNeuron seeding (Figure 6E) limited our ability to track outcomes downstream of ESCRT-III inhibition, including endolysosomal damage and fibril leakage. Neuronal experiments nonetheless supported the central feedback loop model: aggregation disrupts ESCRT-III by sequestration and collateral degradation, and this disruption facilitates seeded α-syn aggregation (Figures 1D, 6D, 6E, S1F, S6L, and S6M).

Collateral degradation plays a key role in our feedback loop model (Figure 7). However, we have not yet identified the responsible E3 ligase(s), the α-syn species where ubiquitination takes place (e.g., small nuclei or mature fibrils), and how ubiquitinated substrates access the proteasome (e.g., passive dissociation or motor-driven removal). Although ascertaining this information would give a clearer mechanistic picture, our study still positions collateral degradation as a key toxic outcome of α-syn aggregation.

RESOURCE AVAILABILITY

Lead contact

Further information and requests for resources and reagents should be directed to, and will be fulfilled by, the lead contact, F. Ulrich Hartl (uhartl@biochem.mpg.de).

Materials availability

Plasmids generated in this study are available on Addgene. HEK cell lines from this study are available upon request to the lead contact, pending completed material transfer agreements from the Max Planck Institute of Biochemistry. CHMP2B-mutant iPSC lines can be provided by J.W.H. (wade_harper@hms.harvard.edu), pending completed material transfer agreements from Harvard Medical School and the Jackson Laboratory, which holds the rights to the parental iPSC line.

Data and code availability

All raw and processed data are publicly available at Zenodo as Zenodo: https://doi.org/10.5281/zenodo.14506781. All original code has been deposited at GitHub and Zenodo, available via the permanent identifiers Zenodo: https://doi.org/10.5281/zenodo.14411900, https://doi.org/10.5281/zenodo.14411929, https://doi.org/10.5281/zenodo.14411941, https://doi.org/10.5281/zenodo.14411935, https://doi.org/10.5281/zenodo.14637057, https://doi.org/10.5281/zenodo.15489358, https://doi.org/10.5281/zenodo.15489352. Any additional information required to reanalyze the data in this paper is available from the lead contact upon request.

ACKNOWLEDGMENTS

We thank MPIB Imaging Facility (RRID: SCR_025739) staff Martin Spitaler, Giovanni Cardone, and Markus Oster and the Core for Imaging Technology & Education (CITE) at Harvard Medical School for imaging help; Carolin Klose, Nadine Wischnewski, Silvia Gaertner, and Romy Lange for protein purification; Stephan Uebel and Stefan Pettera at the MPIB Biochemistry Core Facility (RRID: SCR_025743) for peptide synthesis; and Martin Mueller for comments on the manuscript. This work was supported by the Deutsche Forschungsgemeinschaft (DFG; German Research Foundation) under Germany's Excellence Strategy within the framework of the Munich Cluster for Systems Neurology (grant number EXC 2145 SyNergy—ID 390857198 to F.U.H.), the Max Planck Foundation, and by the joint efforts of the Michael J. Fox Foundation for Parkinson's Research (MJFF) and the Aligning Science Across Parkinson's (ASAP) initiative (to F.U.H. and J.W.H.). MJFF administers the grants ASAP-000282 and ASAP-024268 on behalf of ASAP and itself. C.S.S. was supported by an EMBO Long Term Fellowship (grant number ALTF 360-2020).

AUTHOR CONTRIBUTIONS

C.S.S. planned and performed experiments and analyzed data alongside V.A.T., A.G., M.G., P.Y.-C., L.I., and U.D. C.S.S., V.A.T., and F.U.H. conceived the project. D.F. and J.Z. generated critical cell lines—primary mouse neurons and CHMP2B-edited iPSCs, respectively—with J.W.H. and I.D. supervising. C.S.S. and F.U.H. wrote the initial draft of the manuscript, which V.A.T., A.G., and J.W.H. critically edited. F.U.H. supervised the project.

DECLARATION OF INTERESTS

J.W.H. is a co-founder of Caraway Therapeutics, a subsidiary of Merck & Co., Inc., Rahway, NJ, USA, and is a member of the scientific advisory board for Lyterian Therapeutics.

DECLARATION OF GENERATIVE AI AND AI-ASSISTED TECHNOLOGIES IN THE WRITING PROCESS

During the preparation of this work, the authors used ChatGPT for help in condensing writing and generating protocols for protocols.io using text from the STAR Methods section. After using this tool, the authors reviewed and edited the content as needed and take full responsibility for the content of the publication.

STAR★METHODS

Detailed methods are provided in the online version of this paper and include the following:

SUPPLEMENTAL INFORMATION

Supplemental information can be found online at https://doi.org/10.1016/j.molcel.2025.08.022.

Received: January 22, 2025
Revised: July 9, 2025
Accepted: August 19, 2025
Published: September 10, 2025

REFERENCES

1. Iadanza, M.G., Jackson, M.P., Hewitt, E.W., Ranson, N.A., and Radford, S.E. (2018). A new era for understanding amyloid structures and disease. Nat. Rev. Mol. Cell Biol. *19*, 755–773. https://doi.org/10.1038/s41580-018-0060-8.
2. Jucker, M., and Walker, L.C. (2018). Propagation and spread of pathogenic protein assemblies in neurodegenerative diseases. Nat. Neurosci. *21*, 1341–1349. https://doi.org/10.1038/s41593-018-0238-6.
3. Peng, C., Trojanowski, J.Q., and Lee, V.M.Y. (2020). Protein transmission in neurodegenerative disease. Nat. Rev. Neurol. *16*, 199–212. https://doi.org/10.1038/s41582-020-0333-7.
4. Prusiner, S.B. (2013). Biology and genetics of prions causing neurodegeneration. Annu. Rev. Genet. *47*, 601–623. https://doi.org/10.1146/annurev-genet-110711-155524.
5. Vaquer-Alicea, J., and Diamond, M.I. (2019). Propagation of protein aggregation in neurodegenerative diseases. Annu. Rev. Biochem. *88*, 785–810. https://doi.org/10.1146/annurev-biochem-061516-045049.
6. Atik, A., Stewart, T., and Zhang, J. (2016). Alpha-Synuclein as a biomarker for Parkinson's disease. Brain Pathol. *26*, 410–418. https://doi.org/10.1111/bpa.12370.
7. Braak, H., Del Tredici, K., Rüb, U., de Vos, R.A.I., Jansen Steur, E.N.H., and Braak, E. (2003). Staging of brain pathology related to sporadic Parkinson's disease. Neurobiol. Aging *24*, 197–211. https://doi.org/10.1016/s0197-4580(02)00065-9.
8. Fares, M.B., Jagannath, S., and Lashuel, H.A. (2021). Reverse engineering Lewy bodies: how far have we come and how far can we go? Nat. Rev. Neurosci. *22*, 111–131. https://doi.org/10.1038/s41583-020-00416-6.
9. Rey, N.L., Wesson, D.W., and Brundin, P. (2018). The olfactory bulb as the entry site for prion-like propagation in neurodegenerative diseases. Neurobiol. Dis. *109*, 226–248. https://doi.org/10.1016/j.nbd.2016.12.013.
10. Williams-Gray, C.H., Mason, S.L., Evans, J.R., Foltynie, T., Brayne, C., Robbins, T.W., and Barker, R.A. (2013). The CamPaIGN study of Parkinson's disease: 10-year outlook in an incident population-based cohort. J. Neurol. Neurosurg. Psychiatry *84*, 1258–1264. https://doi.org/10.1136/jnnp-2013-305277.
11. Frost, B., Jacks, R.L., and Diamond, M.I. (2009). Propagation of tau misfolding from the outside to the inside of a cell. J. Biol. Chem. *284*, 12845–12852. https://doi.org/10.1074/jbc.M808759200.
12. Kfoury, N., Holmes, B.B., Jiang, H., Holtzman, D.M., and Diamond, M.I. (2012). Trans-cellular propagation of tau aggregation by fibrillar species. J. Biol. Chem. *287*, 19440–19451. https://doi.org/10.1074/jbc.M112.346072.
13. Luk, K.C., Song, C., O'Brien, P., Stieber, A., Branch, J.R., Brunden, K.R., Trojanowski, J.Q., and Lee, V.M.Y. (2009). Exogenous alpha-synuclein

fibrils seed the formation of Lewy body-like intracellular inclusions in cultured cells. Proc. Natl. Acad. Sci. USA *106*, 20051–20056. https://doi.org/10.1073/pnas.0908005106.

14. Volpicelli-Daley, L.A., Luk, K.C., Patel, T.P., Tanik, S.A., Riddle, D.M., Stieber, A., Meaney, D.F., Trojanowski, J.Q., and Lee, V.M.Y. (2011). Exogenous alpha-synuclein fibrils induce Lewy body pathology leading to synaptic dysfunction and neuron death. Neuron *72*, 57–71. https://doi.org/10.1016/j.neuron.2011.08.033.
15. Brahic, M., Bousset, L., Bieri, G., Melki, R., and Gitler, A.D. (2016). Axonal transport and secretion of fibrillar forms of α-synuclein, Aβ42 peptide and HTTExon 1. Acta Neuropathol. *131*, 539–548. https://doi.org/10.1007/s00401-016-1538-0.
16. Fontaine, S.N., Zheng, D.L., Sabbagh, J.J., Martin, M.D., Chaput, D., Darling, A., Trotter, J.H., Stothert, A.R., Nordhues, B.A., Lussier, A., et al. (2016). DnaJ/Hsc70 chaperone complexes control the extracellular release of neurodegenerative-associated proteins. EMBO J. *35*, 1537–1549. https://doi.org/10.15252/embj.201593489.
17. Jang, A., Lee, H.J., Suk, J.E., Jung, J.W., Kim, K.P., and Lee, S.J. (2010). Non-classical exocytosis of α-synuclein is sensitive to folding states and promoted under stress conditions. J. Neurochem. *113*, 1263–1274. https://doi.org/10.1111/j.1471-4159.2010.06695.x.
18. Lee, H.J., Patel, S., and Lee, S.J. (2005). Intravesicular localization and exocytosis of α-synuclein and its aggregates. J. Neurosci. *25*, 6016–6024. https://doi.org/10.1523/JNEUROSCI.0692-05.2005.
19. Wu, S., Hernandez Villegas, N.C., Sirkis, D.W., Thomas-Wright, I., Wade-Martins, R., and Schekman, R. (2023). Unconventional secretion of α-synuclein mediated by palmitoylated DNAJC5 oligomers. eLife *12*, e85837. https://doi.org/10.7554/eLife.85837.
20. Iranzo, A., Fairfoul, G., Ayudhaya, A.C.N., Serradell, M., Gelpi, E., Vilaseca, I., Sanchez-Valle, R., Gaig, C., Santamaria, J., Tolosa, E., et al. (2021). Detection of alpha-synuclein in CSF by RT-QuIC in patients with isolated rapid-eye-movement sleep behaviour disorder: a longitudinal observational study. Lancet Neurol. *20*, 203–212. https://doi.org/10.1016/S1474-4422(20)30449-X.
21. Magalhães, P., and Lashuel, H.A. (2022). Opportunities and challenges of alpha-synuclein as a potential biomarker for Parkinson's disease and other synucleinopathies. npj Parkinsons Dis. *8*, 93. https://doi.org/10.1038/s41531-022-00357-0.
22. Shahnawaz, M., Tokuda, T., Waragai, M., Mendez, N., Ishii, R., Trenkwalder, C., Mollenhauer, B., and Soto, C. (2017). Development of a biochemical diagnosis of Parkinson disease by detection of alpha-synuclein misfolded aggregates in cerebrospinal fluid. JAMA Neurol. *74*, 163–172. https://doi.org/10.1001/jamaneurol.2016.4547.
23. Siderowf, A., Concha-Marambio, L., Lafontant, D.E., Farris, C.M., Ma, Y., Urenia, P.A., Nguyen, H., Alcalay, R.N., Chahine, L.M., Foroud, T., et al. (2023). Assessment of heterogeneity among participants in the Parkinson's Progression Markers Initiative cohort using alpha-synuclein seed amplification: a cross-sectional study. Lancet Neurol. *22*, 407–417. https://doi.org/10.1016/S1474-4422(23)00109-6.
24. Dilsizoglu Senol, A., Samarani, M., Syan, S., Guardia, C.M., Nonaka, T., Liv, N., Latour-Lambert, P., Hasegawa, M., Klumperman, J., Bonifacino, J.S., and Zurzolo, C. (2021). α-Synuclein fibrils subvert lysosome structure and function for the propagation of protein misfolding between cells through tunneling nanotubes. PLoS Biol. *19*, e3001287. https://doi.org/10.1371/journal.pbio.3001287.
25. Guiney, S.J., Adlard, P.A., Lei, P., Mawal, C.H., Bush, A.I., Finkelstein, D. I., and Ayton, S. (2020). Fibrillar α-synuclein toxicity depends on functional lysosomes. J. Biol. Chem. *295*, 17497–17513. https://doi.org/10.1074/jbc.RA120.013428.
26. Karpowicz, R.J., Jr., Haney, C.M., Mihaila, T.S., Sandler, R.M., Petersson, E.J., and Lee, V.M.Y. (2017). Selective imaging of internalized proteopathic alpha-synuclein seeds in primary neurons reveals mechanistic insight into transmission of synucleinopathies. J. Biol. Chem. *292*, 13482–13497. https://doi.org/10.1074/jbc.M117.780296.
27. Lee, H.J., Suk, J.E., Bae, E.J., Lee, J.H., Paik, S.R., and Lee, S.J. (2008). Assembly-dependent endocytosis and clearance of extracellular α-synuclein. Int. J. Biochem. Cell Biol. *40*, 1835–1849. https://doi.org/10.1016/j.biocel.2008.01.017.
28. Mao, X., Ou, M.T., Karuppagounder, S.S., Kam, T.I., Yin, X., Xiong, Y., Ge, P., Umanah, G.E., Brahmachari, S., Shin, J.H., et al. (2016). Pathological α-synuclein transmission initiated by binding lymphocyte-activation gene 3. Science *353*, aah3374. https://doi.org/10.1126/science.aah3374.
29. Zhang, Q., Xu, Y., Lee, J., Jarnik, M., Wu, X., Bonifacino, J.S., Shen, J., and Ye, Y. (2020). A myosin-7B-dependent endocytosis pathway mediates cellular entry of α-synuclein fibrils and polycation-bearing cargos. Proc. Natl. Acad. Sci. USA *117*, 10865–10875. https://doi.org/10.1073/pnas.1918617117.
30. Luk, K.C., Covell, D.J., Kehm, V.M., Zhang, B., Song, I.Y., Byrne, M.D., Pitkin, R.M., Decker, S.C., Trojanowski, J.Q., and Lee, V.M.Y. (2016). Molecular and biological compatibility with host alpha-synuclein influences fibril pathogenicity. Cell Rep. *16*, 3373–3387. https://doi.org/10.1016/j.celrep.2016.08.053.
31. Chen, J.J., Nathaniel, D.L., Raghavan, P., Nelson, M., Tian, R., Tse, E., Hong, J.Y., See, S.K., Mok, S.A., Hein, M.Y., et al. (2019). Compromised function of the ESCRT pathway promotes endolysosomal escape of tau seeds and propagation of tau aggregation. J. Biol. Chem. *294*, 18952–18966. https://doi.org/10.1074/jbc.RA119.009432.
32. Flavin, W.P., Bousset, L., Green, Z.C., Chu, Y., Skarpathiotis, S., Chaney, M.J., Kordower, J.H., Melki, R., and Campbell, E.M. (2017). Endocytic vesicle rupture is a conserved mechanism of cellular invasion by amyloid proteins. Acta Neuropathol. *134*, 629–653. https://doi.org/10.1007/s00401-017-1722-x.
33. Jiang, P., Gan, M., Yen, S.H., McLean, P.J., and Dickson, D.W. (2017). Impaired endo-lysosomal membrane integrity accelerates the seeding progression of alpha-synuclein aggregates. Sci. Rep. *7*, 7690. https://doi.org/10.1038/s41598-017-08149-w.
34. Rose, K., Jepson, T., Shukla, S., Maya-Romero, A., Kampmann, M., Xu, K., and Hurley, J.H. (2024). Tau fibrils induce nanoscale membrane damage and nucleate cytosolic tau at lysosomes. Proc. Natl. Acad. Sci. USA *121*, e2315690121. https://doi.org/10.1073/pnas.2315690121.
35. Sanyal, A., Scanavachi, G., Somerville, E., Saminathan, A., Nair, A., Bango Da Cunha Correia, R.F., Aylan, B., Sitarska, E., Oikonomou, A., Hatzakis, N.S., and Kirchhausen, T. (2025). Neuronal constitutive endolysosomal perforations enable alpha-synuclein aggregation by internalized PFFs. J. Cell Biol. *224*, e202401136. https://doi.org/10.1083/jcb.202401136.
36. Henne, W.M., Stenmark, H., and Emr, S.D. (2013). Molecular mechanisms of the membrane sculpting ESCRT pathway. Cold Spring Harb. Perspect. Biol. *5*, a016766. https://doi.org/10.1101/cshperspect.a016766.
37. Lata, S., Schoehn, G., Solomons, J., Pires, R., Göttlinger, H.G., and Weissenhorn, W. (2009). Structure and function of ESCRT-III. Biochem. Soc. Trans. *37*, 156–160. https://doi.org/10.1042/BST0370156.
38. McCullough, J., Frost, A., and Sundquist, W.I. (2018). Structures, functions, and dynamics of ESCRT-III/Vps4 membrane remodeling and fission complexes. Annu. Rev. Cell Dev. Biol. *34*, 85–109. https://doi.org/10.1146/annurev-cellbio-100616-060600.
39. Migliano, S.M., and Teis, D. (2018). ESCRT and membrane protein ubiquitination. Prog. Mol. Subcell. Biol. *57*, 107–135. https://doi.org/10.1007/978-3-319-96704-2_4.
40. Radulovic, M., Schink, K.O., Wenzel, E.M., Nähse, V., Bongiovanni, A., Lafont, F., and Stenmark, H. (2018). ESCRT-mediated lysosome repair precedes lysophagy and promotes cell survival. EMBO J. *37*, e99753. https://doi.org/10.15252/embj.201899753.
41. Remec Pavlin, M., and Hurley, J.H. (2020). The ESCRTs - converging on mechanism. J. Cell Sci. *133*, jcs240333. https://doi.org/10.1242/jcs.240333.

42. Skowyra, M.L., Schlesinger, P.H., Naismith, T.V., and Hanson, P.I. (2018). Triggered recruitment of ESCRT machinery promotes endolysosomal repair. Science *360*, eaar5078. https://doi.org/10.1126/science.aar5078.

43. Vietri, M., Radulovic, M., and Stenmark, H. (2020). The many functions of ESCRTs. Nat. Rev. Mol. Cell Biol. *21*, 25–42. https://doi.org/10.1038/s41580-019-0177-4.

44. Zhang, W., Yang, X., Chen, L., Liu, Y.Y., Venkatarangan, V., Reist, L., Hanson, P., Xu, H., Wang, Y., and Li, M. (2021). A conserved ubiquitin- and ESCRT-dependent pathway internalizes human lysosomal membrane proteins for degradation. PLoS Biol. *19*, e3001361. https://doi.org/10.1371/journal.pbio.3001361.

45. Zhu, L., Jorgensen, J.R., Li, M., Chuang, Y.S., and Emr, S.D. (2017). ESCRTs function directly on the lysosome membrane to downregulate ubiquitinated lysosomal membrane proteins. eLlife *6*, e26403. https://doi.org/10.7554/eLife.26403.

46. Hurley, J.H. (2015). ESCRTs are everywhere. EMBO J. *34*, 2398–2407. https://doi.org/10.15252/embj.201592484.

47. Azad, K., Guilligay, D., Boscheron, C., Maity, S., De Franceschi, N., Sulbaran, G., Effantin, G., Wang, H.Y., Kleman, J.P., Bassereau, P., et al. (2023). Structural basis of CHMP2A-CHMP3 ESCRT-III polymer assembly and membrane cleavage. Nat. Struct. Mol. Biol. *30*, 81–90. https://doi.org/10.1038/s41594-022-00867-8.

48. Chiaruttini, N., Redondo-Morata, L., Colom, A., Humbert, F., Lenz, M., Scheuring, S., and Roux, A. (2015). Relaxation of loaded ESCRT-III spiral springs drives membrane deformation. Cell *163*, 866–879. https://doi.org/10.1016/j.cell.2015.10.017.

49. Lata, S., Roessle, M., Solomons, J., Jamin, M., Göttlinger, H.G., Svergun, D.I., and Weissenhorn, W. (2008). Structural basis for autoinhibition of ESCRT-III CHMP3. J. Mol. Biol. *378*, 818–827. https://doi.org/10.1016/j.jmb.2008.03.030.

50. Lin, Y., Kimpler, L.A., Naismith, T.V., Lauer, J.M., and Hanson, P.I. (2005). Interaction of the mammalian endosomal sorting complex required for transport (ESCRT) III protein hSnf7-1 with itself, membranes, and the AAA+ ATPase SKD1. J. Biol. Chem. *280*, 12799–12809. https://doi.org/10.1074/jbc.M413968200.

51. McCullough, J., Clippinger, A.K., Talledge, N., Skowyra, M.L., Saunders, M.G., Naismith, T.V., Colf, L.A., Afonine, P., Arthur, C., Sundquist, W.I., et al. (2015). Structure and membrane remodeling activity of ESCRT-III helical polymers. Science *350*, 1548–1551. https://doi.org/10.1126/science.aad8305.

52. Schöneberg, J., Lee, I.H., Iwasa, J.H., and Hurley, J.H. (2017). Reverse-topology membrane scission by the ESCRT proteins. Nat. Rev. Mol. Cell Biol. *18*, 5–17. https://doi.org/10.1038/nrm.2016.121.

53. Tang, S.G., Henne, W.M., Borbat, P.P., Buchkovich, N.J., Freed, J.H., Mao, Y.X., Fromme, J.C., and Emr, S.D. (2015). Structural basis for activation, assembly and membrane binding of ESCRT-III Snf7 filaments. eLlife *4*, e12548. https://doi.org/10.7554/eLife.12548.

54. Morita, E., Sandrin, V., McCullough, J., Katsuyama, A., Baci Hamilton, I., and Sundquist, W.I. (2011). ESCRT-III protein requirements for HIV-1 budding. Cell Host Microbe *9*, 235–242. https://doi.org/10.1016/j.chom.2011.02.004.

55. Lee, J.A., Liu, L., Javier, R., Kreitzer, A.C., Delaloy, C., and Gao, F.B. (2011). ESCRT-III subunits Snf7-1 and Snf7-2 differentially regulate transmembrane cargos in hESC-derived human neurons. Mol. Brain *4*, 37. https://doi.org/10.1186/1756-6606-4-37.

56. Adell, M.A.Y., Migliano, S.M., Upadhyayula, S., Bykov, Y.S., Sprenger, S., Pakdel, M., Vogel, G.F., Jih, G., Skillern, W., Behrouzi, R., et al. (2017). Recruitment dynamics of ESCRT-III and Vps4 to endosomes and implications for reverse membrane budding. eLlife *6*, e31652. https://doi.org/10.7554/eLife.31652.

57. Babst, M., Davies, B.A., and Katzmann, D.J. (2011). Regulation of Vps4 during MVB sorting and cytokinesis. Traffic *12*, 1298–1305. https://doi.org/10.1111/j.1600-0854.2011.01230.x.

58. Han, H., Monroe, N., Sundquist, W.I., Shen, P.S., and Hill, C.P. (2017). The AAA ATPase Vps4 binds ESCRT-III substrates through a repeating array of dipeptide-binding pockets. Elife *6*, e31324. https://doi.org/10.7554/eLife.31324.

59. Han, H., Monroe, N., Votteler, J., Shakya, B., Sundquist, W.I., and Hill, C.P. (2015). Binding of substrates to the central pore of the Vps4 ATPase is autoinhibited by the microtubule interacting and trafficking (MIT) domain and activated by MIT interacting motifs (MIMs). J. Biol. Chem. *290*, 13490–13499. https://doi.org/10.1074/jbc.M115.642355.

60. Hurley, J.H., and Yang, D. (2008). MIT domainia. Dev. Cell *14*, 6–8. https://doi.org/10.1016/j.devcel.2007.12.013.

61. Mierzwa, B.E., Chiaruttini, N., Redondo-Morata, L., von Filseck, J.M., König, J., Larios, J., Poser, I., Müller-Reichert, T., Scheuring, S., Roux, A., and Gerlich, D.W. (2017). Dynamic subunit turnover in ESCRT-III assemblies is regulated by Vps4 to mediate membrane remodelling during cytokinesis. Nat. Cell Biol. *19*, 787–798. https://doi.org/10.1038/ncb3559.

62. Monroe, N., Han, H., Shen, P.S., Sundquist, W.I., and Hill, C.P. (2017). Structural basis of protein translocation by the Vps4-Vta1 AAA ATPase. eLlife *6*, e24487. https://doi.org/10.7554/eLife.24487.

63. Shim, S., Merrill, S.A., and Hanson, P.I. (2008). Novel interactions of ESCRT-III with LIP5 and VPS4 and their implications for ESCRT-III disassembly. Mol. Biol. Cell *19*, 2661–2672. https://doi.org/10.1091/mbc.E07-12-1263.

64. Yang, B., Stjepanovic, G., Shen, Q.T., Martin, A., and Hurley, J.H. (2015). Vps4 disassembles an ESCRT-III filament by global unfolding and processive translocation. Nat. Struct. Mol. Biol. *22*, 492–498. https://doi.org/10.1038/nsmb.3015.

65. Jimenez, A.J., Maiuri, P., Lafaurie-Janvore, J., Divoux, S., Piel, M., and Perez, F. (2014). ESCRT machinery is required for plasma membrane repair. Science *343*, 1247136. https://doi.org/10.1126/science.1247136.

66. Scheffer, L.L., Sreetama, S.C., Sharma, N., Medikayala, S., Brown, K.J., Defour, A., and Jaiswal, J.K. (2014). Mechanism of Ca2+-triggered ESCRT assembly and regulation of cell membrane repair. Nat. Commun. *5*, 5646. https://doi.org/10.1038/ncomms6646.

67. Cox, L.E., Ferraiuolo, L., Goodall, E.F., Heath, P.R., Higginbottom, A., Mortiboys, H., Hollinger, H.C., Hartley, J.A., Brockington, A., Burness, C.E., et al. (2010). Mutations in CHMP2B in lower motor neuron predominant amyotrophic lateral sclerosis (ALS). PLoS One *5*, e9872. https://doi.org/10.1371/journal.pone.0009872.

68. Skibinski, G., Parkinson, N.J., Brown, J.M., Chakrabarti, L., Lloyd, S.L., Hummerich, H., Nielsen, J.E., Hodges, J.R., Spillantini, M.G., Thusgaard, T., et al. (2005). Mutations in the endosomal ESCRTIII-complex subunit CHMP2B in frontotemporal dementia. Nat. Genet. *37*, 806–808. https://doi.org/10.1038/ng1609.

69. van der Zee, J., Urwin, H., Engelborghs, S., Bruyland, M., Vandenberghe, R., Dermaut, B., De Pooter, T., Peeters, K., Santens, P., De Deyn, P.P., et al. (2008). CHMP2B C-truncating mutations in frontotemporal lobar degeneration are associated with an aberrant endosomal phenotype in vitro. Hum. Mol. Genet. *17*, 313–322. https://doi.org/10.1093/hmg/ddm309.

70. Keogh, M.J., Kurzawa-Akanbi, M., Griffin, H., Douroudis, K., Ayers, K.L., Hussein, R.I., Hudson, G., Pyle, A., Cordell, H.J., Attems, J., et al. (2016). Exome sequencing in dementia with Lewy bodies. Transl. Psychiatry *6*, e728. https://doi.org/10.1038/tp.2015.220.

71. Shahmoradian, S.H., Lewis, A.J., Genoud, C., Hench, J., Moors, T.E., Navarro, P.P., Castaño-Díez, D., Schweighauser, G., Graff-Meyer, A., Goldie, K.N., et al. (2019). Lewy pathology in Parkinson's disease consists of crowded organelles and lipid membranes. Nat. Neurosci. *22*, 1099–1109. https://doi.org/10.1038/s41593-019-0423-2.

72. Trinkaus, V.A., Riera-Tur, I., Martínez-Sánchez, A., Bäuerlein, F.J.B., Guo, Q., Arzberger, T., Baumeister, W., Dudanova, I., Hipp, M.S., Hartl, F.U., and Fernandez-Busnadiego, R. (2021). In situ architecture of neuronal alpha-Synuclein inclusions. Nat. Commun. *12*, 2110. https://doi.org/10.1038/s41467-021-22108-0.

73. Hipp, M.S., Kasturi, P., and Hartl, F.U. (2019). The proteostasis network and its decline in ageing. Nat. Rev. Mol. Cell Biol. *20*, 421–435. https://doi.org/10.1038/s41580-019-0101-y.

74. Yang, H., and Hu, H.Y. (2016). Sequestration of cellular interacting partners by protein aggregates: implication in a loss-of-function pathology. FEBS Journal *283*, 3705–3717. https://doi.org/10.1111/febs.13722.

75. Olzscha, H., Schermann, S.M., Woerner, A.C., Pinkert, S., Hecht, M.H., Tartaglia, G.G., Vendruscolo, M., Hayer-Hartl, M., Hartl, F.U., and Vabulas, R.M. (2011). Amyloid-like aggregates sequester numerous metastable proteins with essential cellular functions. Cell *144*, 67–78. https://doi.org/10.1016/j.cell.2010.11.050.

76. Jiang, L.L., Guan, W.L., Wang, J.Y., Zhang, S.X., and Hu, H.Y. (2022). RNA-assisted sequestration of RNA-binding proteins by cytoplasmic inclusions of the C-terminal 35-kDa fragment of TDP-43. J. Cell Sci. *135*, jcs259380. https://doi.org/10.1242/jcs.259380.

77. Riera-Tur, I., Schäfer, T., Hornburg, D., Mishra, A., da Silva Padilha, M., Fernández-Mosquera, L., Feigenbutz, D., Auer, P., Mann, M., Baumeister, W., et al. (2022). Amyloid-like aggregating proteins cause lysosomal defects in neurons via gain-of-function toxicity. Life Sci. Alliance *5*, e202101185. https://doi.org/10.26508/lsa.202101185.

78. Shao, W., Todd, T.W., Wu, Y., Jones, C.Y., Tong, J., Jansen-West, K., Daughrity, L.M., Park, J., Koike, Y., Kurti, A., et al. (2022). Two FTD-ALS genes converge on the endosomal pathway to induce TDP-43 pathology and degeneration. Science *378*, 94–99. https://doi.org/10.1126/science.abq7860.

79. Cummings, C.J., Mancini, M.A., Antalffy, B., DeFranco, D.B., Orr, H.T., and Zoghbi, H.Y. (1998). Chaperone suppression of aggregation and altered subcellular proteasome localization imply protein misfolding in SCA1. Nat. Genet. *19*, 148–154. https://doi.org/10.1038/502.

80. Guo, Q., Lehmer, C., Martínez-Sánchez, A., Rudack, T., Beck, F., Hartmann, H., Pérez-Berlanga, M., Frottin, F., Hipp, M.S., Hartl, F.U., et al. (2018). In situ structure of neuronal C9orf72 poly-GA aggregates reveals proteasome recruitment. Cell *172*, 696–705.e12. https://doi.org/10.1016/j.cell.2017.12.030.

81. Jana, N.R., Tanaka, M., Wang, Gh., and Nukina, N. (2000). Polyglutamine length-dependent interaction of Hsp40 and Hsp70 family chaperones with truncated N-terminal huntingtin: their role in suppression of aggregation and cellular toxicity. Hum. Mol. Genet. *9*, 2009–2018. https://doi.org/10.1093/hmg/9.13.2009.

82. Park, S.H., Kukushkin, Y., Gupta, R., Chen, T., Konagai, A., Hipp, M.S., Hayer-Hartl, M., and Hartl, F.U. (2013). PolyQ proteins interfere with nuclear degradation of cytosolic proteins by sequestering the Sis1p chaperone. Cell *154*, 134–145. https://doi.org/10.1016/j.cell.2013.06.003.

83. Yang, H., Yue, H.W., He, W.T., Hong, J.Y., Jiang, L.L., and Hu, H.Y. (2018). PolyQ-expanded huntingtin and ataxin-3 sequester ubiquitin adaptors hHR23B and UBQLN2 into aggregates via conjugated ubiquitin. FASEB J. *32*, 2923–2933. https://doi.org/10.1096/fj.201700801RR.

84. Yu, A., Shibata, Y., Shah, B., Calamini, B., Lo, D.C., and Morimoto, R.I. (2014). Protein aggregation can inhibit clathrin-mediated endocytosis by chaperone competition. Proc. Natl. Acad. Sci. USA *111*, E1481–E1490. https://doi.org/10.1073/pnas.1321811111.

85. Midani-Kurçak, J.S., Dinekov, M., Puladi, B., Arzberger, T., and Köhler, C. (2019). Effect of tau-pathology on charged multivesicular body protein 2b (CHMP2B). Brain Res. *1706*, 224–236. https://doi.org/10.1016/j.brainres.2018.11.008.

86. Spencer, B., Kim, C., Gonzalez, T., Bisquertt, A., Patrick, C., Rockenstein, E., Adame, A., Lee, S.J., Desplats, P., and Masliah, E. (2016). alpha-Synuclein interferes with the ESCRT-III complex contributing to the pathogenesis of Lewy body disease. Hum. Mol. Genet. *25*, 1100–1115. https://doi.org/10.1093/hmg/ddv633.

87. Tanikawa, S., Mori, F., Tanji, K., Kakita, A., Takahashi, H., and Wakabayashi, K. (2012). Endosomal sorting related protein CHMP2B is localized in Lewy bodies and glial cytoplasmic inclusions in alpha-synucleinopathy. Neurosci. Lett. *527*, 16–21. https://doi.org/10.1016/j.neulet.2012.08.035.

88. Yamazaki, Y., Takahashi, T., Hiji, M., Kurashige, T., Izumi, Y., Yamawaki, T., and Matsumoto, M. (2010). Immunopositivity for ESCRT-III subunit CHMP2B in granulovacuolar degeneration of neurons in the Alzheimer's disease hippocampus. Neurosci. Lett. *477*, 86–90. https://doi.org/10.1016/j.neulet.2010.04.038.

89. Kurashige, T., Takahashi, T., Yamazaki, Y., Hiji, M., Izumi, Y., Yamawaki, T., and Matsumoto, M. (2013). Localization of CHMP2B-immunoreactivity in the brainstem of Lewy body disease. Neuropathology *33*, 237–245. https://doi.org/10.1111/j.1440-1789.2012.01346.x.

90. Nim, S., O'Hara, D.M., Corbi-Verge, C., Perez-Riba, A., Fujisawa, K., Kapadia, M., Chau, H., Albanese, F., Pawar, G., De Snoo, M.L., et al. (2023). Disrupting the alpha-synuclein-ESCRT interaction with a peptide inhibitor mitigates neurodegeneration in preclinical models of Parkinson's disease. Nat. Commun. *14*, 2150. https://doi.org/10.1038/s41467-023-37464-2.

91. Chou, C.C., Vest, R., Prado, M.A., Wilson-Grady, J., Paulo, J.A., Shibuya, Y., Moran-Losada, P., Lee, T.T., Luo, J., Gygi, S.P., et al. (2025). Proteostasis and lysosomal repair deficits in transdifferentiated neurons of Alzheimer's disease. Nat. Cell Biol. *27*, 619–632. https://doi.org/10.1038/s41556-025-01623-y.

92. Paxinou, E., Chen, Q., Weisse, M., Giasson, B.I., Norris, E.H., Rueter, S.M., Trojanowski, J.Q., Lee, V.M., and Ischiropoulos, H. (2001). Induction of alpha-synuclein aggregation by intracellular nitrative insult. J. Neurosci. *21*, 8053–8061. https://doi.org/10.1523/JNEUROSCI.21-20-08053.2001.

93. Kang, L., Wu, K.P., Vendruscolo, M., and Baum, J. (2011). The A53T mutation is key in defining the differences in the aggregation kinetics of human and mouse alpha-synuclein. J. Am. Chem. Soc. *133*, 13465–13470. https://doi.org/10.1021/ja203979j.

94. Henderson, M.X., Trojanowski, J.Q., and Lee, V.M.Y. (2019). alpha-Synuclein pathology in Parkinson's disease and related alpha-synucleinopathies. Neurosci. Lett. *709*, 134316. https://doi.org/10.1016/j.neulet.2019.134316.

95. Volpicelli-Daley, L.A., Luk, K.C., and Lee, V.M.Y. (2014). Addition of exogenous alpha-synuclein preformed fibrils to primary neuronal cultures to seed recruitment of endogenous alpha-synuclein to Lewy body and Lewy neurite-like aggregates. Nat. Protoc. *9*, 2135–2146. https://doi.org/10.1038/nprot.2014.143.

96. Holmes, B.B., Furman, J.L., Mahan, T.E., Yamasaki, T.R., Mirbaha, H., Eades, W.C., Belaygorod, L., Cairns, N.J., Holtzman, D.M., and Diamond, M.I. (2014). Proteopathic tau seeding predicts tauopathy in vivo. Proc. Natl. Acad. Sci. USA *111*, E4376–E4385. https://doi.org/10.1073/pnas.1411649111.

97. Liu, D., Guo, J.-J., Su, J.-H., Svanbergsson, A., Yuan, L., Haikal, C., Li, W., Gouras, G., and Li, J.-Y. (2021). Differential seeding and propagating efficiency of α-synuclein strains generated in different conditions. Transl. Neurodegener. *10*, 20. https://doi.org/10.1186/s40035-021-00242-5.

98. Nonaka, T., Watanabe, S.T., Iwatsubo, T., and Hasegawa, M. (2010). Seeded aggregation and toxicity of alpha-synuclein and tau: cellular models of neurodegenerative diseases. J. Biol. Chem. *285*, 34885–34898. https://doi.org/10.1074/jbc.M110.148460.

99. Sangwan, S., Sahay, S., Murray, K.A., Morgan, S., Guenther, E.L., Jiang, L., Williams, C.K., Vinters, H.V., Goedert, M., and Eisenberg, D.S. (2020). Inhibition of synucleinopathic seeding by rationally designed inhibitors. Elife *9*, e46775. https://doi.org/10.7554/eLife.46775.

100. See, S.K., Chen, M., Bax, S., Tian, R., Woerman, A., Tse, E., Johnson, I. E., Nowotny, C., Muñoz, E.N., Sengstack, J., et al. (2021). PIKfyve

inhibition blocks endolysosomal escape of α-synuclein fibrils and spread of α-synuclein aggregation. Preprint at bioRxiv. https://doi.org/10.1101/2021.01.21.427704.

101. Zhu, J., Pittman, S., Dhavale, D., French, R., Patterson, J.N., Kaleelurrrahuman, M.S., Sun, Y., Vaquer-Alicea, J., Maggiore, G., Clemen, C.S., et al. (2022). VCP suppresses proteopathic seeding in neurons. Mol. Neurodegener. *17*, 30. https://doi.org/10.1186/s13024-022-00532-0.

102. Fujiwara, H., Hasegawa, M., Dohmae, N., Kawashima, A., Masliah, E., Goldberg, M.S., Shen, J., Takio, K., and Iwatsubo, T. (2002). alpha-Synuclein is phosphorylated in synucleinopathy lesions. Nat. Cell Biol. *4*, 160–164. https://doi.org/10.1038/ncb748.

103. Anderson, J.P., Walker, D.E., Goldstein, J.M., de Laat, R., Banducci, K., Caccavello, R.J., Barbour, R., Huang, J., Kling, K., Lee, M., et al. (2006). Phosphorylation of Ser-129 is the dominant pathological modification of alpha-synuclein in familial and sporadic Lewy body disease. J. Biol. Chem. *281*, 29739–29752. https://doi.org/10.1074/jbc.M600933200.

104. Hasegawa, M., Fujiwara, H., Nonaka, T., Wakabayashi, K., Takahashi, H., Lee, V.M.Y., Trojanowski, J.Q., Mann, D., and Iwatsubo, T. (2002). Phosphorylated alpha-synuclein is ubiquitinated in alpha-synucleinopathy lesions. J. Biol. Chem. *277*, 49071–49076. https://doi.org/10.1074/jbc.M208046200.

105. Kuusisto, E., Salminen, A., and Alafuzoff, I. (2001). Ubiquitin-binding protein p62 is present in neuronal and glial inclusions in human tauopathies and synucleinopathies. NeuroReport *12*, 2085–2090. https://doi.org/10.1097/00001756-200107200-00009.

106. Chang, D., Nalls, M.A., Hallgrimsdottir, I.B., Hunkapiller, J., van der Brug, M., Cai, F., International Parkinson's Disease Genomics Consortium; 23andMe Research Team, Kerchner, G.A., Ayalon, G., et al. (2017). A meta-analysis of genome-wide association studies identifies 17 new Parkinson's disease risk loci. Nat Genet *49*, 1511–1516. https://doi.org/10.1038/ng.3955.

107. Stokholm, J., Teasdale, T.W., Johannsen, P., Nielsen, J.E., Nielsen, T.T., Isaacs, A., Brown, J.M., and Gade, A.; Frontotemporal dementia Research in Jutland Association (FReJA) consortium (2013). Cognitive impairment in the preclinical stage of dementia in FTD-3 CHMP2B mutation carriers: a longitudinal prospective study. J. Neurol. Neurosurg. Psychiatry *84*, 170–176. https://doi.org/10.1136/jnnp-2012-303813.

108. Babst, M., Katzmann, D.J., Estepa-Sabal, E.J., Meerloo, T., and Emr, S.D. (2002). Escrt-III: an endosome-associated heterooligomeric protein complex required for mvb sorting. Dev. Cell *3*, 271–282. https://doi.org/10.1016/s1534-5807(02)00220-4.

109. Babst, M., Wendland, B., Estepa, E.J., and Emr, S.D. (1998). The Vps4p AAA ATPase regulates membrane association of a Vps protein complex required for normal endosome function. EMBO J. *17*, 2982–2993. https://doi.org/10.1093/emboj/17.11.2982.

110. Bodner, C.R., Dobson, C.M., and Bax, A. (2009). Multiple tight phospholipid-binding modes of alpha-synuclein revealed by solution NMR spectroscopy. J. Mol. Biol. *390*, 775–790. https://doi.org/10.1016/j.jmb.2009.05.066.

111. Davidson, W.S., Jonas, A., Clayton, D.F., and George, J.M. (1998). Stabilization of alpha-synuclein secondary structure upon binding to synthetic membranes. J. Biol. Chem. *273*, 9443–9449. https://doi.org/10.1074/jbc.273.16.9443.

112. Jensen, P.H., Nielsen, M.S., Jakes, R., Dotti, C.G., and Goedert, M. (1998). Binding of alpha-synuclein to brain vesicles is abolished by familial Parkinson's disease mutation. J. Biol. Chem. *273*, 26292–26294. https://doi.org/10.1074/jbc.273.41.26292.

113. Maroteaux, L., and Scheller, R.H. (1991). The rat brain synucleins; family of proteins transiently associated with neuronal membrane. Brain Res. Mol. Brain Res. *11*, 335–343. https://doi.org/10.1016/0169-328x(91)90043-w.

114. Muzioł, T., Pineda-Molina, E., Ravelli, R.B., Zamborlini, A., Usami, Y., Göttlinger, H., and Weissenhorn, W. (2006). Structural basis for budding by the ESCRT-III factor CHMP3. Dev. Cell *10*, 821–830. https://doi.org/10.1016/j.devcel.2006.03.013.

115. Saksena, S., Wahlman, J., Teis, D., Johnson, A.E., and Emr, S.D. (2009). Functional reconstitution of ESCRT-III assembly and disassembly. Cell *136*, 97–109. https://doi.org/10.1016/j.cell.2008.11.013.

116. Teis, D., Saksena, S., and Emr, S.D. (2008). Ordered assembly of the ESCRT-III complex on endosomes is required to sequester cargo during MVB formation. Dev. Cell *15*, 578–589. https://doi.org/10.1016/j.devcel.2008.08.013.

117. Whitley, P., Reaves, B.J., Hashimoto, M., Riley, A.M., Potter, B.V.L., and Holman, G.D. (2003). Identification of mammalian Vps24p as an effector of phosphatidylinositol 3,5-bisphosphate-dependent endosome compartmentalization. J. Biol. Chem. *278*, 38786–38795. https://doi.org/10.1074/jbc.M306864200.

118. Moser von Filseck, J., Barberi, L., Talledge, N., Johnson, I.E., Frost, A., Lenz, M., and Roux, A. (2020). Anisotropic ESCRT-III architecture governs helical membrane tube formation. Nat. Commun. *11*, 1516. https://doi.org/10.1038/s41467-020-15327-4.

119. Forno, L.S., DeLanney, L.E., Irwin, I., and Langston, J.W. (1996). Electron microscopy of Lewy bodies in the amygdala-parahippocampal region. Comparison with inclusion bodies in the MPTP-treated squirrel monkey. Adv. Neurol. *69*, 217–228.

120. Forno, L.S., and Norville, R.L. (1976). Ultrastructure of Lewy bodies in the stellate ganglion. Acta Neuropathol. *34*, 183–197. https://doi.org/10.1007/BF00688674.

121. Hayashida, K., Oyanagi, S., Mizutani, Y., and Yokochi, M. (1993). An early cytoplasmic change before Lewy body maturation: an ultrastructural study of the substantia nigra from an autopsy case of juvenile parkinsonism. Acta Neuropathol. *85*, 445–448. https://doi.org/10.1007/BF00334457.

122. Mahul-Mellier, A.L., Burtscher, J., Maharjan, N., Weerens, L., Croisier, M., Kuttler, F., Leleu, M., Knott, G.W., and Lashuel, H.A. (2020). The process of Lewy body formation, rather than simply alpha-synuclein fibrillization, is one of the major drivers of neurodegeneration. Proc. Natl. Acad. Sci. USA *117*, 4971–4982. https://doi.org/10.1073/pnas.1913904117.

123. Chassefeyre, R., Martínez-Hernández, J., Bertaso, F., Bouquier, N., Blot, B., Laporte, M., Fraboulet, S., Couté, Y., Devoy, A., Isaacs, A.M., et al. (2015). Regulation of postsynaptic function by the dementia-related ESCRT-III subunit CHMP2B. J. Neurosci. *35*, 3155–3173. https://doi.org/10.1523/JNEUROSCI.0586-14.2015.

124. Yorikawa, C., Shibata, H., Waguri, S., Hatta, K., Horii, M., Katoh, K., Kobayashi, T., Uchiyama, Y., and Maki, M. (2005). Human CHMP6, a myristoylated ESCRT-III protein, interacts directly with an ESCRT-II component EAP20 and regulates endosomal cargo sorting. Biochem. J. *387*, 17–26. https://doi.org/10.1042/BJ20041227.

125. Scott, A., Gaspar, J., Stuchell-Brereton, M.D., Alam, S.L., Skalicky, J.J., and Sundquist, W.I. (2005). Structure and ESCRT-III protein interactions of the MIT domain of human VPS4A. Proc. Natl. Acad. Sci. USA *102*, 13813–13818. https://doi.org/10.1073/pnas.0502165102.

126. Shim, S., Kimpler, L.A., and Hanson, P.I. (2007). Structure/function analysis of four core ESCRT-III proteins reveals common regulatory role for extreme C-terminal domain. Traffic *8*, 1068–1079. https://doi.org/10.1111/j.1600-0854.2007.00584.x.

127. Zamborlini, A., Usami, Y., Radoshitzky, S.R., Popova, E., Palu, G., and Göttlinger, H. (2006). Release of autoinhibition converts ESCRT-III components into potent inhibitors of HIV-1 budding. Proc. Natl. Acad. Sci. USA *103*, 19140–19145. https://doi.org/10.1073/pnas.0603788103.

128. Lee, J.A., Beigneux, A., Ahmad, S.T., Young, S.G., and Gao, F.B. (2007). ESCRT-III dysfunction causes autophagosome accumulation and neurodegeneration. Curr. Biol. *17*, 1561–1567. https://doi.org/10.1016/j.cub.2007.07.029.

129. Katayama, H., Yamamoto, A., Mizushima, N., Yoshimori, T., and Miyawaki, A. (2008). GFP-like proteins stably accumulate in lysosomes. Cell Struct. Funct. *33*, 1–12. https://doi.org/10.1247/csf.07011.

130. Abu-Remaileh, M., Wyant, G.A., Kim, C., Laqtom, N.N., Abbasi, M., Chan, S.H., Freinkman, E., and Sabatini, D.M. (2017). Lysosomal metabolomics reveals V-ATPase- and mTOR-dependent regulation of amino acid efflux from lysosomes. Science *358*, 807–813. https://doi.org/10.1126/science.aan6298.

131. Giaever, G., Shoemaker, D.D., Jones, T.W., Liang, H., Winzeler, E.A., Astromoff, A., and Davis, R.W. (1999). Genomic profiling of drug sensitivities via induced haploinsufficiency. Nat. Genet. *21*, 278–283. https://doi.org/10.1038/6791.

132. Hartwell, L.H., Szankasi, P., Roberts, C.J., Murray, A.W., and Friend, S.H. (1997). Integrating genetic approaches into the discovery of anticancer drugs. Science *278*, 1064–1068. https://doi.org/10.1126/science.278.5340.1064.

133. Barondes, S.H., Castronovo, V., Cooper, D.N., Cummings, R.D., Drickamer, K., Feizi, T., Gitt, M.A., Hirabayashi, J., Hughes, C., Kasai, K., et al. (1994). Galectins: a family of animal beta-galactoside-binding lectins. Cell *76*, 597–598. https://doi.org/10.1016/0092-8674(94)90498-7.

134. Hoyer, M.J., Swarup, S., and Harper, J.W. (2022). Mechanisms controlling selective elimination of damaged lysosomes. Curr. Opin. Physiol. *29*, 100590. https://doi.org/10.1016/j.cophys.2022.100590.

135. Papadopoulos, C., and Meyer, H. (2017). Detection and clearance of damaged lysosomes by the endo-lysosomal damage response and lysophagy. Curr. Biol. *27*, R1330–R1341. https://doi.org/10.1016/j.cub.2017.11.012.

136. Thurston, T.L.M., Wandel, M.P., von Muhlinen, N., Foeglein, A., and Randow, F. (2012). Galectin 8 targets damaged vesicles for autophagy to defend cells against bacterial invasion. Nature *482*, 414–418. https://doi.org/10.1038/nature10744.

137. Aits, S., Kricker, J., Liu, B., Ellegaard, A.M., Hämälistö, S., Tvingsholm, S., Corcelle-Termeau, E., Høgh, S., Farkas, T., Holm Jonassen, A., et al. (2015). Sensitive detection of lysosomal membrane permeabilization by lysosomal galectin puncta assay. Autophagy *11*, 1408–1424. https://doi.org/10.1080/15548627.2015.1063871.

138. Zhang, Y., Pak, C., Han, Y., Ahlenius, H., Zhang, Z., Chanda, S., Marro, S., Patzke, C., Acuna, C., Covy, J., et al. (2013). Rapid single-step induction of functional neurons from human pluripotent stem cells. Neuron *78*, 785–798. https://doi.org/10.1016/j.neuron.2013.05.029.

139. Zhou, S., Feng, S., Brown, D., and Huang, B. (2020). Improved yellow-green split fluorescent proteins for protein labeling and signal amplification. PLoS One *15*, e0242592. https://doi.org/10.1371/journal.pone.0242592.

140. Gaspar, R., Meisl, G., Buell, A.K., Young, L., Kaminski, C.F., Knowles, T.P.J., Sparr, E., and Linse, S. (2017). Secondary nucleation of monomers on fibril surface dominates alpha-synuclein aggregation and provides autocatalytic amyloid amplification. Q. Rev. Biophys. *50*, e6. https://doi.org/10.1017/S0033583516000172.

141. Törnquist, M., Michaels, T.C.T., Sanagavarapu, K., Yang, X., Meisl, G., Cohen, S.I.A., Knowles, T.P.J., and Linse, S. (2018). Secondary nucleation in amyloid formation. Chem. Commun. (Camb.) *54*, 8667–8684. https://doi.org/10.1039/c8cc02204f.

142. Cohen, S.I.A., Linse, S., Luheshi, L.M., Hellstrand, E., White, D.A., Rajah, L., Otzen, D.E., Vendruscolo, M., Dobson, C.M., and Knowles, T.P.J. (2013). Proliferation of amyloid-β42 aggregates occurs through a secondary nucleation mechanism. Proc. Natl. Acad. Sci. USA *110*, 9758–9763. https://doi.org/10.1073/pnas.1218402110.

143. Collins, S.R., Douglass, A., Vale, R.D., and Weissman, J.S. (2004). Mechanism of prion propagation: amyloid growth occurs by monomer addition. PLoS Biol. *2*, e321. https://doi.org/10.1371/journal.pbio.0020321.

144. Elenbaas, B.O.W., Kremsreiter, S.M., Khemtemourian, L., Killian, J.A., and Sinnige, T. (2023). Fibril elongation by human islet amyloid polypeptide is the main event linking aggregation to membrane damage. BBA Adv. *3*, 100083. https://doi.org/10.1016/j.bbadva.2023.100083.

145. Lashuel, H.A., and Lansbury, P.T., Jr. (2006). Are amyloid diseases caused by protein aggregates that mimic bacterial pore-forming toxins? Q. Rev. Biophys. *39*, 167–201. https://doi.org/10.1017/S0033583506004422.

146. Maraganore, D.M. (2011). Rationale for therapeutic silencing of alpha-synuclein in Parkinson's disease. J. Mov. Disord. *4*, 1–7. https://doi.org/10.14802/jmd.11001.

147. McMillan, B.J., Tibbe, C., Jeon, H., Drabek, A.A., Klein, T., and Blacklow, S.C. (2016). Electrostatic interactions between elongated monomers drive filamentation of Drosophila Shrub, a metazoan ESCRT-III protein. Cell Rep. *16*, 1211–1217. https://doi.org/10.1016/j.celrep.2016.06.093.

148. Prus, G., Satpathy, S., Weinert, B.T., Narita, T., and Choudhary, C. (2024). Global, site-resolved analysis of ubiquitylation occupancy and turnover rate reveals systems properties. Cell *187*, 2875–2892.e21. https://doi.org/10.1016/j.cell.2024.03.024.

149. Brooker, S.M., Naylor, G.E., and Krainc, D. (2024). Cell biology of Parkinson's disease: mechanisms of synaptic, lysosomal, and mitochondrial dysfunction. Curr. Opin. Neurobiol. *85*, 102841. https://doi.org/10.1016/j.conb.2024.102841.

150. Dehay, B., Martinez-Vicente, M., Caldwell, G.A., Caldwell, K.A., Yue, Z., Cookson, M.R., Klein, C., Vila, M., and Bezard, E. (2013). Lysosomal impairment in Parkinson's disease. Mov. Disord. *28*, 725–732. https://doi.org/10.1002/mds.25462.

151. Klein, A.D., and Mazzulli, J.R. (2018). Is Parkinson's disease a lysosomal disorder? Brain *141*, 2255–2262. https://doi.org/10.1093/brain/awy147.

152. Tofaris, G.K. (2012). Lysosome-dependent pathways as a unifying theme in Parkinson's disease. Mov. Disord. *27*, 1364–1369. https://doi.org/10.1002/mds.25136.

153. Duda, J.E., Giasson, B.I., Mabon, M.E., Miller, D.C., Golbe, L.I., Lee, V.M.Y., and Trojanowski, J.Q. (2002). Concurrence of alpha-synuclein and tau brain pathology in the Contursi kindred. Acta Neuropathol. *104*, 7–11. https://doi.org/10.1007/s00401-002-0563-3.

154. Ishizawa, T., Mattila, P., Davies, P., Wang, D., and Dickson, D.W. (2003). Colocalization of tau and alpha-synuclein epitopes in Lewy bodies. J. Neuropathol. Exp. Neurol. *62*, 389–397. https://doi.org/10.1093/jnen/62.4.389.

155. Howlett, D.R., Whitfield, D., Johnson, M., Attems, J., O'Brien, J.T., Aarsland, D., Lai, M.K.P., Lee, J.H., Chen, C., Ballard, C., et al. (2015). Regional multiple pathology scores are associated with cognitive decline in Lewy body dementias. Brain Pathol. *25*, 401–408. https://doi.org/10.1111/bpa.12182.

156. Irwin, D.J., Lee, V.M.Y., and Trojanowski, J.Q. (2013). Parkinson's disease dementia: convergence of alpha-synuclein, tau and amyloid-beta pathologies. Nat. Rev. Neurosci. *14*, 626–636. https://doi.org/10.1038/nrn3549.

157. Ran, F.A., Hsu, P.D., Wright, J., Agarwala, V., Scott, D.A., and Zhang, F. (2013). Genome engineering using the CRISPR-Cas9 system. Nat. Protoc. *8*, 2281–2308. https://doi.org/10.1038/nprot.2013.143.

158. Rospigliosi, C.C., McClendon, S., Schmid, A.W., Ramlall, T.F., Barré, P., Lashuel, H.A., and Eliezer, D. (2009). E46K Parkinson's-linked mutation enhances C-terminal-to-N-terminal contacts in alpha-synuclein. J. Mol. Biol. *388*, 1022–1032. https://doi.org/10.1016/j.jmb.2009.03.065.

159. Linse, S. (2020). Expression and purification of intrinsically disordered Abeta peptide and setup of reproducible aggregation kinetics experiment. Methods Mol. Biol. *2141*, 731–754. https://doi.org/10.1007/978-1-0716-0524-0_38.

160. Kraus, F., Goodall, E.A., Smith, I.R., Jiang, Y., Paoli, J.C., Adolf, F., Zhang, J., Paulo, J.A., Schulman, B.A., and Harper, J.W. (2023). PARK15/FBXO7 is dispensable for PINK1/Parkin mitophagy in

iNeurons and HeLa cell systems. EMBO Rep. *24*, e56399. https://doi.org/10.15252/embr.202256399.

161. Sanders, D.W., Kaufman, S.K., DeVos, S.L., Sharma, A.M., Mirbaha, H., Li, A., Barker, S.J., Foley, A.C., Thorpe, J.R., Serpell, L.C., et al. (2014). Distinct tau prion strains propagate in cells and mice and define different tauopathies. Neuron *82*, 1271–1288. https://doi.org/10.1016/j.neuron.2014.04.047.

162. Yuste-Checa, P., Trinkaus, V.A., Riera-Tur, I., Imamoglu, R., Schaller, T. F., Wang, H., Dudanova, I., Hipp, M.S., Bracher, A., and Hartl, F.U. (2021). The extracellular chaperone Clusterin enhances Tau aggregate seeding in a cellular model. Nat. Commun. *12*, 4863. https://doi.org/10.1038/s41467-021-25060-1.

163. Schindelin, J., Arganda-Carreras, I., Frise, E., Kaynig, V., Longair, M., Pietzsch, T., Preibisch, S., Rueden, C., Saalfeld, S., Schmid, B., et al. (2012). Fiji: an open-source platform for biological-image analysis. Nat. Methods *9*, 676–682. https://doi.org/10.1038/nmeth.2019.

164. Madeira, F., Madhusoodanan, N., Lee, J., Eusebi, A., Niewielska, A., Tivey, A.R.N., Lopez, R., and Butcher, S. (2024). The EMBL-EBI Job Dispatcher sequence analysis tools framework in 2024. Nucleic Acids Res. *52*, W521–W525. https://doi.org/10.1093/nar/gkae241.

165. Saha, I., Yuste-Checa, P., Da Silva Padilha, M., Guo, Q., Körner, R., Holthusen, H., Trinkaus, V.A., Dudanova, I., Fernández-Busnadiego, R., Baumeister, W., et al. (2023). The AAA+ chaperone VCP disaggregates Tau fibrils and generates aggregate seeds in a cellular system. Nat. Commun. *14*, 560. https://doi.org/10.1038/s41467-023-36058-2.

166. Hoyer, M.J., Capitanio, C., Smith, I.R., Paoli, J.C., Bieber, A., Jiang, Y., Paulo, J.A., Gonzalez-Lozano, M.A., Baumeister, W., Wilfling, F., et al. (2024). Combinatorial selective ER-phagy remodels the ER during neurogenesis. Nat. Cell Biol. *26*, 378–392. https://doi.org/10.1038/s41556-024-01356-4.

167. Giasson, B.I., Murray, I.V., Trojanowski, J.Q., and Lee, V.M. (2001). A hydrophobic stretch of 12 amino acid residues in the middle of alpha-synuclein is essential for filament assembly. J. Biol. Chem. *276*, 2380–2386. https://doi.org/10.1074/jbc.M008919200.

168. Walsh, D.M., Thulin, E., Minogue, A.M., Gustavsson, N., Pang, E., Teplow, D.B., and Linse, S. (2009). A facile method for expression and purification of the Alzheimer's disease-associated amyloid beta-peptide. FEBS Journal *276*, 1266–1281. https://doi.org/10.1111/j.1742-4658.2008.06862.x.

169. Ordureau, A., Paulo, J.A., Zhang, W., Ahfeldt, T., Zhang, J., Cohn, E.F., Hou, Z., Heo, J.M., Rubin, L.L., Sidhu, S.S., et al. (2018). Dynamics of PARKIN-dependent mitochondrial ubiquitylation in induced neurons and model systems revealed by digital snapshot proteomics. Mol. Cell *70*, 211–227.e8. https://doi.org/10.1016/j.molcel.2018.03.012.

170. Delic, V., Chandra, S., Abdelmotilib, H., Maltbie, T., Wang, S., Kem, D., Scott, H.J., Underwood, R.N., Liu, Z., Volpicelli-Daley, L.A., et al. (2018). Sensitivity and specificity of phospho-Ser129 alpha-synuclein monoclonal antibodies. J. Comp. Neurol. *526*, 1978–1990. https://doi.org/10.1002/cne.24468.

171. Feng, S., Sekine, S., Pessino, V., Li, H., Leonetti, M.D., and Huang, B. (2017). Improved split fluorescent proteins for endogenous protein labeling. Nat. Commun. *8*, 370. https://doi.org/10.1038/s41467-017-00494-8.

172. Mahul-Mellier, A.-L., Altay, F., Burtscher, J., Maharjan, N., Ait Bouziad, N., Chiki, A., Vingill, S., Wade-Martins, R., Holton, J., Strand, C., et al. (2018). The making of a Lewy body: the role of α-synuclein post-fibrillization modifications in regulating the formation and the maturation of pathological inclusions. Preprint at bioRxiv. https://doi.org/10.1101/500058.

STAR★METHODS

KEY RESOURCES TABLE

REAGENT or RESOURCE	SOURCE	IDENTIFIER
Antibodies		
CHMP2A	Proteintech	Cat#10477-1-AP; RRID: AB_2079470
CHMP2B	Abcam	Cat#ab33174; RRID: AB_2079471
CHMP2B	Proteintech	Cat#12527-1-AP; RRID: AB_10603358
CHMP3	Santa Cruz	Cat#sc-166361; RRID: AB_2217111
CHMP4B	Proteintech	Cat#13683-1-AP; RRID: AB_2877971
CHMP6	Proteintech	Cat#16278-1-AP; RRID: AB_2079498
α-synuclein (MJFR1)	Abcam	Cat#ab138501; RRID: AB_2537217
α-synuclein (LB509)	Abcam	Cat#ab27766; RRID: AB_727020
α-synuclein phosphoS129 (81A)	Abcam	Cat#ab184674; RRID: AB_2819037
α-synuclein phosphoS129 (EP1536Y)	Abcam	Cat#ab51253; RRID: AB_869973
MAP2	Merck Millipore	Cat#AB5543; RRID: AB_571049
HA	Santa Cruz	Cat#sc-7392; RRID: AB_627809
β-Amyloid	Biolegend	Cat#803001; RRID: AB_2564652
p62	Abcam	Cat#ab56416; RRID: AB_945626
K48 ubiquitin	Merck Millipore	Cat#05-1307; RRID: AB_11213655
EEA1	Abcam	Cat#ab2900; RRID: AB_2262056
LAMP2	Santa Cruz	Cat#sc-18822; RRID: AB_626858
LAMP1	Developmental Studies Hybridoma Bank (DSHB)	Cat#H4A3; RRID: AB_2296838
Ubiquitin	Santa Cruz	Cat#sc-8017; RRID: AB_628423
GFP	Proteintech	Cat#3h9-150; RRID: AB_10773374
β-actin	Abcam	Cat#ab6276; RRID: AB_2223210
GAPDH	Merck Millipore	Cat#MAB374; RRID: AB_2107445
HSP60	Abcam	Cat#ab59458; RRID: AB_942025
Calreticulin	Cell Signaling Technologies	Cat#12238S; RRID: AB_2688013
Calnexin	Santa Cruz	Cat#sc-46669; RRID: AB_626784
α-tubulin	Sigma Aldrich	Cat#T6199; RRID: AB_477583
Anti-rabbit IgG (H+L), F(ab′)2 Fragment Alexa Fluor 488	Cell Signaling Technologies	Cat#4412S; RRID: AB_1904025
Goat anti-Mouse IgG (H+L) Cross-Adsorbed Secondary Antibody, Alexa Fluor 488	Thermo Fisher Scientific	Cat#A-11001; RRID: AB_2534069
F(ab′)2-Goat anti-Mouse IgG (H+L) Cross-Adsorbed Secondary Antibody, Alexa Fluor 568	Thermo Fisher Scientific	Cat#A-11019; RRID: AB_143162
Goat anti-Chicken IgY (H+L) Secondary Antibody, Alexa Fluor 647	Thermo Fisher Scientific	Cat#A-21449; RRID: AB_2535866
Goat anti-Mouse IgG (H+L) Highly Cross-Adsorbed Secondary Antibody, Alexa Fluor Plus 647	Thermo Fisher Scientific	Cat#A-32728; RRID: AB_2633277
Goat anti-Rabbit IgG (H+L) Highly Cross-Adsorbed Secondary Antibody, Alexa Fluor Plus 647	Thermo Fisher Scientific	Cat#A-32733; RRID: AB_2633282
Goat anti-Rabbit IgG (H+L) Secondary Antibody, Alexa Fluor 405	Thermo Fisher Scientific	Cat#A-31556; RRID: AB_221605

(*Continued on next page*)

Continued

REAGENT or RESOURCE	SOURCE	IDENTIFIER
anti-Mouse HRP	Sigma Aldrich	Cat#A4416; RRID: AB_258167
anti-Rabbit HRP	Sigma Aldrich	Cat#A9169; RRID: AB_258434
anti-Rat HRP	Sigma Aldrich	Cat#A9037; RRID: AB_258429
Veriblot	Abcam	Cat#ab131366; RRID: AB_2892718
Rabbit IgG, polyclonal - Isotype Control	Abcam	Cat#ab37415; RRID:AB_2631996
OCT4 (C30A3) rabbit mAb	Cell Signaling Technologies	Cat#2840S; RRID:AB_2799505
Synapsin I	Abcam	Cat#ab18814; RRID:AB_444679
HSP90 antibody (4F10)	Santa Cruz	Cat#sc-69703; RRID:AB_2121191
Rabbit anti-FLAG	Sigma-Aldrich	Cat#F7425; RRID:AB_439687
IRDye 680RD goat anti-mouse IgG	Licor	Cat#926-68070; RRID:AB_2651128
IRDye® 800CW Goat anti-Rabbit IgG	Licor	Cat#92632211; RRID:AB_621843
Bacterial and virus strains		
BL21(DE3) E Coli	Hartl lab stock	N/A
Rosetta (DE3)pLysS E Coli cells	Merck	Cat#70956
pTetOFF a-syn A53T	This study	pCS1; RRID:Addgene_215372
pEF1a mNeonGreen-3K-B1-10-IRES-mKate2-2A-PuroR	This study	pCS7; RRID:Addgene_ 215377
pLJC5-Tmem192-3xHA	Abu-Remaileh et al.[130]	RRID:Addgene_102930
pLKO.1 mouse NT	This study	pCS34; RRID:Addgene_242421
pLKO.1 mouse CHMP2B	This study	pCS35; RRID:Addgene_242422
phSyn2 sfGFP-RNF152	This study	pCS29; RRID:Addgene_215374
Chemicals, peptides, and recombinant proteins		
cOmplete EDTA-free Protease Inhibitor	Roche	Cat#5056489001
cOmplete Mini EDTA-free Protease Inhibitor Cocktail	Roche	Cat#4693159001
Alexa Fluor 647 NHS Ester	Thermo Fisher Scientific	Cat#A20006
LLOMe	Santa Cruz	Cat#sc-285992B
Leupeptin	Sigma Aldrich	Cat#11017101001
MLN7243	Selleckchem	Cat#S8341
Bafilomycin A1	Invivogen	Cat#tlrl-baf1
Doxycycline	Clontech	Cat#631311
Y-27632	Biozol	Cat#S1049
PR-619	Sigma Aldrich	Cat#662141-25MG
Bortezomib	LC Laboratories	Cat#B-1408
N-ethylmaleimide	Sigma Aldrich	Cat#E3876-25G
Blasticidin S	Thermo Fisher Scientific	Cat#A1113903
G418	Thermo Fisher Scientific	Cat#10131035
Puromycin	Thermo Fisher Scientific	Cat#A1113803
Terrific Broth	Sigma Aldrich	Cat#T0918
Lipofectamine 3000	Thermo Fisher Scientific	Cat#L3000008
Fugene 6	Promega	Cat#E2692
X-tremeGENE HP DNA Transfection Reagent	Sigma Aldrich	Cat#6366244001
B-27 Plus	Thermo Fisher Scientific	Cat#A3582801
Polybrene	Sigma Aldrich	Cat#TR-1003-G
Lenti-X concentrator	Takara	Cat#631231
poly-D-lysine	Sigma Adrich	Cat#A-003-E
Laminin	Thermo Fisher Scientific	Cat#23017015

(*Continued on next page*)

Continued

REAGENT or RESOURCE	SOURCE	IDENTIFIER
Laminin	Bio-techne	Cat#3446-005-01
Matrigel	Corning	Cat#354277
Accutase	StemCell	Cat#7920
N2	Thermo Fisher Scientific	Cat#17502048
NT3	Peprotech	Cat#AF-450-03-10
BDNF	Peprotech	Cat#450-02
MEM NEAA	Thermo Fisher Scientific	Cat#11140050
GlutaMAX	Thermo Fisher Scientific	Cat#35050061
1% L-Glutamine	Thermo Fisher Scientific	Cat#25030081
mTeSR Plus	Stem Cell Technologies	Cat#100-0276
Neurobasal	Thermo Fisher Scientific	Cat#21103049
StemFlex Medium	Gibco	Cat#A3349401
UltraPure 0.5M EDTA, pH 8.0	Thermo Fisher Scientific	Cat#15575020
ReLeSR	Stem Cell Technologies	Cat#5873
DMEM/F12	Thermo Fisher Scientific	Cat#11995073
FBS (fetal bovine serum)	Thermo Fisher Scientific	Cat#1027010
Penicillin-Streptomycin	Thermo Fisher Scientific	Cat#15140163
TrypLE Express	Thermo Fisher Scientific	Cat#12605036
NucBlue	Thermo Fisher Scientific	Cat#R37606
Paraformaldehyde (PFA)	Thermo Fisher Scientific	Cat#28908
Dako Fluorescence Mounting Medium	Agilent	Cat#S3023
4X NuPAGE LDS Sample Buffer	Thermo Fisher Scientific	Cat#NP0007
Immobilon Forte Western HRP Substrate	Merck Millipore	Cat#WBLUF0500
Immobilon Classico Western HRP Substrate	Merck Millipore	Cat#WBLUC0500
Restore Western Blot Stripping Buffer	Thermo Fisher Scientific	Cat#21059
Protein G Dynabeads	Invitrogen	Cat#10007D
Ubiquitin pan-selector resin	NanoTag Biotechnologies	Cat#N2510
anti-HA magnetic beads	Thermo Fisher Scientific	Cat#88836
Pierce Magnetic Streptavidin Beads	Thermo Fisher Scientific	Cat#88816
Biotinylated CHMP2B 55-96 α2 peptide	Max Planck Institute of Biochemistry Bioorganic Chemistry & Biophysics Core Facility; Sequence: Biotin-GSKEACKVLAK QLVHLRKQKTRTFAVSSKVTSMS TQTKVMNSQM-NH_2	N/A
DNAse I	Thermo Fisher Scientific	Cat#EN0521
Cas9-NLS	QB3 MacroLab; UC Berkeley	N/A
Cpf1 (recombinant protein)	in-house	N/A
α-Synuclein	in-house	N/A
CHMP2B	in-house	This paper
Benzonase	Max Planck Institute of Biochemistry Core Facility	N/A
Benzonase	Merck	Cat#71205-M
His-SenP2 protease	Max Planck Institute of Biochemistry Core Facility	N/A
DMSO	Thermo Fisher Scientific	Cat#D12345
DEAE sepharose	GE	Cat#17-0709-01
Ni-NTA Resin	Thermo Fisher Scientific	Cat#88221
Lenti-X concentrator	Takara	Cat#631231

(*Continued on next page*)

Continued

REAGENT or RESOURCE	SOURCE	IDENTIFIER
PageRuler Prestained Protein Ladder	Thermo Fisher Scientific	Cat#26617
RIPA Buffer	Thermo Fisher Scientific	Cat#89900
Li-Cor Intercept (TBS) Blocking Buffer	Licor	Cat#927-60001
10X Tris/Gycine/SDS Buffer	Bio-Rad	Cat#1610772
10X Tris/Glycine Buffer	Bio-Rad	Cat#16107715
Heparin sodium salt from porcine intestinal mucosa	Merck	Cat#H3393
Phalloidin-iFluor 647 Reagent	Abcam	Cat#ab176759
Zombie NIR™ Fixable Viability Kit	Biolegend	Cat#423106
DPBS with calcium and magnesium	Thermo Fisher Scientific	Cat#14040174
Saponin	Sigma-Aldrich	Cat#47036
Lysozyme	Sigma-Aldrich	Cat#L6876
GFP-Trap® Magnetic Agarose	Proteintech	Cat#gtma-20;RRID:AB_2631358
DYKDDDDK Fab-Trap® Agarose	Proteintech	Cat#ffaa-20;RRID:AB_2894836
Usp2	Max Planck Institute of Biochemistry Core Facility	N/A
TauRD (C291A/P301L/C322A/V337M)	in-house	N/A
Critical commercial assays		
GeneArt Precision gRNA Synthesis Kit	Thermo Fisher Scientific	Cat#A29377
Pierce Rapid Gold BCA Protein Assay Kit	Thermo Fisher Scientific	Cat#A53225
Deposited data		
Flow Cytometry Data	This study	Zenodo: https://doi.org/10.5281/zenodo.14506782
Microscopy Data	This study	Zenodo: https://doi.org/10.5281/zenodo.14506782
Immunoblot Data	This study	Zenodo: https://doi.org/10.5281/zenodo.14506782
Tabular Data	This study	Zenodo: https://doi.org/10.5281/zenodo.14506782
UniProt (accessed 2024-07-30)	Uniprot	RRID:SCR_002380; https://www.uniprot.org
Experimental models: Cell lines		
HEK293T	ATCC	RRID: CVCL_0063
HEK293T a-syn-A53T-mRuby3 a-syn-A53T-mClover3	This study	RRID: CVCL_D4BV
HEK293T TetOff-a-syn-A53T	This study	RRID: CVCL_D4BW
HEK293T TetOff-a-syn-A53T mRuby3-Galectin-3 mClover3-Galectin-3	This study	RRID: CVCL_D4BX
HEK293T TetOff-a-syn-A53T EGFP-RNF152-IRES-mScarlet-I	This study	RRID: CVCL_D4BY
HEK293T TetOff-a-syn-A53T mNeonGreen-3K-1-10-IRES-mKate2	This study	RRID: CVCL_D4BZ
HEK293T TetOff-a-syn-A53T EGFP-RNF152-IRES-mScarlet-I TMEM192-3xHA	This study	RRID: CVCL_E4JW
Lenti-X 293T cells	Takara	Cat#632180; No RRID
KOLF2.1J AAVS1-TREG3-NGN2	Hoyer et al.[134]	RRID: CVCL_D1J6
KOLF2.1J AAVS1-TRE3G-NGN2 CHMP2B-/- cells	This study	RRID: CVCL_E3Y0
KOLF2.1J AAVS1-TRE3G-NGN2 CHMP2B Q165X/+ cells	This study	RRID: CVCL_E3Y1

(*Continued on next page*)

Continued

REAGENT or RESOURCE	SOURCE	IDENTIFIER
KOLF2.1J AAVS1-TRE3G-NGN2 CHMP2B I29V/I29V cells	This study	RRID: CVCL_E3Y2
HEK293T TetOff-a-syn-A53T TauRD (P301L/V337M)-EYFP	This study	RRID: CVCL_F0F7
Experimental models: Organisms/strains		
CD-1 wild-type mouse	MPIB Animal House	RRID:MGI:5649524
Oligonucleotides		
Negative Control siPOOL	siTOOLs Biotech	Cat#si-C002
CHMP2A siPOOL	siTOOLs Biotech	Cat#si-G020-27243
ON-TARGETplus Non-targeting Pool siRNA	Horizon Discovery	Cat#D-001810-10-05
ON-TARGETplus Human CHMP2A SMARTPool siRNA	Horizon Discovery	Cat#L-020247-01-0005
Ultramer repair templates, gRNAs, and primers for gene editing validation are described in Table S1	IDT	N/A
Recombinant DNA		
pTetOFF a-syn A53T	This study	pCS1; RRID:Addgene_215372
pCMV-EGFP-RNF152-IRES-mScarlet-I	This study	pCS2; RRID:Addgene_215373
pCMV mRuby3-Galectin-3	This study	pCS3; RRID:Addgene_ 215375
pCMV mClover3-Galectin-3	This study	pCS4; RRID:Addgene_ 215376
pCMV a-syn-A53T-mRuby3	This study	pCS5; RRID:Addgene_ 215379
pCMV a-syn-A53T-mClover3	This study	pCS6; RRID:Addgene_ 215378
pEF1a mNeonGreen-3K-B1-10-IRES-mKate2-2A-PuroR	This study	pCS7; RRID:Addgene_ 215377
pSPcas9(BB)-2A-Puro V2.0	Ran et al.[157]	RRID:Addgene_62988
pSPcas9(BB)-2A-Puro V2.0 sgCHMP2B-2 aauucccaaaugaagauggc	This study	pCS8; RRID:Addgene_ 231998
pCMV mTagBFP2	This study	pCS9; RRID:Addgene_ 231999
pCMV mTagBFP2-2A-CHMP2B	This study	pCS10; RRID:Addgene_ 232000
pCMV mTagBFP2-2A-CHMP2B-Q165X	This study	pCS11; RRID:Addgene_ 232001
pCMV CHMP2B-3XHA	This study	pCS12; RRID:Addgene_ 232002
pCMV CHMP2B-L4D,F5D-3XHA	This study	pCS13; RRID:Addgene_ 232003
pCMV CHMP2B-L4D F5D-d10-52-3xHA (Δα1)	This study	pCS14; RRID:Addgene_ 232004
pCMV CHMP2B-L4D F5D-d55-96-3xHA (Δα2)	This study	pCS15; RRID:Addgene_ 232005
pCMV CHMP2B-L4D F5D-d97-106-3xHA (Δα2/3 loop)	This study	pCS16; RRID:Addgene_ 232006
pCMV CHMP2B-L4D F5D-d106-113-3xHA (Δα3)	This study	pCS17; RRID:Addgene_ 232007
pCMV CHMP2B-L4D F5D-d118-138-3xHA (Δα4)	This study	pCS18; RRID:Addgene_ 232008
pCMV CHMP2B-L4D F5D-d55-138-3xHA (Δα2-4)	This study	pCS19; RRID:Addgene_ 232009
pCMV CHMP2B-L4D F5D-d159-174-3xHA (Δα5)	This study	pCS20; RRID:Addgene_ 232010
pCMV CHMP2B-L4D F5D-d201-213-HA (ΔVPS4 binding)	This study	pCS21; RRID:Addgene_ 232011
pEF1a FLAG-CHMP2B	This study	pCS22; RRID:Addgene_ 232012
pEF1a FLAG-CHMP2B-d55-96	This study	pCS23; RRID:Addgene_ 232013
pCMV sfGFP-CHMP2B-55-96	This study	pCS24; RRID:Addgene_ 232014

(*Continued on next page*)

Continued

REAGENT or RESOURCE	SOURCE	IDENTIFIER
pCMV sfGFP-CHMP2B-3x-55-96	This study	pCS25; RRID:Addgene_ 232015
pCMV sfGFP-CHMP2B-201-213	This study	pCS26; RRID:Addgene_ 232016
pT7-7 a-syn A53T	Rospigliosi et al.[158]	RRID:Addgene_105727
pT7-7 a-syn A53T D115A mNeonGreen-3K-B11	This study	pCS27; RRID:Addgene_ 232017
pET28 His-SUMO-CHMP2B	This study	pCS28; RRID:Addgene_ 232018
pMD2.G	pMD2.G was a gift from Didier Trono	RRID:Addgene_12259
psPAX2	psPAX2 was a gift from Didier Trono	RRID:Addgene_12260
pET-Sac-Abeta(M1-42)	Linse[159]	RRID:Addgene_71875
pLJC5-Tmem192-3xHA	Abu-Remaileh et al.[130]	RRID:Addgene_102930
pDEST HisAsCpf1	Kraus et al.[160]	N/A
phSyn2 sfGFP-RNF152	This study	pCS29; RRID:Addgene_215374
pCMV CHMP2B-L4D,F5D-V82E-3XHA	This study	pCS30; RRID:Addgene_242393
pCMV CHMP2B-L4D,F5D-M85E-3XHA	This study	pCS31; RRID:Addgene_242416
pCMV CHMP2B-L4D,F5D-M92E-3XHA	This study	pCS32; RRID:Addgene_242417
pCMV CHMP2B-L4D,F5D-V82E M85E M92E-3XHA	This study	pCS33; RRID:Addgene_242418
pLKO.1 mouse NT	This study	pCS34; RRID:Addgene_242421
pLKO.1 mouse CHMP2B	This study	pCS35; RRID:Addgene_242422
pCMV CHMP2Bchimera-L4D,F5D-CHMP6α2-3XHA	This study	pCS36; RRID:Addgene_242419
pCMV sfGFP-CHMP6 57–98	This study	pCS37; RRID:Addgene_242420
N1-TauRD (P301L/V337M)-EYFP	Sanders et al.[161]	N/A
pHUE-TauRD (C291A/P301L/C322A/V337M)	Yuste-Checa et al.[162]	N/A
Software and algorithms		
Fiji 1.54F	Schindelin et al.[163]	RRID:SCR_002285; https://fiji.sc
Matlab R2020b	Mathworks	RRID:SCR_001622; http://www.mathworks.com/products/matlab/
Graphpad Prism 8	Dotmatics	RRID:SCR_002798; http://www.graphpad.com/
ZEN 2.6	Zeiss	RRID:SCR_013672; https://www.zeiss.com/microscopy/en/products/software/zeiss-zen.html
MATLAB Flow Cytometry Analysis - Flow Cytometry data analysis toolkit for Matlab	This study	RRID:SCR_026125; Zenodo: https://doi.org/10.5281/zenodo.14411900; https://github.com/csitron/MATLAB-Programs-for-Flow-Cytometry
MATLAB Immunoblot Quantification – Quantification of the intensity of bands on a western blot in Matlab	This study	RRID:SCR_026124; Zenodo: https://doi.org/10.5281/ze nodo.14411929; https://github.com/csitron/Western-Blot-Quantification-in-MATLAB
Microscopy lif Channel Quant MATLAB - Quantification of positive channel area in Matlab from lif files	This study	RRID:SCR_026188; Zenodo: https://doi.org/10.5281/zenodo.14411941; https://github.com/csitron/Microscopy_lif_Channel_Quant_MATLAB
Microscopy lif Adjust MATLAB - Batched microscopy image contrast adjustment and pseudocoloring in Matlab	This Study	RRID:SCR_026187; Zenodo: https://doi.org/10.5281/zenodo.14411935; https://github.com/csitron/Microscopy_lif_Adjust_MATLAB

(*Continued on next page*)

Continued

REAGENT or RESOURCE	SOURCE	IDENTIFIER
Amino acid composition and hydrophobicity analysis -bioinformatics to analyze the amino acid content and hydrophobicity profile of a given set of protein sequences in a fasta file in Matlab	This study	RRID:SCR_026281; Zenodo: https://doi.org/10.5281/zenodo.14637057; https://github.com/csitron/Amino_acid_composition_and_hydrophobicity_analysis
Leica Applications Suite X 3.5.7.23225	Leica	RRID:SCR_013673; https://www.leica-microsystems.com/products/microscope-software/p/leica-las-x-ls/
FEI MAPS 2.1 and 3.8	FEI	RRID:SCR_018738; http://www.fei.co.jp/_documents/CorrSightDatasheet.pdf
NIS-Elements 5.21.03	Nikon	RRID:SCR_014329; https://www.microscope.healthcare.nikon.com/en_EU/products/software/nis-elements/software-resources
Attune™ Cytometric Software 5.1.2111.1	Thermo Fisher Scientific	N/A; https://www.thermofisher.com/de/en/home/life-science/cell-analysis/flow-cytometry/flow-cytometers/attune-nxt-flow-cytometer/software.html
Cytiva Amersham ImageQuant 800 Control Software	Cytiva	N/A; https://www.cytivalifesciences.com/en/us/shop/protein-analysis/molecular-imaging-for-proteins/imaging-systems/amersham-imagequant-800-systems-p-11546?srsltid=AfmBOoqGOKRP31R6BqnSdqFpfeJZnjfSKA6yKOY43t3byI4xX30yImGn
Clustal omega	Madeira et al.[164]	RRID:SCR_001591; https://www.ebi.ac.uk/jdispatcher/msa/clustalo
Microscopy tif Channel Quant MATLAB - quantification of fluorescence channel area in TIFF images using Matlab	This study	RRID:SCR_026999; Zenodo: https://doi.org/10.5281/zenodo.15489358; https://github.com/csitron/Microscopy_tif_Channel_Quant_MATLAB
Microscopy lif Channel Masked Intensity Quant MATLAB - Quantification of masked fluorescence intensity and nuclear count from.lif files in Matlab	This study	RRID:SCR_026998; Zenodo: https://doi.org/10.5281/zenodo.15489352; https://github.com/csitron/Microscopy_lif_Channel_Masked_Intensity_Quant_MATLAB
Other		
Superdex 200 Column	GE	Cat#28989335
MonoQ HR 16/10 20 mL Column	Amersham	Cat#17-0506-01
HisTrap Columns	Cytiva	Cat#17524802
Superdex 75 Column	GE	Cat#GE17-5174-01
Hitrap Heparin HP Column	Sigma-Aldrich	Cat#17-0407-03
50 kDa MWCO Centriprep YM-50 column	Merck	Cat#4311
Nanodrop One	Thermo Fisher Scientific	https://www.thermofisher.com/eg/en/home/industrial/spectroscopy-elemental-isotope-analysis/molecular-spectroscopy/uv-vis-spectrophotometry/instruments/nanodrop/instruments/nanodro-one.html; RRID:SCR_021242
BioRuptor Plus	Diagenode	Cat#B01020001; RRID:SCR_023470
FEI CorrSight	FEI	https://www.maastrichtuniversity.nl/sites/default/files/2023-03/corrsight_-_product_flyer.pdf

(*Continued on next page*)

Continued

REAGENT or RESOURCE	SOURCE	IDENTIFIER
Leica SP8 Falcon	Leica	https://www.leica-microsystems.com/products/confocal-microscopes/p/leica-tcs-sp8/; RRID:SCR_018169
Zeiss LSM800 with Airyscan	Zeiss	https://microscopy.anu.edu.au/facilities/equipment/zeiss-lsm800-airyscan; RRID:SCR_015963
Eclipse Ti-2 with Yokogawa W1 spinning disk confocal	Nikon	https://www.microscope.healthcare.nikon.com/products/confocal-microscopes/csu-series/csu-w1; RRID:SCR_021242
Amersham ImageQuant 800 biomolecular imager	Cytiva	https://www.cytivalifesciences.com/en/us/shop/protein-analysis/molecular-imaging-for-proteins/imaging-systems/amersham-imagequant-800-systems-p-11546?s_kwcid=AL
Attune NxT Flow Cytometer	Thermo Fisher Scientific	https://www.thermofisher.com/us/en/home/life-science/cell-analysis/flow-cytometry/flow-cytometers/attune-acoustic-focusing-flow-cytometer.html; RRID:SCR_019590
Desalting Column	Cytiva	Cat#17508702
Low bind 1.5 mL centrifuge tubes	Eppendorf	Cat#30108116
Econo-Pac Disposable Chromatography Columns	Bio-Rad	Cat#7321010
Poly-L-lysine-coated coverslips	Neuvitro	Cat#GG-12-1.5-PLL
Epredia glass slides	Thermo Fisher Scientific	Cat#17294884
NuPAGE 1.5 mm 4-12% Bis-Tris gels	Thermo Fisher Scientific	Cat#NP0323BOX
NuPAGE 1 mm 12% Bis-Tris gels	Thermo Fisher Scientific	Cat#NP0342BOX
PVDF membrane	Sigma-Adlrich	Cat#3010040001
0.2 μm pore size cellulose acetate membrane	GE	Cat#10404131
Slot blot vacuum manifold	Hoefer	Cat#PR648
4–20% Criterion™ TGX Stain-Free™ Protein Gel, 18 well	Bio-Rad	Cat#5678094
ChemiDoc MP Imaging System	Bio-Rad	Cat#12003154; RRID:SCR_01903
Source 30S	Cytiva	Cat#17127301
Purification of α-synuclein from E. coli – protocols.io	Trinkaus et al.[72]	https://doi.org/10.17504/protocols.io.btynnpve
Filter trap assay for the detection of alpha-synuclein aggregation – protocols.io	This study	https://doi.org/10.17504/protocols.io.x54v92re4l3e/v1
Quantification of endolysosomal leak of alpha-synuclein fibrils by fluorescence complementation – protocols.io	This study	https://doi.org/10.17504/protocols.io.q26g71dr8gwz/v1
In vitro coimmunoprecipitation between CHMP2B and alpha-synuclein – protocols.io	This study	https://doi.org/10.17504/protocols.io.8epv5rb66g1b/v1
Mild Immunoprecipitation with Low Background – protocols.io	This study	https://doi.org/10.17504/protocols.io.eq2lywe9pvx9/v1
Purification of CHMP2B – protocols.io	This study	https://doi.org/10.17504/protocols.io.bp2l623r1gqe/v1
Pulldown of protein aggregates with a biotinylated peptide – protocols.io	This study	https://doi.org/10.17504/protocols.io.261ge5wrwg47/v1
Small-scale LysoIP – protocols.io	This study	https://doi.org/10.17504/protocols.io.yxmvmep25g3p/v1

(*Continued on next page*)

Continued

REAGENT or RESOURCE	SOURCE	IDENTIFIER
Production of lentiviruses in Lenti-X cells – protocols.io	This study	https://doi.org/10.17504/protocols.io.n92ldmdyol5b/v1
Immunostaining – protocols.io	This study	https://doi.org/10.17504/protocols.io.e6nvwd7n7lmk/v1
Induction of aggregation in alpha-synuclein-expressing cells by treatment with preformed fibrils (PFFs) – protocols.io	This study	https://doi.org/10.17504/protocols.io.eq2lyjbbplx9/v1
Ubiquitin immunoprecipitation using an anti-ubiquitin nanobody – protocols.io	This study	https://doi.org/10.17504/protocols.io.dm6gp36k1vzp/v1
Primary neuronal cultures – protocols.io	Saha et al.[165]	https://doi.org/10.17504/protocols.io.ewov1ojwklr2/v1
Human pluripotent stem cell culture – protocols.io	Hoyer et al.[134]	https://doi.org/10.17504/protocols.io.j8nlkoq56v5r/v1
CRISPR editing of CHMP2B gene in KOLF2.1J AAVS-NGN2 iPSCs – protocols.io	This study	https://doi.org/10.17504/protocols.io.q26g71q68gwz/v1
Neural differentiation of AAVS1-TRE3G-NGN2 pluripotent stem cells – protocols.io	This study	https://doi.org/10.17504/protocols.io.x54v9p8b4g3e/v1
Tau Purification – Edmond Repository	Yuste-Checa et al.[162]	https://doi.org/10.17617/3.51VXU0
Tau Aggregation – Edmond Repository	Yuste-Checa et al.[162]	https://doi.org/10.17617/3.51VXU0

EXPERIMENTAL MODEL AND STUDY PARTICIPANT DETAILS

Cell culture

HEK293T cells were cultured in DMEM (Thermo Fisher Scientific, 11995073) containing 10% FBS (Thermo Fisher Scientific, 10270106) and 1X Penicillin-Streptomycin (Thermo Fisher Scientific, 15140163) at 37°C and 5% CO_2. HEK293T TetOff-α-syn-A53T cells were cultured in 2 μg/mL Blasticidin S (Thermo Fisher Scientific, A1113903). HEK293T TetOff-α-syn-A53T EGFP-RNF152-IRES-mScarlet-I, HEK293T TetOff-α-syn-A53T mRuby3-Galectin-3 mClover3-Galectin-3, HEK293T α-syn-A53T-mRuby3 α-syn-A53T-mClover3, and HEK293T TetOff-a-syn-A53T TauRD (P301L/V337M)-EYFP cells were cultured in 2 μg/mL Blasticidin S and 225 μg/mL G418 (Thermo Fisher Scientific, 10131035). HEK293T TetOff-α-syn-A53T mNeonGreen-3K-1-10-IRES-mKate2 cells were cultured in 2 μg/mL Blasticidin S and 200 ng/mL Puromycin (Thermo Fisher Scientific, A1113803). Cells were passaged using TrypLE Express (Thermo Fisher Scientific, 12605036). Cultures were regularly checked for mycoplasma contamination.

Drug treatments were performed for the indicated amounts of time by addition of compounds dissolved in DMSO, except for LLOMe (Santa Cruz, sc-285992B) and Leupeptin (Sigma Aldrich, 11017101001), which were dissolved in PBS. Each time a drug treatment was performed, a control using an equal volume of the appropriate solvent (DMSO or PBS) was used for comparison.

HEK293T TetOff-α-syn-A53T cells were created by transduction with pTetOFF α-syn A53T virus (details about virus transduction below). The transduced cells were then selected with 10 μg/mL Blasticidin S. Monoclones were isolated by single-cell sorting with a BD FACS Aria III (BD Biosciences). HEK293T TetOff-α-syn-A53T EGFP-RNF152-IRES-mScarlet-I and HEK293T TetOff-α-syn-A53T mRuby3-Galectin-3 mClover3-Galectin-3 cell lines were produced in this genetic background by transfection with either pCMV-EGFP-RNF152-IRES-mScarlet-I or pCMV mRuby3-Galectin-3 and pCMV mClover3-Galectin-3, respectively, using Lipofectamine 3000 (Thermo Fisher Scientific, L3000008). Stably transfected polyclonal cell lines were then created by selection with 1 mg/mL G418. Monoclones of these two cell lines were then isolated by limiting dilution. The HEK293T TetOff-α-syn-A53T mNeonGreen-3K-1-10-IRES-mKate2 polyclonal cell line was created by transducing HEK293T TetOff-α-syn-A53T with pEF1a mNeonGreen-3K-B1-10-IRES-mKate2-2A-PuroR virus, and selecting with 2 μg/mL Puromycin.

HEK293T α-syn-A53T-mRuby3 α-syn-A53T-mClover3 cells were produced by transfection with pCMV α-syn-A53T-mRuby3 and pCMV α-syn-A53T-mClover3 with Lipofectamine 3000, followed by selection with 1 mg/mL G418. Monoclones were then isolated by single-cell sorting on a BD FACS Aria III.

HEK293T TetOff-a-syn-A53T TauRD (P301L/V337M)-EYFP cells were produced by Lipofectamine 3000 transfection of N1-TauRD (P301L/V337M)-EYFP[161] and selection with 1 mg/mL G418.

Primary cortical neuron cultures were produced from E15.5 CD-1 wild-type mouse embryos. All mouse experiments were performed in accordance with the relevant guidelines and regulations of the Government of Upper Bavaria, Germany. Mice were maintained in a pathogen-free animal facility at 22 ± 1.5°C, 55 ± 5% humidity, with a 14/10 hr light/dark cycle. Mice were allowed food and water access ad libitum. Pregnant females were sacrificed by cervical dislocation. The uterus was then dissected from the sacrificed animal and submerged into a 10 cm sterile dish on ice filled with Dissection Medium: Hank's balanced salt solution and 10 mM

HEPES, 10 mM $MgSO_4$, and 1X Penicillin-Streptomycin. Choosing sexes randomly, heads were cut from the embryos and the brains were removed and submerged into Dissection Medium on ice. Cortical hemispheres were then dissected and the meninges were removed. 6-7 embryos worth of cortical tissue was then digested in a 15 mL conical with 0.25% Trypsin-EDTA solution (Sigma Aldrich, T4049), 1 mM EDTA, and 15 μL DNAse I (Thermo Fisher Scientific, EN0521) at 37°C for 20 min. Trypsin was then quenched by washing the cortices settled at the bottom of the conical twice with Neurobasal medium (Thermo Fisher Scientific, A3582901) supplemented with 5% FBS. To generate a single-cell suspension, the digested tissue was then triturated 15 times through a 1 mL pipette tip in 2 mL Neurobasal medium. Cells were then centrifuged at 130 x g and resuspended in Primary Neuron Culture Medium: Neurobasal medium, 2% B-27 Plus (Thermo Fisher Scientific, A3582801), 1% L-Glutamine (Thermo Fisher Scientific, 25030081), and 1X Penicillin-Streptomycin. Neurons were then counted and plated either at 1 x 10^5 neurons per well onto glass coverslips (VWR, 630-2190) in a 24-well plate or at 2 x 10^5 neurons per well of a 12-well plate. In both cases, the coverslips or wells were pre-coated with 1 mg/mL poly-D-lysine (Sigma, A-003-E) and 1 μg/mL laminin (Thermo Fisher Scientific, 23017015). The day of plating was considered day in vitro (DIV) 0. A detailed protocol can be found at https://doi.org/10.17504/protocols.io.ewov1ojwklr2/v1.

The KOLF2.1J AAVS1-TRE3G-NGN2 cell line was previously described.[166] During the generation of mutant cell lines in this background (described below), cells were cultured in StemFlex medium (Gibco, A3349401) at 37°C and 5% CO_2 on plates coated with Matrigel (Corning, 354277). iPSCs were passaged using 0.5 mM Ultrapure EDTA pH 8 (Thermo Fisher Scientific, 15575020). Details about handling these cultures can be found at https://doi.org/10.17504/protocols.io.j8nlkoq56v5r/v1, originally from Saha et al.[165]

METHOD DETAILS

Recombinant protein purification and aggregation

Recombinant α-syn A53T and variants thereof were purified based on published protocol.[167] BL21(DE3) *E. Coli* were transformed with pT7-7 α-syn A53T (Addgene #105727; a gift of Hilal Lashuel[158]) or pT7-7 α-syn A53T D115A mNeonGreen-3K-B11 (this study). The culture was grown in Terrific Broth (Sigma, T0918) at 37°C until OD600 = 0.8, at which point the culture was induced with 1 mM IPTG for 4 hr. Cell pellets were harvested and lysed by sonication for 5 min in High Salt Buffer: 750 mM NaCl, 50 mM Tris, 1 mM EDTA, cOmplete EDTA-free Protease Inhibitor (Roche, 5056489001), pH 7.6. The lysate was then boiled for 15 min, cooled on ice, and clarified by centrifugation at 6,000 x g for 20 min at 4°C. The clarified lysate was then dialyzed into Size Exclusion Buffer, consisting of 10 mM Tris, 50 mM NaCl, 1 mM EDTA, pH 7.6. The dialyzed protein was then purified further by size exclusion chromatography in a Superdex 200 column (GE, 28989335). Following size exclusion, the protein was dialyzed into Anion Exchange Buffer containing 10 mM Tris, 25 mM NaCl, 1 mM EDTA, pH 7.6. The dialyzed protein was run on a MonoQ column (Amersham, 17-0506-01) and eluted with a linear gradient of 25 mM to 1 M NaCl in Anion Exchange Buffer. The anion-exchanged protein was then dialyzed into 50 mM Tris, 150 mM KCl, pH 7.5, concentrated to 5 mg/mL, frozen, and stored at -80°C until use. A detailed protocol can be found at https://doi.org/10.17504/protocols.io.btynnpve.

α-Syn PFFs were produced based on an established protocol.[95] 5 mg/mL recombinant α-syn A53T or α-syn A53T D115A mNeonGreen-3K-B11 was centrifuged for 1 hr at 100,000 x g at 4°C. The supernatant was then added to a new 1.5 mL tube and shaken for 24 hr in a Thermomixer (Eppendorf) at 900 rpm and 37°C.

α-Syn PFFs were labeled with Alexa Fluor 647 NHS Ester (Thermo Fisher Scientific, A20006) according to the manufacturer's instructions. 5 mg of PFFs were pelleted by 30 min of 20,000 x g centrifugation and resuspended in 0.1 M $NaHCO_3$, pH 8.3. The PFFs were then reacted with 0.5 mg of Alexa Fluor Ester dissolved in DMSO (Thermo Fisher Scientific, D12345) for 1 hr at room temperature with shaking at 400 rpm, protected from light. The PFFs were then washed by 5 rounds of pelleting with a 20,000 x g centrifugation for 30 min and resuspension in 0.1 M $NaHCO_3$, pH 8.3. After the final wash, the PFFs were finally resuspended in PBS, pH 7.2 (Thermo Fisher Scientific, 20012068) at a concentration of 5 mg/mL.

CHMP2B was expressed as a His-SUMO fusion protein in BL21(DE3) *E. Coli* transformed with pET28-His-SUMO-CHMP2B (this study). After outgrowth at 30°C, the culture was shifted to 18°C and induced with 0.5 mM IPTG for 16 hr. Pellets were lysed by sonication for 20 min in Lysis Buffer containing 50 mM Tris, 500 mM NaCl, 10 mM imidazole, 2 mM β-Mercaptoethanol (β-ME), 5% glycerol, cOmplete EDTA-free Protease Inhibitor, pH 8. The lysate was then clarified by centrifugation and run over 3 connected 5 mL HisTrap columns (Cytiva, 17524802), followed by elution with a gradient of 50 mM to 500 mM imidazole in a buffer of 50 mM Tris, 500 mM NaCl, 2 mM β-ME, pH 8.0. To cleave the His-SUMO tag, the eluted His-SUMO-CHMP2B was then combined with His-SenP2 protease (7500 U per L of culture, Max Planck Institute of Biochemistry Core Facility) and glycerol to 10%; the mixture was dialyzed overnight in 20 mM Tris, 150 mM NaCl, 4 mM imidazole, 2 mM β-ME, pH 7.5. To separate the cleaved CHMP2B from His-SUMO, a reverse HisTrap column was then performed as above with two alterations: the buffers were instead at pH 7 and the flow-through was collected instead of the eluate. The CHMP2B in the flow-through was then subjected to size exclusion chromatography in a Superdex 200 column using 20 mM Tris, 150 mM NaCl, 2 mM β-ME, pH 7. Glycerol was added to the eluted CHMP2B to a final concentration of 10%, then the sample was concentrated to 1.11 mg/mL. A detailed protocol can be found at https://doi.org/10.17504/protocols.io.bp2l623r1gqe/v1.

Aβ42 was purified from inclusion bodies as in the "without urea" protocol described in Linse.[159] BL21(DE3) *E Coli* were transformed with the pET-Sac-Abeta(M1-42) plasmid (Addgene #71875; a gift of Sarah Linse[168]), grown in LB media at 37°C, and induced with 0.4 mM IPTG for 4 hr. Bacterial pellets from a 3 L culture were sonicated in 50 mL TE7.5 Buffer (10 mM Tris, 1 mM EDTA, cOmplete

EDTA-free Protease Inhibitor, 2 U/mL Benzonase (Max Planck Institute of Biochemistry Core Facility RRID:SCR_025741), pH 7.5) until the sample appeared homogenous. To clean the pellets, the lysate went through two washing steps consisting of centrifugation at 18,000 x g for 8 min at 4°C, discarding of the supernatant, and sonication of the pellet in TE7.5 Buffer. The sample was then pelleted, resuspended in 40 mL TE9.5 Buffer (10 mM Tris, 1 mM EDTA, pH 9.5), sonicated, and centrifuged at 18,000 x g for 10 min at 4°C. The supernatant was filtered and adjusted to pH 8.5 with 1 M HCl. The pH-adjusted supernatant was then passed through a self-packed column of DEAE sepharose (GE, 17-0709-01) equilibrated with TE8.5 Buffer (10 mM Tris, 1 mM EDTA, pH 8.5). Aβ42 was then eluted with TE8.5 containing 50 mM NaCl. The eluted Aβ42 then underwent buffer exchange into TE8.5 Buffer via a desalting column (Cytiva, 17508702). The buffer-exchanged Aβ42 was then lyophilized.

To prepare Aβ42 monomers and aggregates, 500 μg of lyophilized Aβ42 was resuspended in 700 μL 6M GuHCl, 20 mM sodium phosphate, pH 8.5. The solubilized Aβ42 was then subjected to size exclusion chromatography on a Superdex 75 column (GE, GE17-5174-01) in Aβ42 Aggregation Buffer containing 20mM sodium phosphate, 0.2 mM EDTA, pH 8.5. The eluted monomeric Aβ42 was pooled and its concentration was determined by 205 nm absorbance on a Nanodrop One (Thermo Fisher Scientific). The concentration of Aβ42 monomers was adjusted to 10 μM in Aβ42 Aggregation Buffer. Part of the pool of Aβ42 monomers was snap-frozen in low-bind tubes (Eppendorf, 0030108116) and stored, while the rest was aggregated. To aggregate Aβ42, the monomers were aliquoted into a 96-well plate (Corning, 3881) at 80 μL per well, and incubated at 37°C for 24 hr. The aggregates were then snap-frozen and stored at -80°C.

To purify Cpf1, a 500 mL culture of Rosetta (DE3)pLysS *E. Coli* cells (Merck, 70956) transformed with the pDEST-his-AsCpf1-EC plasmid[160] was grown at 37°C in LB media containing 50 μg/mL chloramphenicol and 34 μg/mL kanamycin with shaking until OD600 reached 0.6-1. The culture was cooled to <20°C in an ice bath before induction with 0.5 mM IPTG, followed by overnight shaking at 16–20°C. Cells were harvested by centrifugation and stored at −80°C. The cell pellet was resuspended in 25 mL lysis buffer (50 mM HEPES-NaOH, 150 mM NaCl, 5 mM MgCl2, 20 mM imidazole, 0.5 mM TCEP, pH 7.0). The resuspended cells were lysed by the addition of 2.5 mL 10X FastBreak buffer (Promega, V8571). Lysis was enhanced by 15 min Benzonase (Merck, 71205-M) treatment in 4 μL increments, as needed, to reduce viscosity. Once DNA was digested, the salt concentration was then adjusted to 500 mM by adding 5 M NaCl. Insoluble material was removed by centrifugation at 38,000 x g for 10 min at 4°C. 4 mL pre-washed Ni-NTA resin (Thermo Fisher Scientific, 88221) was equilibrated in a buffer of 50 mM HEPES-NaOH, 500 mM NaCl, 5 mM MgCl2, 20 mM imidazole, pH 7.0. Clarified lysate was bound to this resin at 4°C for 1 hr with gentle rotation. The slurry was loaded into a disposable column (Bio-Rad, 7321010) and washed three times with 20 mL high-salt buffer (50 mM HEPES-NaOH, 2 M NaCl, 20 mM imidazole, 0.5 mM TCEP, pH 7.0) and twice eluted with 5 mL elution buffer (50 mM HEPES-NaOH, 5 mM MgCl2, 400 mM imidazole, 0.5 mM TCEP, pH 7.0). Eluates were diluted 4-fold with PBS and loaded onto a Hitrap Heparin HP Column (Sigma, 17-0407-03) pre-equilibrated with PBS pH 7.4. The heparin column was washed with 20 mL of 0.1 M NaCl and eluted sequentially with 10 mL of PBS pH 7.4 containing increasing NaCl concentrations (0.3 M, 0.5 M, 0.7 M, 1.0 M, 2.0 M). Fractions judged by SDS-PAGE to contain purified Cpf1 were pooled and concentrated to 3 mL using a 50 kDa MWCO Centriprep YM-50 column (Merck, 4311). The sample was twice brought to 15 mL in PBS with 20% Glycerol and 2 mM TCEP, then concentrated to 3 mL with the Centriprep column. The final preparation was briefly centrifuged, sterilized using a syringe filter, and quantified by 280 nm absorbance on a NanoDrop. Purified protein was stored at 4 mg/mL at −80°C.

Tau was purified from BL21(DE3) *E Coli* transformed with the plasmid pHUE-TauRD (C291A/P301L/C322A/V337M),[162] which expresses Tau as an N-terminal His_6-ubiquitin fusion. Cultures were grown in Terrific Broth and induced at an OD600 of 0.5-0.8 with 0.4 mM IPTG overnight at 37°C. Cell pellets were lysed in 50 mM PIPES-NaOH, 250 mM NaCl, 10 mM imidazole, 2 mM β-ME, 1 mg/ml lysozyme (Sigma-Aldrich, L6876), cOmplete EDTA-free Protease Inhibitor, and Benzonase, pH 6.5. Lysates were sonicated and clarified by 1 hr centrifugation at 40,000 × g and 4°C, then bound to a HisTrap column. The column was then washed and eluted in base PIPES buffer containing 50 mM PIPES-NaOH and 2 mM β-ME, pH 6.5 - the column was first washed with high-salt PIPES buffer (500 mM NaCl and 10 mM imidazole), washed again with 250 mM NaCl and 50 mM imidazole PIPES wash buffer, then eluted with 50 mM NaCl and 250 mM imidazole PIPES elution buffer. Eluates were diluted 1:5 in base PIPES buffer and digested overnight at 4°C with Usp2 (Max Planck Institute of Biochemistry Core Facility) to remove the His_6-ubiquitin tag. Cleaved protein was further purified via a 0-500 mM NaCl gradient in PIPES buffer on a Source 30S cation exchange column (Cytiva, 17127301). The ion-exchanged TauRD was then further purified by size exclusion in PBS, pH 7.2 on a Superdex column. To produce PFF-TauRD aggregates, 10 μM TauRD was combined with 2.5 μM heparin (Merck, H3393) and 2 mM $MgCl_2$ at 37 °C with 850 rpm agitation for 1 hr. Protocols for TauRD purification and aggregation can be found at https://doi.org/10.17617/3.51VXU0.

iPSC gene editing

Mutations were made by gene editing, performed as described in Ordureau et al.[169] using a detailed protocol that can be found at: https://doi.org/10.17504/protocols.io.q26g71q68gwz/v1. To target the appropriate region of the CHMP2B gene, the SpCas9 sgRNA was generated by using the GeneArt Precision gRNA synthesis kit (Thermo Fisher Scientific) and the Cas12a (Cpf1) sgRNAs were ordered from Integrated DNA Technologies (IDT). The sequences of these sgRNAs (5' to 3') are as follows: GCCAAACAACTTGTGCATCTACGG [$CHMP2B^{-/-}$, CRISPR-Cas12a (Cpf1)], ATCAAGAACTTGATTCACAATATC [$CHMP2B^{Q165X/+}$, CRISPR-Cas12a (Cpf1)], and AGAGTTACGAGGTACACAGA ($CHMP2B^{I29V/I29V}$, CRISPR-SpCas9). Ultramer ssDNA oligos (IDT) were also designed to act as a homology-directed repair template in generating the point mutants, possessing the following sequences (bases that diverge from the genomic sequence capitalized): ccaactaagaaaagatgatgttcatacctttccagaaatttcaattccaatCt

catcaagaacttAattcacaatatcctggctttcttcttcgtcatcagaaccgtcaaagatgtc (CHMP2B$^{Q165X/+}$), and ctcctagatgtaataaaggaacagaatcga gagttacgaggtacacagagAgctataGtcagagatcgagcagctttagagaaacaagaaaaacagctggtaagtag (CHMP2B$^{I29V/I29V}$). Information about oligonucleotides used in gene editing can be found in Table S1.

Gene edits were introduced by first incubating 0.6 μg sgRNA with 3 μg SpCas9-NLS protein (UC Berkeley QB3 Macrolab) or 80 pmol sgRNA with 63 pmol Cas12a (Cpf1) protein for 10 min at room temperature, then electroporating the mixture into 2 x 10^5 KOLF2.1J AAVS1-TRE3G-NGN2 cells using a Neon Transfection System (Thermo Fisher Scientific). For the CRISPR-Cas12a (Cpf1) system, the cells were co-transfected with 39 pmol Alt-R Cpf1 Electroporation Enhancer (IDT, 1076301). For the point mutants, 80 pmol of the appropriate Ultramer ssDNA oligo was added to the electroporated CRISPR/Cas protein mixture. Cells then recovered for 1 day before single cells were sorted with a SH800S Cell Sorter (Sony Biotechnology).

Clones were then grown for 7-12 days before validation by DNA sequencing on a MiSeq (Illumina) as well as Sanger sequencing of PCR-amplified regions. The primer pairs used for amplification were: AAGAAAATGGCCAAGATTGGTA & CCATCTTCATTTGGGAA TTCAT (CHMP2B$^{-/-}$), TTGATGACATCTTTGACGGTTC & GAAATAAAAACCATGCACCTCC (CHMP2B$^{Q165X/+}$), and GGTTTCTTTTG TGATTCTCCTAG & CATGTGCCTTCTTCCTAGTTAGC (CHMP2B$^{I29V/I29V}$). Information about these genotyping oligonucleotides appear in Table S1. CHMP2B protein expression in sequencing-validated clones was then assessed by immunoblot.

iNeuron Differentiation

KOLF2.1J AAVS1-TRE3G-NGN2 background iPSCs were differentiated into iNeurons using the forced NGN2 expression protocol.[138] Prior to differentiation, iPSC lines were cultured in mTeSR Plus (Stem Cell Technologies, 100-0276) on Matrigel-coated plates at 37°C and 5% CO_2. The cells were passaged with ReLeSR (Stem Cell Technologies, 05873). For each differentiation, a single cell suspension of the iPSCs was generated by Accutase (Stem Cell Technologies, 07920) treatment and 2.5 x 10^5 cells were plated per well in a Matrigel-coated 6-well plate into ND1 medium: DMEM/F12, 1X NEAA (Gibco, 11140-068), 1X N2 (Thermo Fisher Scientific, 17502048), 10 ng/mL NT3 (Peprotech, AF-450-03-10), 10 ng/mL BDNF (Peprotech, 450-02), 200 ng/mL laminin (Bio-techne, 3446-005-01), and 2 μg/mL doxycycline (Clontech, 631311), supplemented with 10 μM Y-27632 (Biozol, S1049). The day of this first plating was considered DIV 0. On DIV 1, the media was exchanged for ND1 without Y-27632. On DIV 2, the media was exchanged for ND2 medium: Neurobasal, 1X Glutamax (Thermo Fisher Scientific, 35050061), 2% B-27 Plus, 10 ng/mL NT3, 10 ng/mL BDNF, and 2 μg/mL doxycycline. Half of the media was exchanged with fresh ND2 on DIV 4. On DIV 6, cells were split using Accutase and plated at 5 x 10^4 cells per well onto coverslips coated with 0.01% poly-L-ornithine (Sigma-Aldrich, P3655-50MG) and 10 μg/mL laminin in a 24-well plate. Half of the media was exchanged every 2 days thereafter with fresh ND2 media, with the media lacking doxycycline from DIV10 onwards. After addition of PFFs, the media was additionally supplemented with 1X Penicillin-Streptomycin. A detailed protocol for this differentiation can be found at https://doi.org/10.17504/protocols.io.x54v9p8b4g3e/v1.

Transfections, transductions, and knockdowns

For experiments involving expression of CHMP2B variants with their related controls or Cas9 with an sgRNA, plasmids were transfected using Fugene 6 (Promega, E2692). Cells at 70-80% confluence were transfected with a 4:1 (μL:μg) ratio of Fugene 6 to plasmid. Cells were replated the following day to avoid overgrowth of the culture.

For the strong CHMP2A and CHMP2B knockdown, the *CHMP2B* locus was first disrupted by transfection with an all-in-one plasmid encoding both Cas9 and an sgRNA with the sequence AAUUCCCAAAUGAAGAUGGC, pSPcas9(BB)-2A-Puro V2.0 sgCHMP2B-2. As a non-targeting control, cells were transfected with the parental pSPcas9(BB)-2A-Puro V2.0 plasmid (Addgene # 62988; a gift of Feng Zhang[157]). The cells were then selected with 2 μg/mL puromycin for 2 days. CHMP2A was then knocked down by reverse transfection; 1.5 x 10^5 cells were plated into the wells of a 12-well plate pre-loaded with reverse transfection mix: 12.5 pmol siPOOL siRNA against CHMP2A (siTOOLs Biotech, si-G020-27243) or a non-targeting negative control (siTOOLs Biotech, si-C002), 0.94 μL Lipofectamine 3000, and 36.9 μL Opti-MEM (Thermo Fisher Scientific, 31985-062). The media was exchanged the following day and measurements were taken after 72 hr of knockdown.

For the mild CHMP2A and CHMP2B knockdown, the *CHMP2B* locus was disrupted as above except for the puromycin selection, which was instead performed for two days. CHMP2A was then knocked down by transfecting a 60-70% confluent well of a 12-well plate with 100 pmol of ON-TARGETplus Human CHMP2A SMARTPool siRNA (Horizon Discovery, L-020247-01-0005) or ON-TARGETplus Non-targeting Pool siRNA (Horizon Discovery, D-001810-10-05) and 7.5 μL Lipofectamine 3000. Cells were then replated and measured 96 hr after knockdown.

To produce lentivirus, 2.5 x 10^6 Lenti-X 293T cells (Takara, 632180) were plated onto a 10 cm plate. The following day, cells were transfected with 0.65 pmol psPAX2 (Addgene #12260; a gift of Didier Trono), 0.36 pmol pMD2.G (Addgene #12259; a gift of Didier Trono), and 0.82 pmol of the desired lentiviral transfer vector using X-tremeGENE HP DNA Transfection Reagent (Sigma Aldrich, 6366244001) at a ratio of 4 μL per μg of transfer vector. The transfer vectors used were either phSyn2 sfGFP-RNF152 (this study), pLKO.1 mouse NT (this study), pLKO.1 mouse CHMP2B (this study), pLJC5-Tmem192-3xHA (Addgene #102930; a gift of David Sabatini[130]), pTetOFF α-syn A53T (this study), or pEF1a mNeonGreen-3K-B1-10-IRES-mKate2-2A-PuroR (this study). The following day, the media was exchanged with 9 mL of fresh DMEM. 72 hr after transfection, the media was collected, filtered, and mixed with 3 mL Lenti-X concentrator (Takara, 631231), and incubated at 4°C overnight. The viral precipitate was then concentrated by pelleting at 1500 x g for 45 min at 4°C and resuspending in 120 μL ice-cold PBS. This concentrated virus was then frozen and stored at -80°C. A detailed protocol can be found at: https://doi.org/10.17504/protocols.io.n92ldmdyol5b/v1.

To create stable HEK293T cell lines (detailed above in "cell culture"), cells were plated in 24-well plates and treated with 10 μL of concentrated virus and 0.5 μg/mL polybrene (Sigma Aldrich, TR-1003-G). Primary neurons were transduced by treatment with 1 or 2 μL of concentrated virus when they were cultured in 24-well plates or 12-well plates, respectively.

PFF treatment and induction of α-syn aggregation

For Lipofectamine 3000-mediated α-syn aggregation induction, HEK293T cells were first plated at 250 cells/mm^2 (e.g. 10^5 cells per well of a 12-well plate) for flow cytometry, immunoblot, or immunoprecipitation experiments or 125 cells/mm^2 (e.g. 2.5 x 10^4 cells per well of a 24-well plate) for microscopy experiments. On the following day, a 5 mg/mL aliquot of PFFs was thawed, diluted 1:20 in PBS, and sonicated in a BioRuptor Plus (Diagenode, B01020001) for 25 cycles of 5 seconds on and 5 seconds off. Opti-MEM and Lipofectamine 3000 were then mixed at a ratio of 50:3 and incubated for 5 min. In no Lipofectamine 3000 controls, an equal volume of Opti-MEM served as a substitute. The sonicated PFFs were then added to this pre-incubated mixture at a ratio of 50:3:20 (Opti-MEM: Lipofectamine 3000:diluted PFFs) to form the "seeding mixture." In no PFF controls, the PFFs were substituted by an equal volume of PBS. The seeding mixture was incubated for 10 min at room temperature, then added dropwise to wells. The volume of seeding mixture used was adjusted such that 1 μL of sonicated PFFs were added per 10 mm^2 of well surface area (e.g. 73 μL of seeding mixture used in 24-well plates and 146 μL in 12-well plates). The following day, the media was exchanged with fresh DMEM to minimize off-target effects of Lipofectamine 3000. Measurements were then taken 2 days after PFF treatment. A detailed protocol can be found at: https://doi.org/10.17504/protocols.io.eq2lyjbbplx9/v1.

Extended PFF treatment in HEK293T cells without Lipofectamine 3000 was performed exactly as described above with 4 alterations: 1) cells were instead plated at 32 cells/mm^2, 2) Lipofectamine 3000 was not used, 3) rather than a media exchange, half the volume of medium was spiked in after 3 days, and 4) measurements were taken 6 days after PFF treatment. PFF treatment in primary mouse neurons and iNeurons occurred as described above, although the plating density was as described in the "cell culture" and "iNeuron differentiation" sections, Opti-MEM was replaced with the appropriate growth medium, Lipofectamine 3000 was not used, and there was no full media exchange after PFF treatment. For iNeurons, instead of exchanging the media in the first media change after PFF treatment, half the well volume of media was spiked in and none was removed. In primary neuron experiments, PFFs were added on different days such that all measurements were taken on DIV 18 (e.g. PFFs added on DIV 4 for 14 day treatment and on DIV 11 for 7 day treatment). iNeurons were treated with PFFs on DIV 16.

For PFF-TauRD treatment, 10 μM TauRD was diluted 1:20 in PBS and sonicated in a BioRuptor Plus for 25 cycles lasting for 5 sec on and 5 sec off. Sonicated, diluted PFF-TauRD was then mixed with Opti-MEM at a 58.5:14.5 ratio. Using this mixture, 0.73 μL of sonicated PFF-TauRD was added per 10 mm^2 of plate surface area, equivalent to 73 μL into a well of a 24-well plate (i.e. 100 ng of PFF-TauRD per well). These cells were then incubated for 2 days before fixation.

Immunofluorescence Microscopy

For immunofluorescence microscopy, HEK293T cells were grown on poly-L-lysine-coated coverslips (Neuvitro, GG-12-1.5-PLL), iNeurons were grown on poly-L-ornithine- and laminin-coated coverslips (described above), and primary neurons were grown on poly-D-lysine- and laminin-coated coverslips (described above). Cells growing on coverslips were fixed by 4% PFA (Thermo Fisher Scientific, 28908) for 10 min at room temperature. Permeabilization was then carried out in 0.1% Triton X-100 in PBS for 5 min at room temperature. The cells were blocked for 1 hr in a Blocking Solution consisting of PBS, 5% milk powder (Sucofin), 0.1% Triton X-100, pH 7.4. Primary antibodies were diluted in Blocking Solution and incubated on the coverslips overnight at 4°C. All primary antibodies were used at 1:500 dilution, except for anti-MAP2 (Merck Millipore, AB5543) at 1:1500 and anti-CHMP3 (Santa Cruz, sc-166361) at 1:100. Coverslips were then washed three times in PBS before incubation with secondary antibodies diluted in Blocking Solution for 3 hr at room temperature protected from light. Secondary antibodies (listed in the STAR Resources table) were diluted 1:1000. Coverslips were then washed with PBS. Where appropriate, phalloidin staining was then carried out using 1:1000 diluted Phalloidin-iFluor 647 Reagent (Abcam, ab176759) in PBS with 1% BSA, 0.02% Triton X-100, pH 7.2 for 45 min before proceeding to nuclear staining. Nuclei were stained with NucBlue (Thermo Fisher Scientific, R37606) for 5 min, followed by two more PBS washes. Dako Fluorescence Mounting Medium (Agilent, S3023) was used to mount coverslips on Epredia glass slides (Thermo Fisher Scientific, 17294884). A detailed protocol can be found at: https://doi.org/10.17504/protocols.io.e6nvwd7n7lmk/v1.

Assessment of plasma membrane integrity was performed using Zombie NIR Fixable Viability Dye (Biolegend, 423119). Coverslips were washed once with warm DPBS (Thermo Fisher Scientific, 14040174) before staining for 15 min in 1:1000 dye diluted in warm DPBS. As a positive control, the staining buffer contained 0.006% Saponin (Sigma-Aldrich, 47036). Dye was then quenched by a wash in 10% FBS, diluted in DPBS. The coverslips were once washed with DPBS before continuing with fixation, permeabilization, nuclear staining, and mounting, as described above.

Images were acquired either with a FEI CorrSight using a 63X oil objective running FEI MAPS 2.1 or 3.8 (FEI), a Leica SP8 Falcon using a 63X oil objective running Leica Applications Suite X 3.5.7.23225 (Leica; Max Planck Institute of Biochemistry Imaging Facility), a Zeiss LSM800 using a 40X Plan-Apochromat objective in Airyscan super resolution mode running Zen 2.6 (Zeiss), or a W1 spinning disk confocal (Yokogawa) on an Eclipse Ti-2 (Nikon) with a 100X oil Plan-Apochromat objective (Harvard Medical School Core for Imaging Technology & Education) running NIS-Elements 5.21.03.

For figure preparation, fluorescence microscopy images were contrast-adjusted for the purpose of visualization. Prior to further analysis, Airyscan images acquired on the LSM980 were first processed in ZEN software (Zeiss). For images generated on the

CorrSight, LSM800, and Eclipse microscopes, figure panels of micrographs were prepared in Fiji.[163] Images acquired on the SP8 falcon were processed using a MATLAB script, deposited at https://github.com/csitron/Microscopy_lif_Adjust_MATLAB. In all cases, adjustments were applied uniformly to the entire image. For directly compared images, the same minimum and maximum intensity cutoff values were used.

In some cases, minimum intensity cutoffs were set uniformly across images in the same panel to compensate for antibody staining in areas of the coverslip clearly not occupied by cells (e.g., the CHMP2B antibody on the mouse primary neurons in Figures 1D and S1C). This was done to clarify the location of the stronger intracellular signal. In these cases, exact values used for intensity cutoffs can be found in the deposited data (Zenodo: https://doi.org/10.5281/zenodo.14506781).

Certain images exhibited very low background, particularly in situations where no signal was expected, such as pS129 α-syn staining in cells without aggregation induction or split mNeonGreen in conditions without complementation (e.g., Figures S7C and S7F). For pS129 α-syn, this is likely due to the high sensitivity and specificity of the anti-pS129 α-syn antibodies.[170] For split mNeonGreen, this is likely due to the negligible fluorescence produced by uncomplemented split mNeonGreen variants.[171]

Image quantification of pixel intensities was performed on non-contrast-adjusted images. These analyses were conducted in Matlab using the following scripts, deposited at Github: pSer129 α-syn area compared to nuclear (DAPI) area https://github.com/csitron/Microscopy_lif_Channel_Quant_MATLAB; pSer129 α-syn area compared to cytoplasmic area (MAP2), https://github.com/csitron/Microscopy_tif_Channel_Quant_MATLAB; CHMP2B signal in phalloidin-masked cytoplasmic area, https://github.com/csitron/Microscopy_lif_Channel_Masked_Intensity_Quant_MATLAB. pSer129 α-syn inclusions were manually counted from contrast-adjusted images.

Immunoblotting

For harsh lysis, HEK293T cells were harvested by trypsinization and lysed in RIPA Buffer (Thermo Fisher Scientific, 89900) supplemented with cOmplete Mini EDTA-free Protease Inhibitor Cocktail (Roche, 04693159001) and 7.5 U/mL Benzonase on ice. The lysate was then sonicated in a BioRuptor Plus for 5 cycles of 30 seconds on and 30 seconds off. The concentration was then determined using the Pierce Rapid Gold BCA Protein Assay Kit (Thermo Fisher Scientific, A53225) and equalized between samples. The lysate was then denatured by addition of one third of the sample volume of 4X NuPAGE LDS Sample Buffer (Thermo Fisher Scientific, NP0007) supplemented with 5% β-ME and boiling for 5 min at 95°C.

Primary neurons were lysed in the growth vessel by first washing with ice-cold PBS, then direct addition of the RIPA Buffer described above. The lysate was then sonicated and the concentrations were then equalized as described above. Total protein was precipitated from the lysate with 10% TCA. The protein pellets were then washed twice with ice-cold acetone and dried. The dried pellets were rehydrated with 300 mM Tris, pH 8.3, then treated with an equal volume of 4X NuPAGE LDS Sample Buffer with 5% β-ME and heated for 10 min at 70°C.

Samples were then run on NuPAGE 1.5 mm 4-12% Bis-Tris gels (Thermo Fisher Scientific, NP0323BOX) along with the PageRuler Prestained Protein Ladder (Thermo Fisher Scientific, 26617) and transferred to a PVDF membrane (Sigma Aldrich, 3010040001) for 1 hr at 100 V in Towbin Buffer (25 mM Tris, 192 mM glycine, pH 8.3) containing 20% methanol. For membranes stained for untagged α-syn, the membrane was fixed in 4% PFA for 30 min at room temperature after transfer.

For assessment of iPSC differentiation marker expression, lysates were run on Criterion TGX Stain free gels (Bio-Rad, 5678094) in Tris/Glycine/SDS buffer (Bio-Rad, 1610772), then transferred onto PVDF using Tris/Glycine buffer (Bio-Rad, 1610771).

To perform filter trap assays, cells were collected by trypsinization and lysed in 50 mM Tris, 150 mM NaCl, 1% Triton X-100, pH 7.5 supplemented with cOmplete Mini EDTA-free Protease Inhibitor Cocktail and 7.5 U/mL Benzonase. The lysate was then sonicated in a BioRuptor Plus for 3 cycles of 30 seconds on and 30 seconds off. The sonicated lysate underwent gentle clarification by centrifugation at 500 x g for 5 min at 4°C. After performing a BCA Gold assay to determine the protein concentration, the concentrations were then equalized and loaded onto a 0.2 μm pore size cellulose acetate membrane (GE, 10404131) in a slot blot vacuum manifold (Hoefer, PR648). A small sample of the lysate was then denatured with 4X NuPAGE LDS Sample Buffer with 5% β-ME and processed for SDS-PAGE to run as a loading control. More details can be found at: https://doi.org/10.17504/protocols.io.x54v92re4l3e/v1.

PVDF and cellulose acetate membranes were blocked for 1 hr at room temperature in Blocking Buffer: 5% milk powder in TBS-T (50 mM Tris, 150 mM NaCl, 0.1% Tween-20, pH 7.4). For assessment of iPSC differentiation, membranes were blocked and stained using Li-Cor Intercept (TBS) Blocking Buffer (Licor, 927-60001). Membranes were then probed with primary antibodies diluted in the appropriate blocking buffer overnight at 4°C. Concentrations of primary antibodies were as follows: 1:1000 rabbit anti-CHMP2A (Proteintech, 10477-1-AP), 1:2000 rabbit anti-CHMP2B (Abcam, ab33174), 1:2000 rabbit anti-α-synuclein MJFR1 (Abcam, ab138501), 1:2000 mouse anti-α-synuclein LB509 (Abcam, ab27766), 1:2000 rabbit anti-α-synuclein phosphoSer129 EP1536Y (Abcam, ab51253), 1:500 mouse anti-β-Amyloid (Biolegend, 803001), 1:100 mouse anti-LAMP1 (Developmental Studies Hybridoma Bank, H3A3), 1:2000 mouse anti-Ubiquitin (Santa Cruz, sc-8017), 1:2000 rat anti-GFP (Proteintech, 3h9-150), 1:5000 mouse anti-β-actin (Abcam, ab6276), 1:2000 mouse anti-GAPDH (Merck Millipore, MAB374), 1:1000 mouse anti-Hsp60 (Abcam, ab59458), 1:1000 rabbit anti-Calreticulin (Cell Signaling Technologies, 12238S), 1:1000 mouse anti-Calnexin (Santa Cruz, sc-46669), 1:1000 mouse anti-α-tubulin (Sigma Aldrich, T6199), 1:1000 rabbit anti-Synapsin I (Abcam, ab18814), 1:1000 rabbit anti-OCT4 (Cell Signaling Technologies, 2840S), 1:1000 mouse anti-HSP90 (Santa Cruz, sc-69703), 1:2000 rabbit anti-FLAG (Sigma-Aldrich, F7425). After three washes in TBS-T, the membrane was then stained with either 1:2000 anti-mouse HRP (Sigma Aldrich, A4416), 1:10000 anti-rabbit

HRP (Sigma Aldrich, A9169), 1:2000 anti-rat HRP (Sigma Aldrich, A9037), 1:10000 anti-mouse IRdye 680D (Licor, 926-68070), 1:10000 anti-rabbit IRdye 800D (Licor, 92632211), or 1:2000 Veriblot (Abcam, ab131366) diluted in the appropriate blocking buffer.

Membranes stained with HRP-conjugated secondary antibodies were then washed, developed with either Immobilon Forte or Classico Western HRP Substrate (Merck Millipore, WBLUF0500 or WBLUC0500), and imaged on an Amersham ImageQuant 800 biomolecular imager (Cytiva). IRdye-stained membranes were imaged on a ChemiDoc MP Imaging System (Bio-Rad, 12003154). Before re-probing previously-stained membranes, the membranes were first stripped using Restore Western Blot Stripping Buffer (Thermo Fisher Scientific, 21059) and then blocked and stained as described above.

Immunoblots were quantified using a custom Matlab script that has been deposited at https://github.com/csitron/Western-Blot-Quantification-in-MATLAB. Original, non-contrast-adjusted images were used for quantification. For figure preparation, images were first contrast adjusted such that no values for bands of interest fell below the minimum cutoff or above the maximum cutoff, ensuring that the quantitative relationship between bands was accurately portrayed. All contrast adjustments were applied uniformly across the entire image. If this adjustment resulted in an unacceptably low background, the maximum intensity cutoff was lowered to produce a pale gray background, corresponding to intensity values near 2000 arbitrary units out of a possible 65,535 (for 16-bit images). When the "pale gray background" adjustment caused bands to appear excessively strong, merge together, or lose distinction, we instead applied a higher maximum intensity cutoff, resulting in a lighter background. In cases where achieving a pale gray background would have compromised the integrity of the bands, we provide a comparison between the version used in the main figure and the pale gray-adjusted version in the deposited data (Zenodo: https://doi.org/10.5281/zenodo.14506781).

Immunoprecipitations and Pulldowns

For immunoprecipitation of CHMP2B and its variants from lysate, cells were collected by trypsinization and lysed in PBS, 0.1% Triton X-100, 0.02% Tween-20, pH 7.2 with cOmplete Mini EDTA-free Protease Inhibitor Cocktail and 0.75 U/mL Benzonase on ice. For immunoprecipitation of endogenous CHMP2B, the lysate was pre-clarified by 500 x g centrifugation at 4°C for 5 min and the affinity matrix was prepared by binding 2.67 μL of rabbit anti-CHMP2B or rabbit IgG isotype control (Abcam, ab37415) to 30 μL Protein G Dynabeads (Invitrogen, 10007D), then blocking the antibody-bound beads with PBS, 0.1% Triton X-100, 0.02% Tween-20, 3% BSA, pH 7.2 with cOmplete Mini EDTA-free Protease Inhibitor Cocktail. For immunoprecipitation of sfGFP-tagged CHMP2B fragments, 20 μL GFP-Trap Magnetic Agarose (Proteintech, gtma-20) beads were used on unclarified lysate. Beads were then incubated with 200 μg of lysate with an additional 113 mM NaCl (for a total of 250 mM NaCl) for 1 hr at 4°C with rotation. The beads were then washed three times in PBS, 0.1% Triton X-100, 0.02% Tween-20, 113 mM additional NaCl, pH 7.2. The bound protein was eluted by boiling with 2X NuPAGE LDS Sample Buffer with 2.5% β-ME at 95°C for 5 min. The eluate was denatured again at 95°C for 5 min after addition of an equal volume of 10 mM DTT in the lysis buffer. To resolve CHMP2B and a nonspecific band in the eluate, we found it critical to run the input and elution fractions on 12% Bis-Tris NuPAGE gels (Thermo Fisher Scientific, NP0342BOX). A detailed protocol has been uploaded to https://doi.org/10.17504/protocols.io.eq2lywe9pvx9/v1.

Immunoprecipitation of FLAG-tagged CHMP2B was performed as described above for endogenous CHMP2B, with three alterations. First, lysates were pre-clarified with a 750 x g centrifugation at 4°C for 5 min. Second, lysates were bound to 25 μL DYKDDDDK Fab-Trap Agarose (Proteintech, ffaa-20). Third, beads were separated from supernatant for washing via centrifugation for 5 min at 500 x g and 4°C.

To immunoprecipitate ubiquitinated proteins, cell pellets were lysed on ice in 20 mM Tris, 150 mM NaCl, 1% Triton X-100, pH 8 supplemented with cOmplete Mini EDTA-free Protease Inhibitor Cocktail, freshly-added 20 mM N-ethylmaleimide (Sigma Aldrich, E3876-25G), 50 μM PR-619 (Sigma Aldrich, 662141-25MG), and 7.5 U/mL Benzonase. Lysates were sonicated in a BioRuptor Plus for 5 cycles of 30 seconds on and 30 seconds off and clarified at 18000 x g for 10 min at 4°C. 1 mg of lysate was incubated with 50 μL of pre-equilibrated Ubiquitin pan-selector resin (NanoTag Biotechnologies, N2510) for 1 hr at 4°C with rotation. The resin was washed 3 times in 20 mM Tris, 150 mM NaCl, 1 mM EDTA, 1% Triton X-100, 0.1% SDS, pH 8 with an additional 50 μM PR-619. Elution was then carried out by boiling for 5 min at 95°C in 100 μL 2X NuPAGE LDS Sample Buffer with 2.5% β-ME. A detailed protocol appears at: https://doi.org/10.17504/protocols.io.dm6gp36k1vzp/v1.

Lysis prior to LysoIP[130] was carried out by subjecting cell pellets from a 10 cm dish to 30 strokes of a Dounce Homogenizer in 1 mL of ice-cold KPBS (10 mM KH_2PO_4, 136 mM KCl, pH 7.25 with cOmplete Mini EDTA-free Protease Inhibitor Cocktail). The lysate was then clarified by centrifugation at 1000 x g for 4 min at 4°C. 100 μg of the clarified lysate was bound to 75 μL of pre-equilibrated anti-HA magnetic beads (Thermo Fisher Scientific, 88836) at 4°C for 20 min. After 3 washes with KPBS, the bound proteins were eluted by addition of 70 μL RIPA with cOmplete Mini EDTA-free Protease Inhibitor Cocktail at 4°C for 30 min. An in-depth protocol is described at: https://doi.org/10.17504/protocols.io.yxmvmep25g3p/v1.

For the in vitro co-immunoprecipitation between CHMP2B and α-syn, 5 μM CHMP2B was mixed with either 5 μM α-syn PFFs or 5 μM α-syn monomers in PBS-T: PBS, 0.02% Tween-20, pH 7.2. Prior to use, both CHMP2B and α-syn monomers were centrifuged at 16,000 x g for 10 min at 4°C to remove any aggregated material. 250 μL of these protein mixtures and control mixtures thereof (i.e. without CHMP2B) were added to 20 μL of Protein G Dynabeads that had been previously complexed with 2 μL of rabbit anti-CHMP2B antibody (Abcam, ab33174). The protein mixtures were allowed to bind the beads for 45 min at room temperature with rotation. The beads were then washed 5 times with PBS-T and eluted with 50 μL 2X NuPAGE LDS Sample Buffer with 2.5% β-ME at 70°C for 10 min. More details can be found at: https://doi.org/10.17504/protocols.io.8epv5rb66g1b/v1.

The biotinylated $CHMP2B_{55-96}$ peptide pulldown was carried out by first conjugating 3.2 pmol of a peptide with the sequence Biotin-GSKEACKVLAKQLVHLRKQKTRTFAVSSKVTSMSTQTKVMNSQM-NH_2 (Max Planck Institute of Biochemistry Bioorganic Chemistry & Biophysics Core Facility) dissolved in 45% ethanol, 10% acetic acid, and 1 mM DTT to 25 μL Pierce Magnetic Streptavidin Beads (Thermo Fisher Scientific, 88816). These beads were then blocked in PBS, 1% Triton X-100, additional 113 mM NaCl (final concentration 250 mM), 3% BSA, pH 7.2. To eliminate aggregates from the non-aggregated species, monomeric Aβ42 and α-syn were centrifuged at 20,000 x g for 30 min at 4°C prior to use. The blocked peptide-conjugated beads (or peptide-free control) were incubated with of 2.5 μM Aβ42 monomers, Aβ42 aggregates, α-syn monomers, or α-syn PFFs for 1 hr in a buffer consisting of PBS, 1% Triton X-100, additional 113 mM NaCl, 0.1% SDS, 1 mM DTT, pH 7.2. In the case of the Aβ42 monomers, incubation was carried out at 4°C to reduce aggregation; incubations otherwise occurred at room temperature. Beads were washed three times in PBS, 1% Triton X-100, 0.1% SDS, 1 mM DTT, pH 7.2, with either 113 mM, 363 mM, or 613 mM additional NaCl. α-syn samples were eluted by boiling at 95°C for 10 min in 50 μL 1X NuPAGE LDS Sample Buffer with 1.25% β-ME. Aβ42 samples were eluted with 100 μL formic acid at 19°C for 40 min. The formic acid was then evaporated in a SpeedVac at 45°C for 1 hr. The dried protein pellet was re-solubilized by incubation in 50 μL HU Buffer (8 M urea, 5% SDS, 200 mM Tris, 1 mM EDTA, 0.01% bromophenol blue, pH 6.8) with 5% β-ME for 10 min at 60°C. A detailed protocol can be found at: https://doi.org/10.17504/protocols.io.261ge5wrwg47/v1.

Flow Cytometry

The cells measured for flow cytometry were grown in 12-well plates. Two experiments required unique replating and washing conditions. First, for the assay measuring disappearance of Gal3 FRET signal after LLOMe treatment in cells with or without aggregates (Figure 5D), α-syn aggregation was first induced in the Gal3 FRET cell line as previously described. On the following day, the cells were trypsinized and replated at a density of 1.5 x 10^5 cells per well in 12-well plates that had been coated with 0.05 mg/mL poly-D-lysine (Thermo Fisher Scientific, A3890401). The day after replating, the media was replaced with media containing 300 μM LLOMe for 2 hr. The cells were then washed once with DMEM lacking FBS, then fresh medium was added. After the indicated amounts of time, the cells were fixed and prepared for flow cytometry as described below. For the quantification of PFF leakage in cells with or without aggregates (Figure 6G), aggregation was first induced in HEK293T TetOff-α-syn-A53T mNeonGreen-3K-1-10-IRES-mKate2 cells. The cells were then trypsinized and replated on the following day at a density of 10^5 cells per well in 0.05 mg/mL poly-D-lysine-coated 12-well plates. Half of the wells containing replated cells were then treated with 100 μL Opti-MEM and either 40 μL of 1:20 diluted, sonicated α-syn PFFs carrying the D115A mutation and C-terminally tagged with $mNeonGreen_{11}$. The other half of the wells were treated with 100 μL Opti-MEM and 40 μL PBS. The $mNeonGreen_{11}$-tagged PFFs carried the D115A mutation to limit C-terminal cleavage,[172] and thereby ensure that the $mNeonGreen_{11}$ tag remained attached to the PFFs. Two days after addition of these PFFs, the cells were then processed for flow cytometry. A detailed protocol is described at: https://doi.org/10.17504/protocols.io.q26g71dr8gwz/v1.

Cells were collected for flow cytometry by trypsinization, pelleted by centrifugation at 1,500 x g for 3 min at 4°C, washed once in ice-cold PBS, then fixed in 4% PFA for 10 min at 37°C. The fixed samples were then resuspended in PBS and stored at 4°C before measurement. At least two technical replicates were collected within each experiment. Experiments conducted on different days were considered biological replicates.

Flow cytometry analysis was performed on an Attune NxT Flow Cytometer (Thermo Fisher Scientific) running Attune Cytometric Software 5.1.2111.1. mTagBFP2 fluorescence was measured by excitation with a 405 nm laser and recorded with a 440/50 filter (corresponding to the VL1-A channel). EGFP, mClover3, and split mNeonGreen-3K used a 488 nm laser and 530/30 filter (BL1-A), while mScarlet-I used a 561 nm laser and a 620/15 filter (YL2-A). FRET between mClover3 and mRuby3 was measured by via 488 nm excitation and emission through a 590/40 filter (BL2-A).

Data were processed using custom MATLAB scripts, deposited at https://github.com/csitron/MATLAB-Programs-for-Flow-Cytometry. In all cases, cells were first gated based on forward scatter (FSC-H) and side scatter (SSC-A) to eliminate cellular debris, as shown in Figure S3A. Cells transfected with CHMP2B variants were selected in the analysis by gating for VL1-A fluorescence above a non-transfected control, as these CHMP2B plasmids additionally encoded an mTagBFP2 transfection marker.

For ratiometric measurements of the ESCRT reporter, the ratio of EGFP to mScarlet-I fluorescence was assessed and a median value was calculated for each technical replicate. The values obtained from technical replicates were then averaged and normalized to the average value from a negative control within each biological replicate, such that all values presented in the figures represent a fold-change relative to this negative control (i.e. NT knockdown control in Figure 3C; untreated in Figures 3D and S3E–S3G; PBS in Figure S3B; Lpf/NT KD or Lpf/DMSO in Figure 3F).

To measure FRET between mClover3 and mRuby3, a reference no FRET control histogram was first constructed by averaging distributions of BL2-A:BL1-A fluorescence ratios for a no FRET control (e.g. no LLOMe). This histogram was then compared to an experimental condition (e.g. 2 mM LLOMe), and the percentage of the experimental condition histogram that did not overlap with the no FRET control was computed for each technical replicate, as shown in Figure S5A. The technical replicates were then averaged for each biological replicate.

For measurement of mNeonGreen-3K-positive cells in the PFF leakage assay, BL1-A vs. BL2-A fluorescence was plotted for each sample. A polygonal gate was then drawn above the xy scatter of a sample known to be mNeonGreen negative (i.e. a sample not treated with PFF-mNeonGreen$_{11}$). The percentage of cells lying in this gate was then calculated for each sample, as shown in Figure S7A.

Bioinformatic Analysis of ESCRT-III proteins

Using a human proteome accessed from UniProt, ESCRT-III protein sequences were aligned with Clustal Omega.[164] Regions homologous to CHMP2B K55-M96 (α2) were then selected for further analysis. The amino acid frequencies in α2 sequences were then computed and compared to the proteome at large. The Kyte Doolittle hydrophobicity was additionally calculated for each position in the α2 sequences and averaged. The code used for this analysis was deposited at https://github.com/csitron/Amino_acid_composition_and_hydrophobicity_analysis.

QUANTIFICATION AND STATISTICAL ANALYSIS

Statistical analysis and plotting were performed in GraphPad Prism 8 (Dotmatics). Comparisons were made between biological replicates, which we define as experiments performed on different days. Multiple comparisons were analyzed by one-way or two-way ANOVA with a post-hoc Tukey HSD test. P-values below 0.05 were considered significant. Unless otherwise indicated, statistical comparisons in barplots are shown relative to the control in the leftmost bar. N-values for experiments can be found in the figure legends.